8-1-2019

Piezoelectric Energy Harvesting via Frequency Up-conversion Technology

Amin Abedini
Southern Illinois University Carbondale, aabedin@siue.edu

PIEZOELECTRIC ENERGY HARVESTING VIA FREQUENCY UP-CONVERSION TECHNOLOGY

by

Amin Abedini
B.S., Sharif University of Technology, 2011
M.S., Sharif University of Technology, 2014

A Dissertation
Submitted in Partial Fulfillment of the Requirements for the
Doctor of Philosophy Degree

Department of Mechanical Engineering
in the Graduate School
Southern Illinois University Carbondale
August, 2019

DISSERTATION APPROVAL

PIEZOELECTRIC ENERGY HARVESTING VIA FREQUENCY UP-CONVERSION TECHNOLOGY

By
Amin Abedini

A Dissertation Submitted in Partial
Fulfillment of the Requirements
for the Degree of
Doctor of Philosophy
in the field of Engineering Science

Approved by:
Fengxia Wang, Co-Chair
Om Agrawal, Co-Chair
Keqin Gu
Albert C.J. Luo
Emmanuel C. Nsofor
Rasit Koc
Peter Filip

Graduate School
Southern Illinois University Carbondale
June 21, 2019

AN ABSTRACT OF THE DISSERTATION OF

Amin Abedini, for the Doctor of Philosophy degree in Engineering Science, presented on June 21, 2019, at Southern Illinois University Carbondale.

TITLE: Piezoelectric Energy Harvesting via Frequency Up-conversion Technology

MAJOR PROFESSOR: Dr. F. Wang

Ambient energy harvesting has attracted significant attention over the last years for applications such as wireless sensors, implantable devices, health monitoring systems, and wearable devices. The methods of vibration-to-electric energy conversion can be included in the following categories: electromagnetic, electrostatic, and piezoelectric. Among various techniques of vibration-based energy harvesting, piezoelectric transduction method has received the most attention due to the large power density of the piezoelectric material and its simple architectures. In contrast to electromagnetic energy harvesting, the output voltage of a piezoelectric energy harvester is high, which can charge a storage component such as a battery. Compared to electrostatic energy harvester, the piezoelectric energy harvester does not require an external voltage supply. Also, piezoelectric harvesters can be manufactured in micro-scale, where they show better performance compared to other energy harvesters, owing to the well-established thick-film and thin-film fabrication techniques. The main drawback of the linear piezoelectric harvesters is that they only retrieve energy efficiently when they are excited at their resonance frequencies, which are usually high, while they are less efficient when the excitation frequency is distributed over a broad spectrum or is dominant at low frequencies. High-frequency vibrations can be found in machinery and vehicles could be used as the energy source but, most of the vibration energy harvesters are targeting at low-frequency vibration sources which are more achievable in the natural environment. One way to overcome this limi-

tation is by using the frequency-up-conversion technology via impacts, where the source of the impacts can be one or two stoppers or more massive beams. The impact makes the piezoelectric beam oscillate in its resonance frequency and brings nonlinear behavior into the system. The goal of this research is to enhance the piezoelectric harvester's energy retrieving performance from ambient vibrations with low or varying frequencies. In this work, impact-based piezoelectric energy harvesters were studied by discontinuous mapping dynamics. Discontinuous dynamics has been extensively applied in mechanical dynamics and physics field. Since the nature of the most environmental vibrations is periodic, periodic motions of the impact-based piezoelectric harvester were studied. Four different possible motion phases have been identified and categorized based on the performance of the output energy of the system. Many periodic motions are possible depending on the physical properties of the energy harvester setup. So far, we studied three different periodic motions of two beams interacting with each others, where period-1 and period-2 motions of the system are predicted. The stability of the system were analyzed and bifurcation graphs for each periodic motions were presented.

ACKNOWLEDGMENTS

First I would like to give grateful thanks to my advisor Dr. Fengxia Wang, who gave me all the advices and support during the entire process of this research. I could never have achieved what I have without the intuitive guiding of Dr. Wang. Also as the dissertation advisory committee chair, Dr. Wang kindly provided a lot of help through the whole preparing process of this dissertation. Herein, I would like to express my deepest appreciation to Dr. Wang once again. Also I would like to especially thank all the dissertation advisory committee members: professor Om Agrawal, professor Albert C.J.Luo, professor Keqin Gu, professor Peter Filip, professor Emmanuel C. Nsofor and professor Rasit Koc. Thanks to you for all the advices and suggestions you gave me. Without all these helps I could not have completed this dissertation so smoothly. I would like to gratefully thank the Department of Mechanical and Industrial Engineering for their financial support. Also I wish to express my appreciation to all the faculty and staff at Southern Illinois University for the cooperative efforts during my years of graduate study. Nevertheless, the guidance from all the professors in class leads me to the successful completion of this dissertation. Finally, I would like to express my greatest appreciation to the members in our research group for their helps. Thanks to all my friends for their helps, supports, and valuable hints that make the tough work easier.

TABLE OF CONTENTS

CHAPTER **PAGE**

LIST OF FIGURES

FIGURE **PAGE**

CHAPTER 1

INTRODUCTION

1.1 ENERGY HARVESTING

Recent advances in wireless and wearable technologies and low-power electronics such as MEMS devices have demanded a surge of research in self-powered wireless sensors and self-powered data transformations. A wireless sensor network is more practical than a wired sensor due to the large-scale infrastructure and harsh environment of data transmission. Such conditions might include obtaining structure information from high pressure, high temperature, and high impact environments. Advances in manufacturing low-powered digital signal processors (DSP) has made them require power in the range of ten to hundreds of μW for variety of applications. The energy scavenged from smart materials can be used in several engineering and scientific applications, such as structural health monitoring [1, 2, 3, 4], wireless sensor networks [5, 6, 7], buoys for oceanic observations [8, 9], and, possibly, tagged global positioning system sensors for animals [10, 11].

The idea of the conversion of vibration into electricity first begun in an article from Williams and Yates [12] in 1996. They described the basic transduction mechanisms that can be used for this purpose and provided a basic excitation model of concentrated parameters to simulate the electrical output power to capture electromagnetic energy. As stated by Williams and Yates [12], the three basic mechanisms of conversion of energy from vibration to electrical energy are electromagnetic [12, 13, 14], electrostatic [15, 16] and piezoelectric [17, 18] transductions. During the last decade, several articles have appeared on the use of these transduction mechanisms for the generation of low power from environmental vibrations. Two of the review articles that cover mainly experimental research on all transduction mechanisms are provided by Beeby et al. [19] and Cook-Chennault et al. [20].

Piezoelectricity is a form of coupling between the mechanical and electrical behavior

of certain materials. Materials that exhibit the piezoelectric effect are called piezoelectric materials. The piezoelectric effect is generally divided into two parts as direct and inverse piezoelectric effects. In the simplest terms, when a piezoelectric material is compressed, an electrical charge builds up on the electrodes located on its surface. This is called a direct piezoelectric effect and was first demonstrated by the Currie brothers in 1880. If the same material is subjected to a voltage change, it will mechanically be deformed. This is called the inverse piezoelectric effect and was mathematically deduced (after the discovery of the direct piezoelectric effect) of the fundamental principles of thermodynamics by Gabriel Lippmann in 1881 and then experimentally confirmed by the Curie brothers. It is crucial to keep in mind that these two effects usually coexist in a piezoelectric material. Therefore, in an application where the direct piezoelectric effect is of particular interest (which is the case in the collection of energy) ignoring the presence of the inverse piezoelectric effect would be thermodynamically inconsistent.

It has been observed that several natural crystals exhibit the piezoelectric effect in the first half of the last century, such as Rochelle salt and quartz. However, for use in engineering applications, the electromechanical coupling between the mechanical and electrical behavior of the material must be strong enough. As a result, piezoelectric ceramics made by man have developed in the second half of the last century. The most popular engineering ceramics, PZT (lead zirconate titanate) was developed at the Tokyo Institute of Technology in the 1950s, and several versions (especially PZT-5A and PZT5H) are nowadays the most widely used engineering piezoceramics. With regard to energy harvesting research, PZT-5A and PZT-5H are the piezoceramics more commonly implemented according to the literature [20].

The high energy density and various existing forms of piezoelectric materials make the successful fabrication of a micro-size high-efficiency piezoelectric generator very promising. Over the past several years, piezoelectric energy harvesting has led to a remarkable rise in the area of self-powered structural health monitoring systems

[21, 22, 10]. Elvin and Choi [23] tested how to use a piezoelectric device to power embedded damage-detecting sensors and transmit data wirelessly to a remote receiver. Claude et al. [24] showed actuators and sensors can be powered by piezoelectric micro-generators to provide a stand-alone power source from the environmental mechanical stress in Structural Health Monitoring (SHM). Despite the great amount of attention received by self-powered wireless sensor networks over the last decade, few reports are available on the commercialization of self-powered wireless sensor networks. It should be emphasized that the self-powered sensor and data transmission remains in its infancy. In order to transmit the current practice of self-powered sensor and data transmission networks from state-of-the-art to full-scale deployment, a tremendous research effort is required to convert, optimize, and accumulate the necessary amount of energy to power such electronics.

Different ambient energy scavenging sources have been investigated, such as solar energy, thermoelectric, acoustic, and mechanical vibrations. Mechanical vibration energy harvesters can be divided into two categories: non-resonant devices, and resonant devices. Resonant mechanical vibration energy harvesters can be categorized into three groups: electrostatic, electromagnetic, and piezoelectric. The major disadvantage of electrostatic energy harvesting is that an external voltage or charge is required in order to make the relative motion of the capacitor elements produce an alternating electrical output. On the other hand, in comparison to piezoelectric harvester, the main drawback of electromagnetic harvesters is the low energy density of the electromagnetic device. As the harvester's size reduced to micro-scale, electromagnetic harvesters energy retrieving efficiency becomes less than the corresponding piezoelectric ones. The high energy density and various existing forms of piezoelectric materials make the fabrication of a small-size high-efficiency piezoelectric generators very promising, especially in the area of self-powered MEMS devices. Dutoit et al. have collected a table comparing the different types of energy harvesters, which demonstrates that when the harvester's size is small, the piezoelectric energy harvesting from vibration sources shows better performance com-

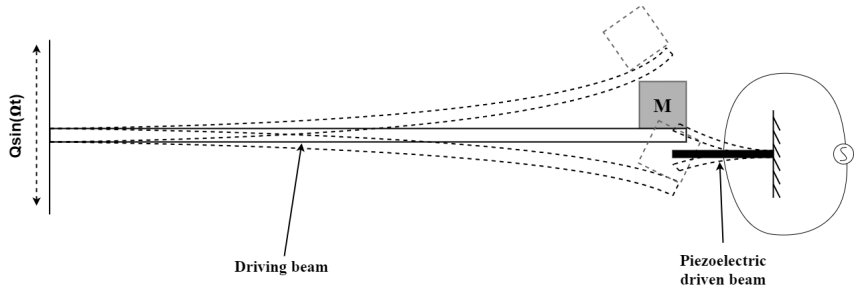

FIGURE A1: Impact-driven beam setup.

pared to scavenging energy from other energy resources or utilizing other types of material [25].

A single degree of freedom (SDF) piezoelectric energy harvester model was presented by Dutoit et al. [25], where they introduced the relationship between electrical effects of the SDF system with harmonic base excitation. Stephan used the SDF Piezoelectric energy harvester to investigate the effect of damping on the maximum power of system [26]. Erturk et al. investigated the accuracy of the SDF model and they presented a correction factor for the velocity of the tip point of the piezoelectric bar to reduce the error of SDF system [21].

The strong stiffness of most PZT plates causes their high natural frequency, usually more than 100 Hz. This brings challenges of designing a high-efficiency piezoelectric harvester due to the fact that the maximum power of a harvester can only be achieved at the resonance frequency [27, 28, 29, 30]. Currently, most piezoelectric energy harvesters are resonant-type devices, where the resonant frequency is related to the natural frequency of the piezoelectric ceramic which is not a practical frequency in normal vibration. Therefore, frequency tuning is a good solution, in which the resonant frequency is tuned to match the excitation frequency [31], but such devices are either at macro-scale [11], or difficult to tune from a high resonant frequency because of geometrical or dynamical constraints [32]. As a result, to improve the output power of the energy harvesters for low-frequency applications, researchers have presented frequency

up-conversion technologies, which may be divided into two categories: impact and non-impact types. Umeda et al. analyzed the power generated by the impact of a steel ball on a piezoelectric membrane [33]. Renaud et al. and Manla et al. presented non-resonant energy harvesters model which were excited by the repeated impact of a free ball on two piezoelectric plates. This non-resonant approach offers an advantage of power generation by impact motions, but they do not benefit the power enhancement of resonant harvesters [34, 35].

One effective method to achieve frequency up-conversion is to let the beam consecutively subject to an initial deflection to obtain repeated free vibrations. PEHs based on this method can use different plucking approaches to deflect the piezoelectric beam, such as magnetic repulsion forces to achieve non-contact frequency up-conversion [36, 37]. Pillatsch developed a generator to scavenge energy from human motions, which used magnetic forces to convert the low-frequency human motions to the resonant oscillations of a piezoelectric cantilever bimorph beam [38]. Many studies employed impact-driven contact frequency up-conversion techniques to improve the energy harvesting performance of PEHs. One design is shaking a cantilever PEH beam to let it repeatedly strike with one or two stoppers, and researchers obtained higher energy harvesting performance in a broader frequency bandwidth compared to the non-impact energy harvesters [39, 40, 41, 42]. Pozzi developed a rotary knee-joint piezoelectric energy harvester, which can produce an average power of 2 milliwatts [43]. Impact-driven PEH beams are more effective and contain complicated dynamics arising from the impact-induced discontinuous vibrations. However, most studies associated with impact-driven PEHs are focused on the experimental studies or finite element analysis [38, 39]. To obtain maximum power from impact-driven PEHs, one needs to find optimum values among different types of system parameters: 1) the optimum relation between the source vibration frequency and the gap between PEHs and stoppers; 2) the pluck load and free vibration periods. Therefore, deep understanding of the complicated dynamics induced by impact

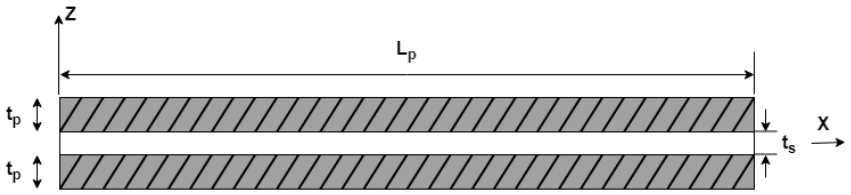

FIGURE A2: Bimorph beam schematic.

are essential.

To obtain the maximum power a piezoelectric harvester should only be excited at its resonance frequency, which is typically over 100 Hz. Most times the ambiance vibration frequency is lower than 100 Hz, therefore a normal piezoelectric harvesting device is known to underperform since the resonance frequency will not match the low excitation frequency. Besides the nonlinear broaden frequency bandwidth technologies, such as, mono-stable [44] and bi-stable [45] piezoelectric energy harvesters, frequency up-conversion is an effective method to obtain high-energy output from piezoelectric harvesters. The frequency up-conversion technique frequently applies initial deflections to the piezoelectric structure to let it vibrate freely at its mechanical resonant frequency. Different methods can be used to deflect the piezoelectric structure includes mechanical impact induced frequency-up conversion as well as magnetic repulsion non-contact frequency up-conversion [37, 36].

1.2 VIBRO-IMPACT

Vibro-impact systems are extensively researched in both the engineering and the physics fields. Such systems possess continuous characteristics as continuous dynamic systems and carry the discrete characteristics introduced by the impacts at the same time. So, discrete mapping structures developed for such vibro-impact systems are required to be able to investigate the complexity of movements. In this dissertation, some vibro-oscillators will be researched to understand the dynamics of vibro-impact systems. Before discussing the phenomena and nonlinear dynamic behavior of these vibration

impact oscillators, the theory of non-linear discrete systems will be applied to a two-dimensional discrete system (Henon map), and the full dynamics of such non-linear discrete dynamic systems will be presented. Then, the theory of discontinuous dynamic systems will be adopted to investigate the vibro-impact dynamics in several vibro-impact systems. Non-linear discrete systems are usually obtained from the non-linear difference equations of dynamic systems. These systems provide a convenient way to easily describe the behavior of a complex dynamic system by observing only the initial and final states. The complex dynamic responses in such systems can be observed through the cascade of stable solutions.

In 1976, a one-dimensional discrete map was used to describe the dynamical processes in biological, economic, and social science [46]. In the same period, a discrete-time dynamic system was introduced to simplify the 3-dimensional Lorenz equations as a Poincare map [47], from which, one can observe chaos numerically. This discrete system was later on well known as Henon map. The existence of chaotic behavior in Henon map was later mathematically proved [48] for certain parameters. At the same time, the chaotic behavior of Henon map was measured using Lyapunov characteristic exponent and frequency spectrum [49]. In 1988, the topologic properties and multifractality of Henon map were investigated [50]. In 1992, a geometric approach for the period doubling bifurcation was presented by Luo and Han [51] ,and they investigated the multifractality of a general one-dimensional iterative map. In 1993, numerical investigation of parameter maps was also performed [52] for Henon map. Later in 2000, Zhusubaliyev et al. numerically conducted the bifurcation analysis of Henon map and presented a more detailed parameter map [53]. Shaw [54] studied a single degree of freedom system with dry friction. Feeny [55] studied the chaotic dynamics of a forced dry-friction springmass system both experimentally and numerically. Luo et al also [56, 57, 58, 59] applied the theory of non-linear discontinuities to a fermi accelerator, horizontal impact pair, and train suspension system.

CHAPTER 2

METHODOLOGY

2.1 THE BIMORPH PZT BEAM CONSTITUTIVE LAW

In general, poled monolithic piezoceramics are transversely isotropic materials. To be in agreement with the IEEE Standard on Piezoelectricity [60], the plane of isotropy is defined here as the xy-plane. The piezoelectric material therefore exhibits symmetry about the z-direction, which is the poling direction of the material. The field variables are the stress components (T_{ij}), strain components (S_{ij}), electric field components (E_k) and the electric displacement components (D_k). The standard form of piezoelectric constitutive equations can be given in four different ways by taking any of two of the four field variables as independent variables. Consider the tensor representation of the deformation-form of electric displacement [60] where the independent variables are the voltage components and the components of the electric field:

$$S_{ij} = S^E_{ijkl} T_{kl} + d_{kij} E_k \tag{2.1a}$$

$$D_i = d^E_{ikl} T_{kl} + \varepsilon^T_{ik} E_k \tag{2.1b}$$

which is the preferred form of constituent piezoelectric relationships for limited means (to eliminate some of the voltage components as a function of the geometry and some of the components of the electric field as a function of the placement of the electrodes). Equations 2.1 can be given in matrix form as:

$$\begin{Bmatrix} \mathbf{T} \\ \mathbf{D} \end{Bmatrix} = \begin{bmatrix} \mathbf{c}^E & -\mathbf{e}' \\ \mathbf{e} & \boldsymbol{\varepsilon}^s \end{bmatrix} \begin{Bmatrix} \mathbf{S} \\ \mathbf{E} \end{Bmatrix}, \tag{2.2}$$

where T, D, S, E, c, e and ε are stress, electric displacement, strain, electric field, elastic modulus, piezoelectric constant and permittivity constant , respectively. The prime sign stands for transpose and, superscript E and S represent that the quantity is evaluated

at constant electric field strength and constant strain, respectively. As defined with the IEEE standard on piezoelectricity the 3-direction (or the z-direction) is the poling direction of the material [60].

$$\begin{Bmatrix} S_1 \\ S_2 \\ S_3 \\ S_4 \\ S_5 \\ S_6 \\ D_1 \\ D_2 \\ D_3 \end{Bmatrix} = \begin{bmatrix} S_{11}^E & S_{12}^E & S_{13}^E & 0 & 0 & 0 & 0 & 0 & d_{31} \\ S_{12}^E & S_{11}^E & S_{13}^E & 0 & 0 & 0 & 0 & 0 & d_{31} \\ S_{13}^E & S_{13}^E & S_{33}^E & 0 & 0 & 0 & 0 & 0 & d_{33} \\ 0 & 0 & 0 & s_{55}^E & 0 & 0 & 0 & d_{15} & 0 \\ 0 & 0 & 0 & 0 & s_{55}^E & 0 & d_{15} & 0 & 0 \\ 0 & 0 & 0 & 0 & 0 & s_{66}^E & 0 & 0 & 0 \\ 0 & 0 & 0 & 0 & d_{15} & 0 & \varepsilon_{11}^T & 0 & 0 \\ 0 & 0 & 0 & d_{15}0 & 0 & 0 & \varepsilon_{11}^T & 0 & 0 \\ d_{31} & d_{31} & d_{33} & 0 & 0 & 0 & 0 & 0 & \varepsilon_{33}^T \end{bmatrix} \begin{Bmatrix} T_1 \\ T_2 \\ T_3 \\ T_4 \\ T_5 \\ T_6 \\ E_1 \\ E_2 \\ E_3 \end{Bmatrix}, \tag{2.3}$$

where Using Voigt's notation leads us to:

$$\begin{Bmatrix} S_1 \\ S_2 \\ S_3 \\ S_4 \\ S_5 \\ S_6 \end{Bmatrix} = \begin{Bmatrix} S_{11} \\ S_{22} \\ S_{33} \\ 2S_{23} \\ 2S_{13} \\ 2S_{12} \end{Bmatrix}, \tag{2.4a}$$

$$\begin{Bmatrix} T_1 \\ T_2 \\ T_3 \\ T_4 \\ T_5 \\ T_6 \end{Bmatrix} = \begin{Bmatrix} T_{11} \\ T_{22} \\ T_{33} \\ T_{23} \\ T_{13} \\ T_{12} \end{Bmatrix}, \tag{2.4b}$$

Therefore the shear strain components in the contracted notation are the engineering shear strains. It should be noted from the elastic, piezoelectric and dielectric constants in Equ.2.3 that the poled piezoceramic considered here is a monolithic piezoceramic so that the symmetries of transversely isotropic material behavior are applied.

2.2 REDUCED CONSTITUTIVE EQUATIONS OF AN EULER-BERNOULLI BEAM

If the piezoelastic behavior of the thin monolithic structure is to be modeled as a thin beam based on the Euler-Bernoulli beam theory or Rayleigh beam theory, the only non-zero stress component is T_1 and we will have:

$$T_2 = T_3 = T_4 = T_5 = T_6 = 0 \tag{2.5}$$

Therefore based on Euler-Bernoulli beam assumption, the piezoelectric driven beam's non-zero stress component is only along the x-direction, and Equ.(2.2) is reduced to

$$\begin{Bmatrix} S_1 \\ D_3 \end{Bmatrix} = \begin{bmatrix} s_{11}^E & d_{31} \\ d_{31} & \varepsilon_{33}^E \end{bmatrix} \begin{Bmatrix} T_1 \\ E_3 \end{Bmatrix}. \tag{2.6}$$

or:

$$\begin{bmatrix} S_{11}^E & 0 \\ -d_{31} & 1 \end{bmatrix} \begin{Bmatrix} T_1 \\ D_3 \end{Bmatrix} = \begin{bmatrix} 1 & -d_{31} \\ 0 & \varepsilon_{33}^T \end{bmatrix} \begin{Bmatrix} S_1 \\ E_3 \end{Bmatrix}. \tag{2.7}$$

Therefore the stress – electric displacement form of the reduced constitutive equations for a thin beam is

$$\begin{Bmatrix} T_1 \\ D_3 \end{Bmatrix} = \begin{bmatrix} \bar{c}_{11}^E & -\bar{e}_{31} \\ \bar{e}_{31} & \bar{\varepsilon}_{33}^T \end{bmatrix} \begin{Bmatrix} S_1 \\ E_3 \end{Bmatrix}. \tag{2.8}$$

where the reduced matrix of elastic, piezoelectric and dielectric constants is

$$\bar{\mathbf{C}} = \begin{bmatrix} \bar{c}_{11}^E & -\bar{e}_{31} \\ \bar{e}_{31} & \bar{\varepsilon}_{33}^T \end{bmatrix} = \begin{bmatrix} s_{11}^E & 0 \\ -d_{31} & 0 \end{bmatrix}^{-1} \begin{bmatrix} 1 & -d_{31} \\ 0 & \varepsilon_{33}^T \end{bmatrix} \tag{2.9}$$

where over-bar denotes that the respective constant is reduced from the three-dimensional form to the plane-stress condition.

$$\bar{c}_{11}^E = \frac{1}{S_{11}^E}, \tag{2.10a}$$

$$\bar{e}_{31} = \frac{d_{31}}{S_{11}^E}, \tag{2.10b}$$

$$\bar{\varepsilon}_{33}^S = \varepsilon_{33}^T - \frac{d_{31}^2}{S_{11}^E} \tag{2.10c}$$

CHAPTER 3

LUMPED PARAMETER MODEL

3.1 LUMPED PARAMETER MODEL

The energy harvesting system consists of two cantilever beams as shown in figure A1 : 1) a soft beam as the driving beam, which is excited by base sinusoidal movement, 2) the piezoelectric driven beam shown in figure A2. In this work, both beams are expressed as lumped parameter models. For the piezoelectric driven beam, one DOF describes the dynamics and the other DOF defines the generated electricity. Both beams' equivalent masses are obtained by expressing the total kinetic energy of the beam in term of the velocity at the tip via Rayleight's quotient [61]. The transverse deflections of the neutral line of the driving beam and the piezoelectric driven beam can be written as,

$$w_i(x,t) = \phi_i(x)u_i(t), \qquad i = d, p, \tag{3.1}$$

where $\phi_d(x)$ and $\phi_p(x)$ are the transverse deflection function of the driving beam and the piezoelectric driven beam, respectively. $u_d(t)$ and $u_p(t)$ are the generalized coordinates of the driving beam and the driven beam. The x-axis is coincident with the centroidal axis of the undeformed beam, the y-axis is taken into the plane of the paper, and the z-axis is the transverse coordinate. For both beams, the normal strain of an arbitrary point across the thickness can be written as,

$$S_{i1}(x,z) = -z\frac{\partial^2 w_i(x,t)}{\partial x^2}, \qquad i = d, p. \tag{3.2}$$

the potential energy of the piezoelectric beam includes the material strain energy, electric-mechanical coupling energy, and electric energy. Using the linear mechanical-electrical constitutive law, the electric field generated by the elastic strain on the top and bottom piezoelectric layers can be written as,

$$E_3(z,t) = \begin{cases} -\frac{v_A}{t_p} e^{j\omega_p t}, & \frac{t_s}{2} < z < \frac{t_s}{2} + t_p \\ 0, & -\frac{t_s}{2} < z < \frac{t_s}{2} \\ \frac{v_A}{t_p} e^{j\omega_p t}, & -\frac{t_s}{2} - t_p < z < -\frac{t_s}{2} \end{cases} \tag{3.3}$$

where v_A is the amplitude of the generated AC voltage and t_p and t_s are the thickness of the piezoelectric and substrate layers. Hence the total potential energy of the piezoelectric beam is,

$$U_p = \frac{1}{2}\int_{V_s} c_s S_{p1}^2 dV_s + \frac{1}{2}\int_{V_p} c_{11}^E S_{p1}^2 dV_p - \int_{V_p} e_{31} E_3 S_{p1} dV_p - \frac{1}{2}\int_{V_p} \varepsilon_{33}^S E_3^2 dV_p, \tag{3.4}$$

where V_s and V_p are the volume of the piezoelectric material and the volume of the substrate, respectively. The equivalent stiffness of the driving and driven beam can be obtained via two ways: 1) using the static deflection relation of a cantilevered beam due to a concentrated transverse load at the tip, or 2) expressing the total strain energy of a whole beam in terms of the tip point deflection. In this work we use the second approach, based on the strain definition of Equ.(4), the equivalent stiffness can be obtained,

$$\frac{1}{2}\int_{V_d} Y_d S_{d1}^2 dV_d = \frac{1}{2} k_{eq_d} z_d^2(t), \tag{3.5a}$$

$$\frac{1}{2}\int_{V_S} Y_S S_{P1}^2 dV_S + \frac{1}{2}\int_{V_p} Y_d S_{P1}^2 dV_p = \frac{1}{2} k_{eq_p} z_p^2(t), \tag{3.5b}$$

$$z_i(t) = \Phi_i(x) u_i(t), \qquad i = d, p. \tag{3.5c}$$

where $z_d(t)$ and $z_p(t)$ denote of the tip points displacements of the driving beam and the piezoelectric driven beam, respectively. Y_d and V_d are the elastic Young's modulus and the volume of the driving beam, respectively. If the static deflection function subjected to a tip force is employed as the mode shape function for both driving beam and driven beam, the equivalent masses of the driving beam and the driven beam can be solved as,

$$k_{eq_d} = \frac{3Y_d I_d}{L_d^3}, \tag{3.6a}$$

$$k_{eq_p} = \frac{b_p(Y_S t_s^3 + 8t_p^3 + 12t_p^2 t_s + 6t_s^2 t_p)}{4L_p^3}, \tag{3.6b}$$

Similarly, the equivalent masses of the driving beam and the driven beam are obtained by expressing the total kinetic energy of each beam in terms of the tip point velocity of each beam, that is,

$$\frac{1}{2}\int_{V_d} \rho_d \dot{w}_d(x,t)^2 dV_d = \frac{1}{2} m_{eq_d} \dot{z}_d^2(t), \tag{3.7a}$$

$$\frac{1}{2}(\int_{V_p} \rho_p \dot{w}_p(x,t)^2 dV_p + \int_{V_S} \rho_S \dot{w}_p(x,t)^2 dV_S) = \frac{1}{2} m_{eq_p} \dot{z}_p^2(t). \tag{3.7b}$$

If the static deflection function subjected to a tip force is employed as the mode shape function for both driving beam and driven beam, the equivalent masses of the driving beam and the driven beam can be solved as [61],

$$m_{eq_d} = \frac{33}{140}\rho_d A_d L_d, \tag{3.8a}$$

$$m_{eq_p} = \frac{33}{140}(\rho_p A_p + \rho_S A_S) L_p, \tag{3.8b}$$

where L_d, A_d and ρ_d are the length, area and density of the driving beam and ρ_S, ρ_p are substrate's density and piezoelectric material's density, respectively. Similarly, A_S and A_p are the cross section area of the substrate layer and the cross section area of both piezoelectric layers. L_p is the length of the piezoelectric bimorph. With the strain energy Equ.(7a) and the kinetic energy Equ.(9) of the driving beam, as well as the base excitation, apply the Hamilton principle and add viscous damping, the lumped parameter model of the driving beam is obtained,

$$m_{eq_d}\ddot{z}_d + c_d\dot{z}_d + k_{eq_d} z_d = k_{eq_d} z_b + c_d \dot{z}_b, \tag{3.9}$$

where c_d is damping coefficient of the driving beam and z_b and $\dot{z}_b$ are the displacement and velocity functions of the base excitation. The equivalent mechanical electrical cou-

pling coefficient of the piezoelectric beam can be calculated by describing the mechanical electrical coupling potential energy in Equ.(6) with the following form,

$$-\int_{V_p} e_{31} E_3 S_{P1} dV_p = -\theta v(t) \frac{z_p(t)}{\Phi(L_p)}, \tag{3.10}$$

with a static deflection mode shape function the electric-mechanical coupling coefficient is solved as

$$\theta = 3b_p(t_s + t_p)L_p^2 e_{31} \tag{3.11}$$

The equivalent capacity of the piezoelectric beam is pull out from the electric energy term in the potential energy Equ.(6),

$$-\frac{1}{2}\int_{V_p} \varepsilon_{33}^S E_3^2 dV_p = -\frac{1}{2} C_p v^2(t), \tag{3.12}$$

Considering the series connection between the bimorph, the equivalent capacitance of the bimorph is written as:

$$C_p = \frac{b_p L_p \varepsilon_{33}^S}{2t_p}. \tag{3.13}$$

The generated electric energy due to strain will be retrieved from the piezoelectric beam, the work caused by retrieving energy is written as,

$$W = vq, \tag{3.14}$$

where q is the electric charge. Apply Hamilton principle to the strain energy Equ.(7), kinetic energy Equ.(9), electric-mechanical coupling energy Equ.(11), electric potential energy Equ.(14), and the generated electric energy retrieved from the piezoelectric beam Equ. (16), and then add the viscous damping, the lumped parameter model of the piezoelectric driven beam is obtained,

$$m_{eq_p}\ddot{z}_p(t) + c\dot{z}_p(t) + k_{eq_p} z_p(t) + \frac{\Theta}{\phi_p(L_p)} v(t) = 0, \tag{3.15a}$$

$$-\frac{\Theta}{\phi_p(L_p)} z_p(t) + C_p v(t) = q. \tag{3.15b}$$

In this work, the resistive element will provide a means of removing energy from the system,

$$v = -R\dot{q}. \tag{3.16}$$

A pure resistive load is considered, which is directly connected to the piezoelectric element. The electrical-mechanical coupling Equ.(3.15) can be written as:

$$m_{eq_p}\ddot{z}_p(t) + c\dot{z}_p(t) + k_{eq_p}z_p(t) + \frac{\Theta}{\phi_p(L_p)}v(t) = 0 \tag{3.17a}$$

$$-\frac{\Theta}{\phi_p(L_p)}\dot{z}_p(t) + C_p\dot{v}(t) = \frac{-v(t)}{R}, \tag{3.17b}$$

Following the same analysis method, if we denote the tip displacement of the plastic beam as,

$$w_d(L_d, t) = z_d(t). \tag{3.18}$$

We can write the lumped parameter model of the plastic driving beam as,

$$m_{eq_d}\ddot{z}_d(t) + c_{eq_d}\dot{z}_d(t) + k_{eq_d}z_d(t) = 0, \tag{3.19}$$

where c_{eq_d} is the viscous damping coefficient of the plastic driving beam.

3.2 PERIODIC BOUNCING

3.2.1 Modeling of Two Beams Impact via Mapping Function

Considering the state vector variables $z = (z_p, z_d)^T$, the impact variables of k^{th} impact z_{d_k}, $\dot{z}_{d_k}$ and t_k are defined as the impact position, after impact velocity and impact time of the driving beam, respectively. Similarly, the impact variables of the piezoelectric driven beam t_k, z_{p_k} and $\dot{z}_{p_k}$ are defined as the impact time, position and after impact velocity, respectively. For the time interval $t \in [t_{k-1}, t_k], (k = 1, 2, ...)$, the implicit map P_k is written as:

$$P_k : (z_{p_{k-1}}, z_{d_{k-1}}) \to (z_{p_k}, z_{d_k}) \Rightarrow (z_{p_k}, z_{d_k}, \dot{z}_{p_{k-1}}, \dot{z}_{d_{k-1}}) = P_k(z_{p_{k-1}}, z_{d_{k-1}}, \dot{z}_{p_k}, \dot{z}_{d_k}). \tag{3.20}$$

In this study, the elapsed time during the impact of the beams has been neglected and a constant coefficient of restitution is assumed. The velocity relations of the implicit map can be presented as:

$$\dot{z}_{d_k}^{+} = \frac{m_{eq_d}\dot{z}_{d_k}^{-} + m_{eq_p}\dot{z}_{p_k}^{-} + em_{eq_p}(\dot{z}_{d_k}^{-} - \dot{z}_{p_k}^{-})}{m_{eq_d} - m_{eq_p}} \tag{3.21a}$$

$$\dot{z}_{p_k}^{+} = \frac{-m_{eq_d}\dot{z}_{d_k}^{-} - m_{eq_p}\dot{z}_{p_k}^{-} - em_{eq_d}(\dot{z}_{d_k}^{-} - \dot{z}_{p_k}^{-})}{m_{eq_d} - m_{eq_p}} \tag{3.21b}$$

where $\dot{z}_{d_k}^{+}$ and $\dot{z}_{d_k}^{-}$ are the after impact and before impact velocities of the driving beam, respectively. Similarly, $\dot{z}_{p_k}^{+}$ and $\dot{z}_{p_k}^{-}$ are the after impact and before impact velocities of the driven beam and e is the coefficient of restitution.

The corresponding mechanical implicit relations of displacements and velocities of the implicit map are:

$$\begin{aligned} &f_1^d(t_k, t_{k-1}, z_{d_{k-1}}, \dot{z}_{d_{k-1}}^{+}, \dot{z}_{p_{k-1}}^{+}) = z_{d_k} = \\ &e^{-\zeta_d \omega_{n_d}(t_k - t_{k-1})}\Big[C_{s_d}\sin(\omega_{d_d}(t_k - t_{k-1})) + C_{c_d}\cos(\omega_{d_d}(t_k - t_{k-1}))\Big] \\ &+ A\sin(\Omega t_k) + B\cos(\Omega t_k) \end{aligned} \tag{3.22a}$$

$$\begin{aligned} &f_1^p(t_k, t_{k-1}, z_{d_{k-1}}, \dot{z}_{d_{k-1}}^{+}, \dot{z}_{p_{k-1}}^{+}) = z_{p_k} = \\ &e^{-\zeta_p \omega_{n_p}(t_k - t_{k-1})}\Big[C_{s_p}\sin(\omega_{d_p}(t_k - t_{k-1})) + C_{c_p}\cos(\omega_{d_p}(t_k - t_{k-1}))\Big] \end{aligned} \tag{3.22b}$$

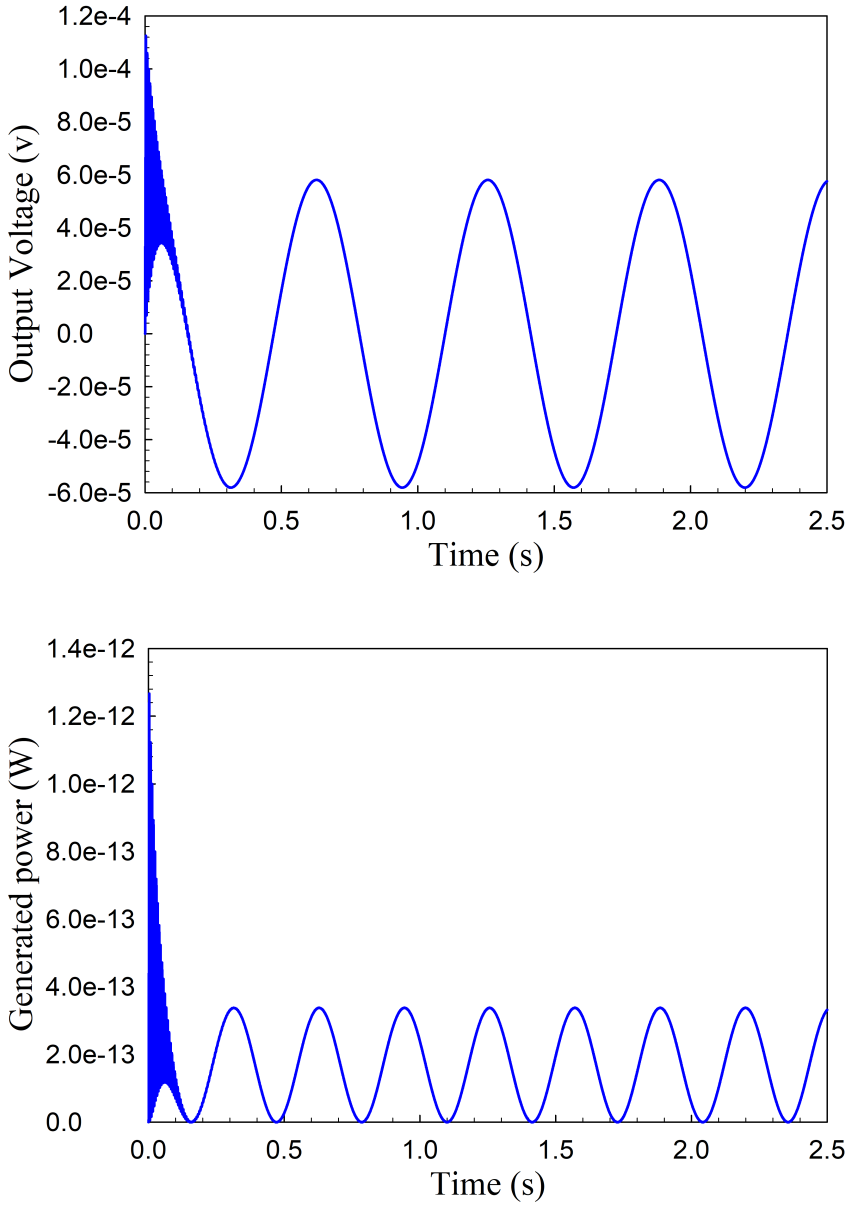

FIGURE A1: A simple piezoelectric beam energy harvester with base excitation, (a) output voltage, (b) harvested power

$$\hat{f}_2^d(t_k, t_{k-1}, z_{d_{k-1}}, \dot{z}_{d_{k-1}}^+, \dot{z}_{p_{k-1}}^+) = \dot{z}_{d_k} =$$

$$e^{-\zeta_d \omega_{n_d}(t_k - t_{k-1})} \Big[(C_{s_d}\omega_{dd} - C_{c_d}\zeta_d\omega_{n_d}) \cos(\omega_{d_d}(t_k - t_{k-1}))$$

$$- (C_{s_d}\omega_{n_d} + C_{c_d}\omega_{d_d}) \sin(\omega_{d_d}(t_k - t_{k-1})) \Big] + A\Omega \cos(\Omega t_k) \tag{3.23a}$$

$$- B\Omega \sin(\Omega t_k)$$

$$\hat{f}_2^p(t_k, t_{k-1}, z_{d_{k-1}}, \dot{z}_{d_{k-1}}^+, \dot{z}_{p_{k-1}}^+) = \dot{z}_{p_k} =$$

$$e^{-\zeta_p \omega_{n_p}(t_k - t_{k-1})} \Big[(C_{s_p}\omega_{dp} - C_{c_p}\zeta_p\omega_{n_p}) \cos(\omega_{d_p}(t_k - t_{k-1}))$$

$$- (C_{s_p}\omega_{n_p} + C_{c_p}\omega_{d_p}) \sin(\omega_{d_p}(t_k - t_{k-1})) \Big], \tag{3.23b}$$

where

$$\omega_{n_i} = \sqrt{\frac{k_{eq_i}}{m_{eq_i}}}, \qquad i = d, p, \tag{3.24a}$$

$$\zeta_i = \frac{c_{eq_i}}{2\sqrt{k_{eq_i} m_{eq_i}}}, \qquad i = d, p, \tag{3.24b}$$

$$\omega_{d_i} = \sqrt{1 - \zeta_i^2}\omega_{n_i}, \qquad i = d, p, \tag{3.24c}$$

where C_{s_d}, C_{c_d} are the sine and cosine coefficient extracted from initial conditions and A, B are the particular solution coefficients of the driving beam, respectively. Similarly, C_{s_p}, C_{c_p} are the initial condition constants of the driven beam. The above coefficients are provided in appendix. In the above equations, $\hat{f}_2^p$ and $\hat{f}_2^d$ are the before impact velocity equations of the driven and driving beams, respectively. By using Equ.(3.21) and (3.23), we can get the after impact velocities of both beams as below:

$$\begin{Bmatrix} f_2^d \\ f_2^p \end{Bmatrix} = \begin{Bmatrix} (m_{eq_d} - e m_{eq_p})\hat{f}_2^d + m_{eq_p}(1+e)\hat{f}_2^p \\ m_{eq_d}(1+e)\hat{f}_2^d + (m_{eq_p} - e m_{eq_d})\hat{f}_2^p \end{Bmatrix}. \tag{3.25}$$

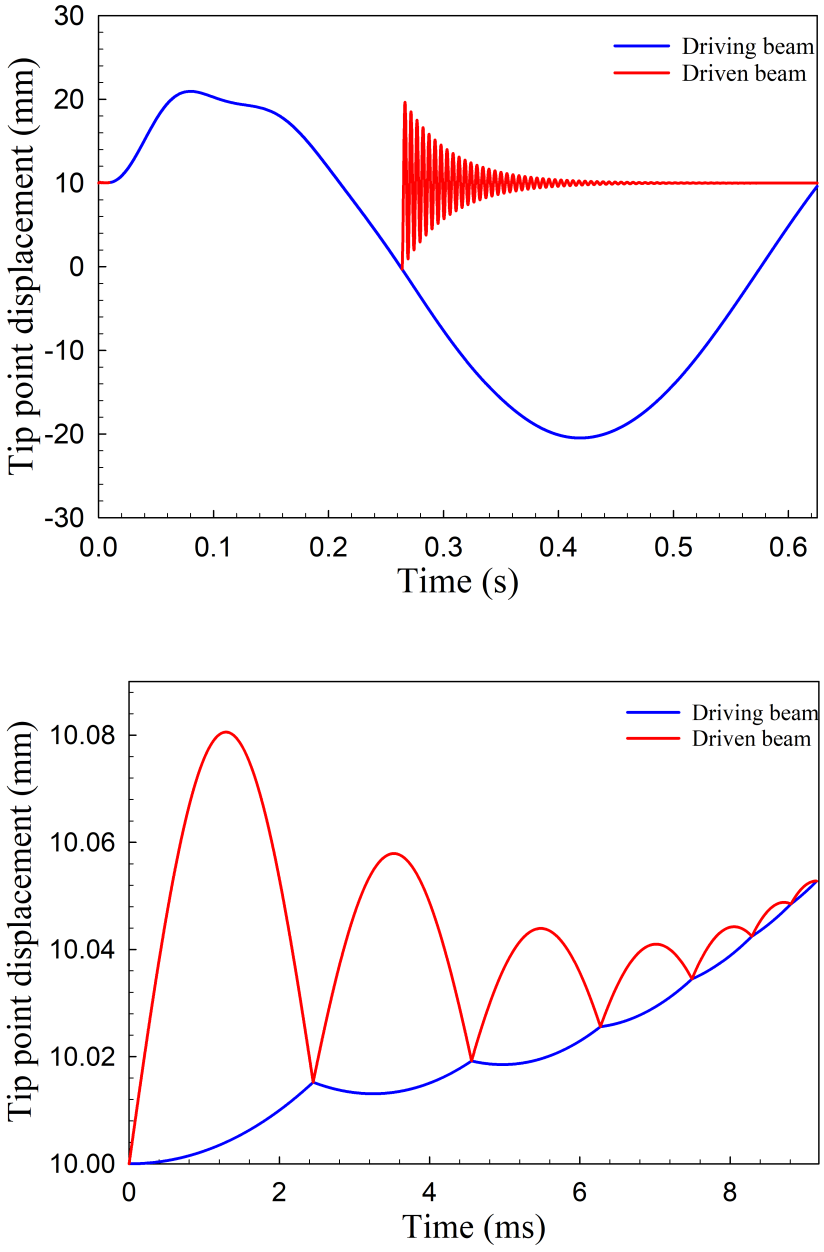

FIGURE A2: Voltage a output from system with arbitrary initial condition, (a) voltage versus time, (b) Voltage from the chattering phase versus time.

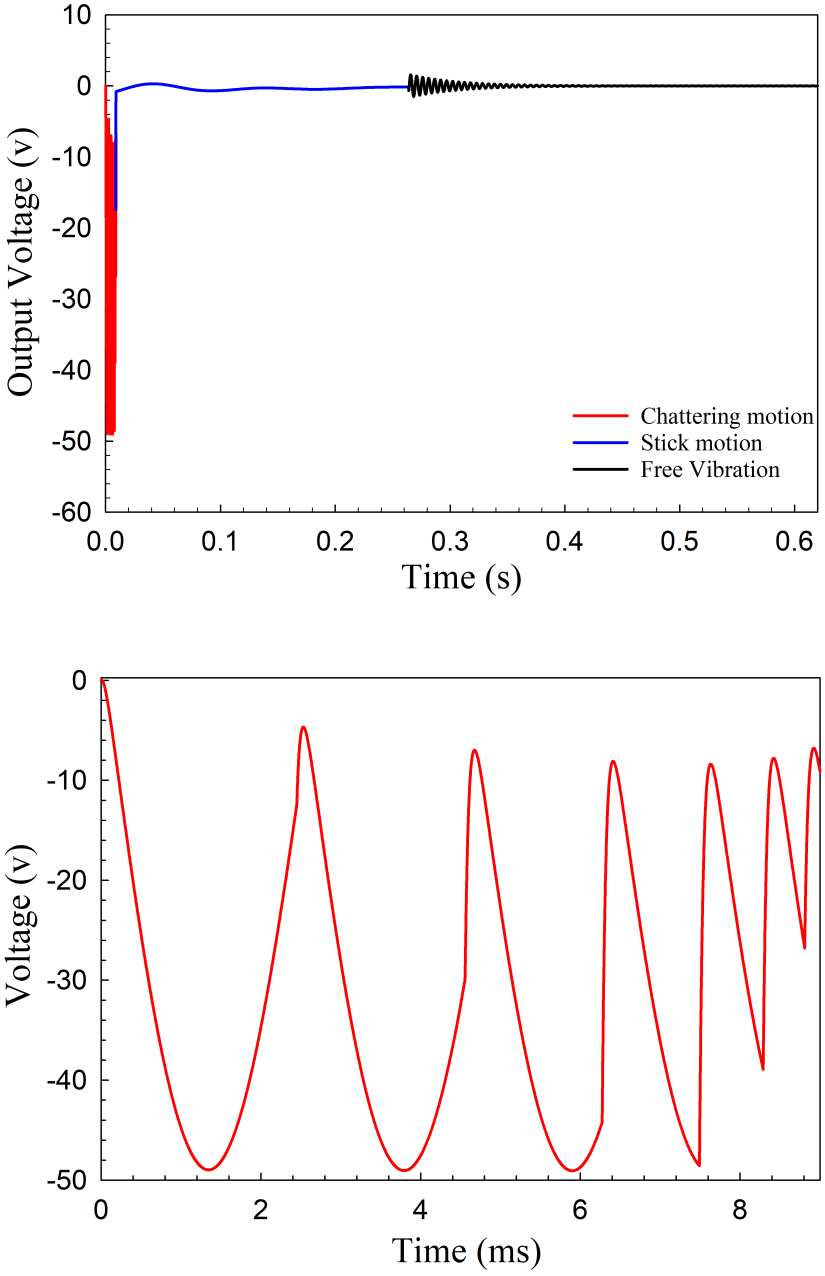

FIGURE A3: Voltage a output from system with arbitrary initial condition, (a) voltage versus time, (b) Voltage from the chattering phase versus time.

According to Equ.(3.23) and Equ.(3.25), the discrete impact mapping functions can be defined as:

$$F_k^1(t_k, z_{d_k}, t_{k-1}, z_{d_{k-1}}, \dot{z}_{d_{k-1}}^+, \dot{z}_{p_{k-1}}^+) = f_1^d - z_{d_{k-1}} = 0, \tag{3.26a}$$

$$F_k^2(t_k, z_{d_k}, \dot{z}_{d_k}^+, \dot{z}_{p_k}^+, t_{k-1}, z_{d_{k-1}}, \dot{z}_{d_{k-1}}^+, \dot{z}_{p_{k-1}}^+) = f_2^d - \dot{z}_{d_{k-1}}^+ = 0, \tag{3.26b}$$

$$F_k^3(t_k, z_{d_k}, t_{k-1}, z_{d_{k-1}}, \dot{z}_{d_{k-1}}^+, \dot{z}_{p_{k-1}}^+) = f_1^p - z_{p_{k-1}} = 0 \tag{3.26c}$$

$$F_k^4(t_k, z_{d_k}, \dot{z}_{d_k}^+, \dot{z}_{p_k}^+, t_{k-1}, z_{d_{k-1}}, \dot{z}_{d_{k-1}}^+, \dot{z}_{p_{k-1}}^+) = f_2^p - \dot{z}_{p_{k-1}}^+ = 0, \tag{3.26d}$$

$$z_{d_k} = z_{p_k}, \tag{3.26e}$$

$$z_{d_{k-1}} = z_{p_{k-1}}. \tag{3.26f}$$

Once the switching points for a specific periodic motion is obtained, the local stability and bifurcation analysis can be achieved through the corresponding stability Jacobian matrix:

$$D\mathbf{P} = DP_1^{-1} \cdot DP_0 = \left[\frac{\partial \mathbf{F}_k}{\partial \mathbf{Z}_{k+1}}\right]^{-1} \left[\frac{\partial \mathbf{F}_k}{\partial \mathbf{Z}_k}\right], \tag{3.27}$$

where

$$\mathbf{F}_k = [F_k^1, F_k^2, F_k^3, F_k^4]^T, \tag{3.28a}$$

$$\mathbf{Z}_k = [t_k, z_{d_k}, \dot{z}_{d_k}, \dot{z}_{p_k}]^T, \tag{3.28b}$$

$$DP_i = \left[\frac{\partial \mathbf{F}_{k+i}}{\partial \mathbf{Z}_{k+i-1}}\right]. \tag{3.28c}$$

Considering the eigenvalues of DP, the following statements hold:

If all $|\lambda_i| < 1$ for $(i = 1, 2, 3, 4)$, the periodic motion is stable.

If $|\lambda_i| > 1$ for $(i \in \{1, 2, 3, 4\})$, the periodic motion is unstable.

If $\lambda_i = -1$ and $|\lambda_j| < 1$ for $(i, j \in \{1, 2, 3, 4\}$ and $i \neq j)$, the period-doubling bifurcation of periodic motion occurs.

If $\lambda_i = 1$ and $|\lambda_j| < 1$ for $(i, j \in \{1, 2, 3, 4\}$ and $i \neq j)$, the saddle-node bifurcation of the periodic motion occurs.

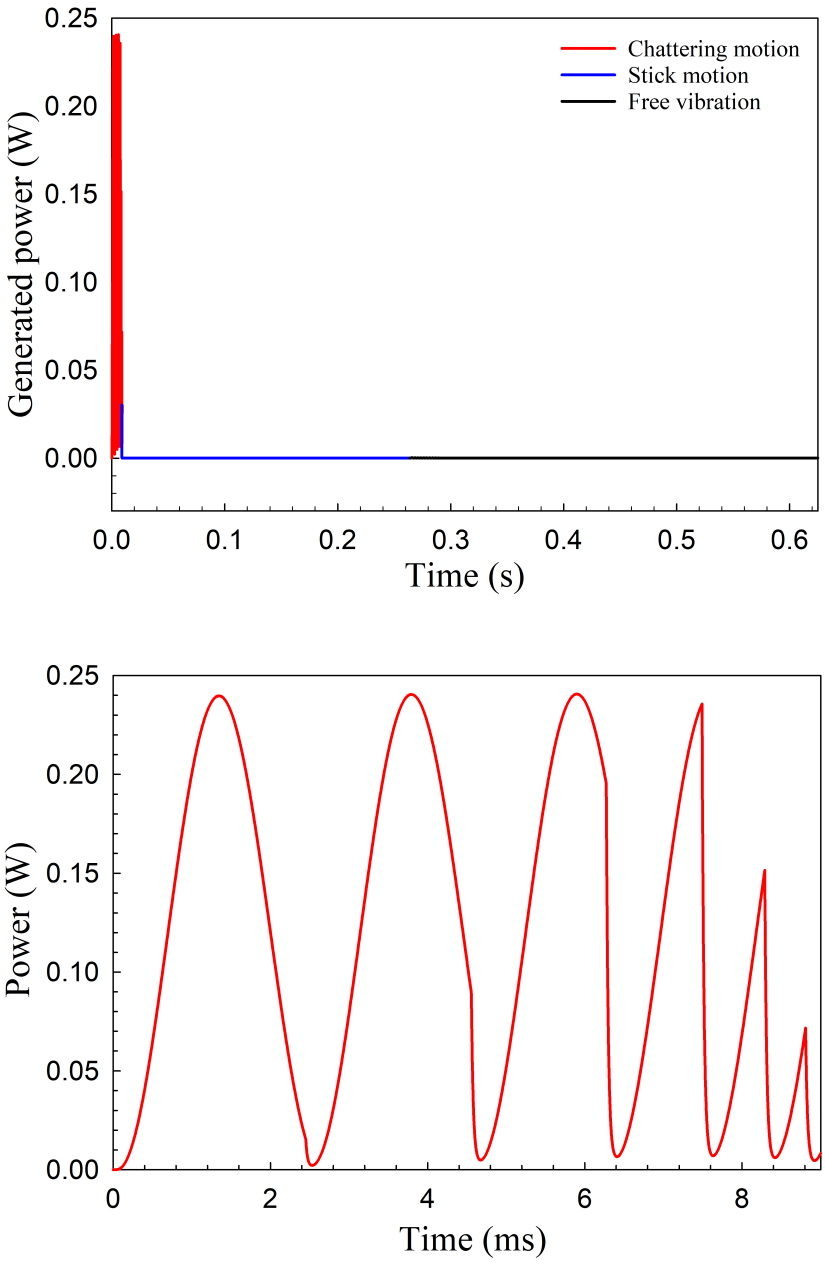

FIGURE A4: Power output from system with arbitrary initial condition, (a) power versus time, (b) power from the chattering phase.

If $|\lambda_{i,j}| = 1$ is a pair of complex eigenvalues, the Neimark bifurcation of the periodic motion occurs.

3.2.2 NUMERICAL PREDICTIONS

In this section, different types of motions of the proposed piezoelectric energy harvester system are studied and the bifurcation diagrams of periodic solution with impact-driven motions are obtained. The numerical predictions of the output voltage and power of period-1 to period-2 motions are also examined.

3.2.3 Motion with arbitrary initial condition

The goal of this research is to enhance the piezoelectric harvester's energy retrieving performance from ambient vibrations with low or varying frequencies. Therefore, the frequency region in our study is less than the natural frequency of the piezoelectric beam. As a reference point, let's first test the voltage and power output of the piezoelectric beam without impact, when the ambient vibration frequency and magnitude are set to be $\Omega = 1.6\ Hz, Q = 0.02m$. Using the provided model, the output voltage and power from a piezoelectric beam without impact are presented in the figure A1. It is shown that the output voltage and power are less than one mili-volt and one nano-watt via shaking a single piezoelectric beam with low excitation frequency.

In order to improve the energy harvesting efficiency, an impact-driven piezoelectric harvester is introduced. The output voltage and power of the piezoelectric beam excited by impact from the driving beam with arbitrary initial condition are predicted as shown in figures A3 and A4 and, the displacement of the piezoelectric beam is presented in figure A2. Comparing figures A1(b) and A4(b), one can see that the impact-driven piezoelectric harvester has great potential to provide much more energy when the excitation frequency is low.

Four different types of motions are defined for the impact-driven piezoelectric beam:

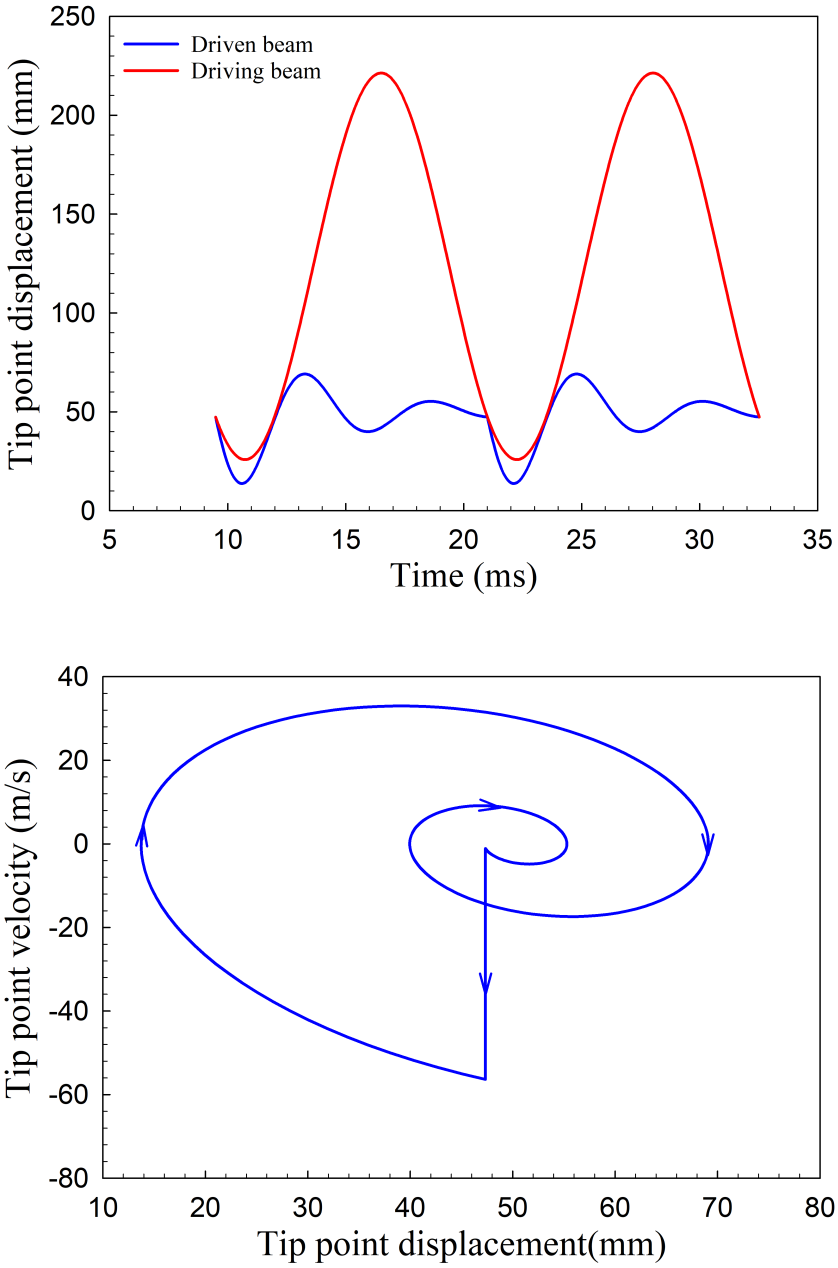

FIGURE A5: Period-1 motion displacement of the driving beam (red) and driven beam (blue) and phase-diagram for the piezoelectric driven beam at $\Omega = 86\ Hz$, (a) Displacement versus time, (b) Velocity versus Position.

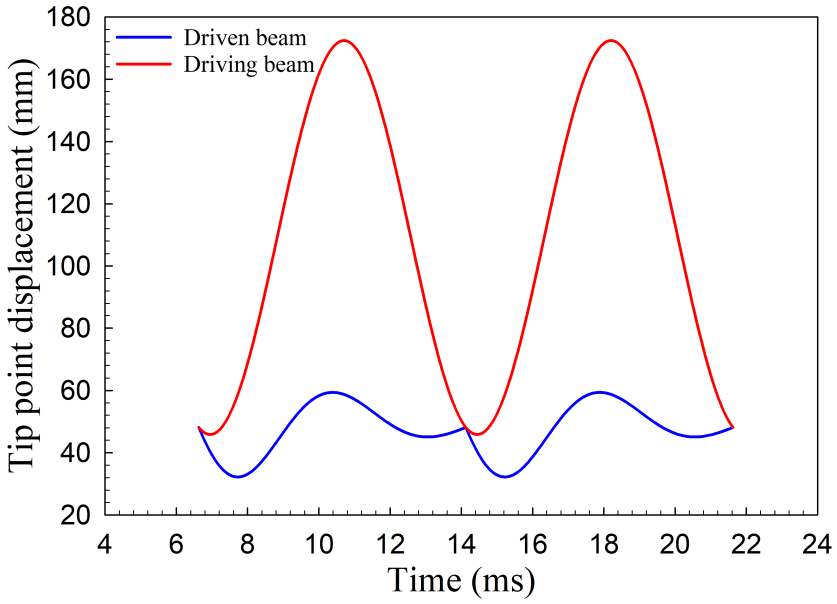

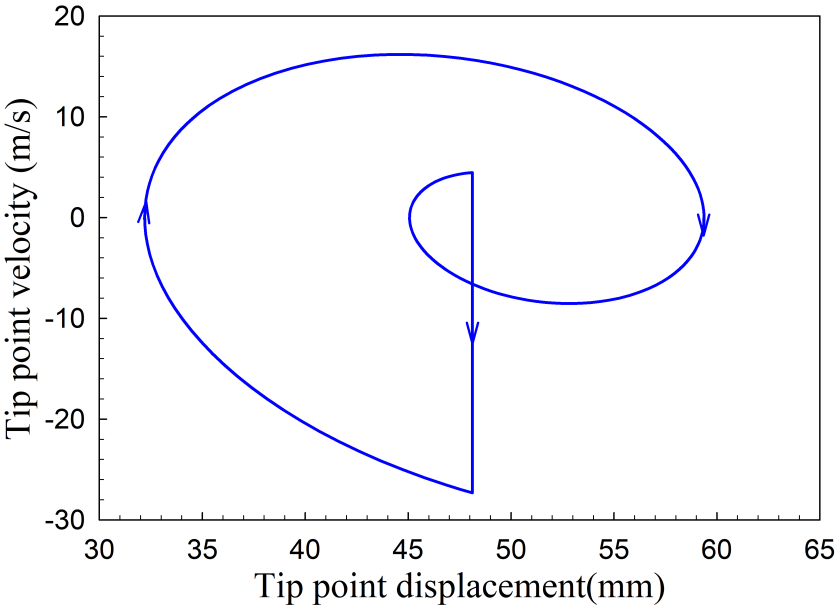

FIGURE A6: Period-1 motion displacement of the driving beam (red) and driven beam (blue) and phase-diagram for the piezoelectric driven beam at $\Omega = 133\ Hz$, (a) Displacement versus time (b) Velocity versus Position.

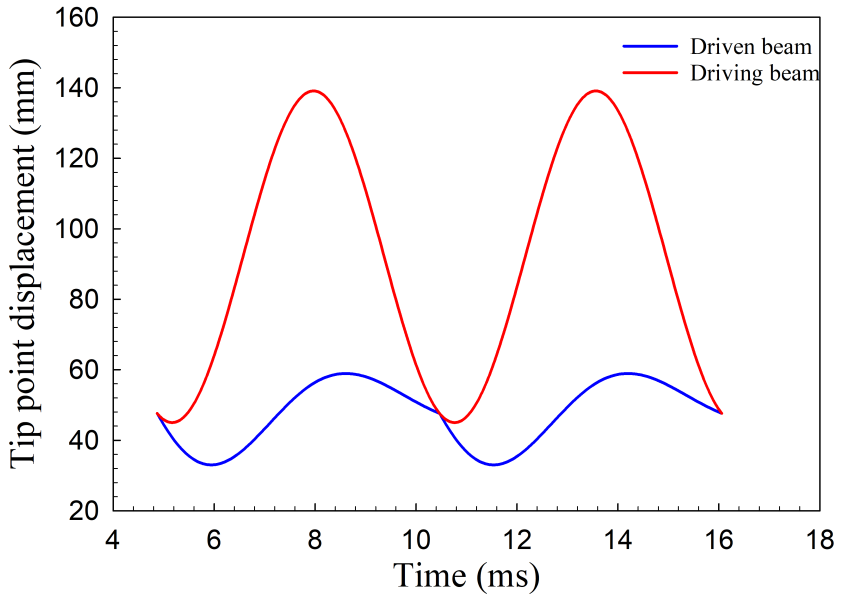

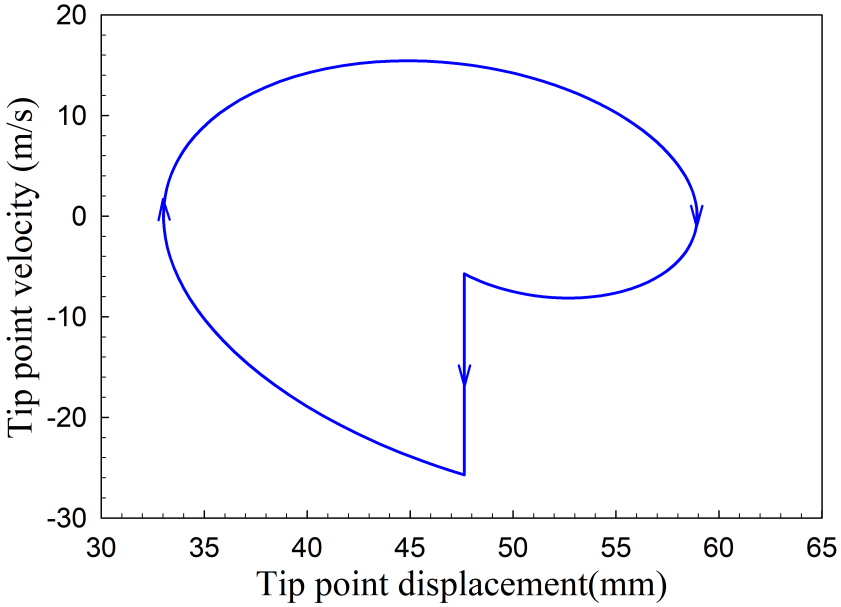

FIGURE A7: Period-1 motion displacement of the driving beam (red) and driven beam (blue) and phase-diagram for the piezoelectric driven beam at $\Omega = 178\ Hz$, (a) Displacement versus time, (b) Velocity versus Position.

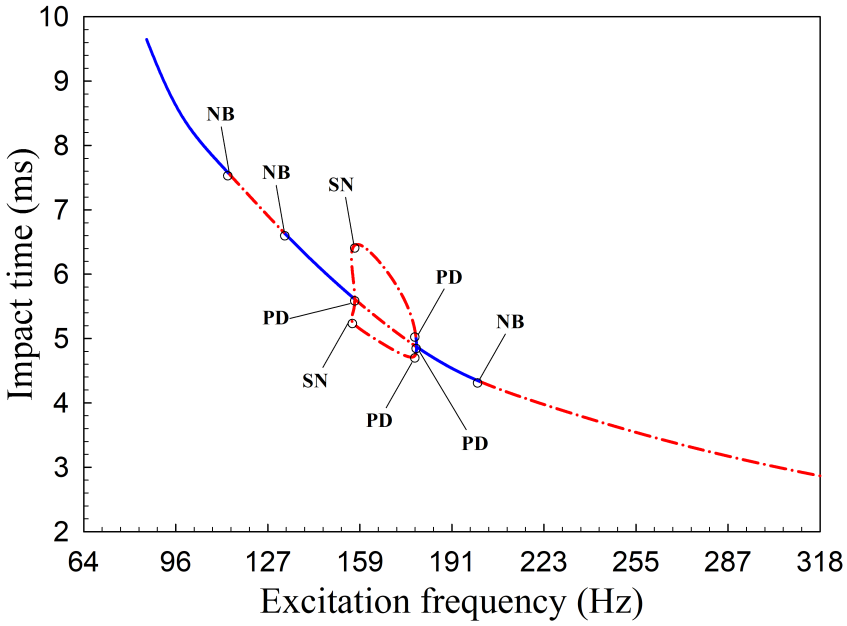

FIGURE A8: Impact time of the beams versus excitation frequency $\Omega \in [85, 318]\ Hz$.

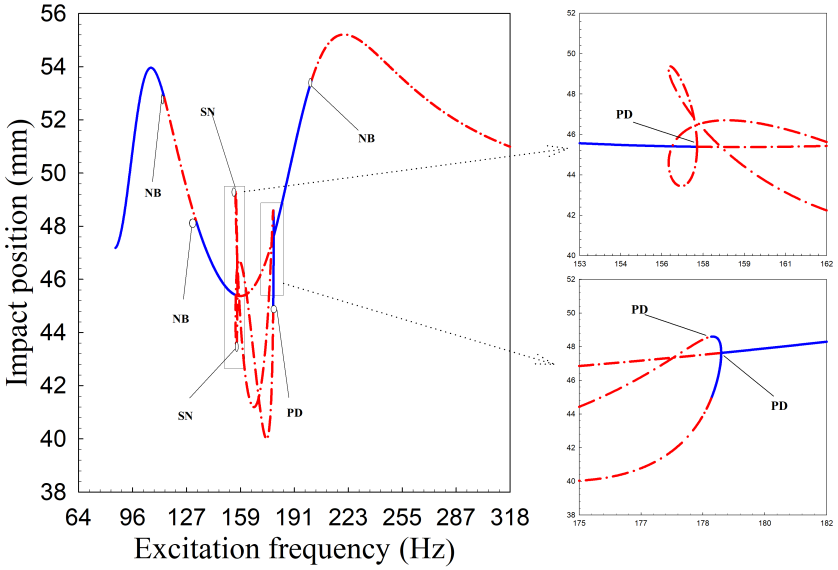

FIGURE A9: Impact position of the beams versus excitation frequency $\Omega \in [85, 318]\ Hz$.

stick motion, free vibration, chattering and rapid-impact. Stick motion happens when the beams move along with each other after the impact. Free vibration motion phase is defined as the piezoelectric beam performs at least three complete cycles of its periodic motion after the impact. The chattering motion happens when two beams hit each other rapidly with a small amplitude which usually ends up to stick motion phase, in other words, chattering motion is a pre-stick motion phase of motion (figure A2(b)). Rapid-impact motion is defined when the piezoelectric beam does not have enough time to let three cycles of motion to finish before the next impact. The rapid-impact phase is similar to chattering motion phase but it does not followed by stick motion phase and has a larger amplitude. The output voltage and power for three different types of motion with arbitrary initial conditions are studied, where figure A2(a) shows the displacements of the driving beam and the driven beam of chattering motion followed by stick motion and free vibration phase. In figure A2(b) the red and blue lines stand for the tip point displacement of the driven and driving beams in the chattering motion phase, respectively. According to figures A3 and A4, one can observe that a lot of voltage and naturally power is retrieved in chattering motion phase, while the generated power in the other two phases are not significant. The high performance of the chattering motion phase leads us to study periodic motion with rapid-impact phase in order to get the best possible power output. The pure rapid-impact motion would not occur naturally with arbitrary initial conditions, which can be achieved in periodic motions via properly calculating the initial conditions. Non-periodic rapid-impact motions end up to a stick motion phase and will not improve the power generation efficiency.

Therefore, to increase the energy harvesting efficiency via impact-induced frequency up-conversion, one needs to carefully investigate the impact dynamics of the system. These studies can help us to: 1) identify domains of low energy generation stick motions; 2) obtain optimum system parameters correlations, such the gap between beams or excitation frequencies; 3) find proper initial conditions to start consecutive chattering phase

of the piezoelectric beam with high-efficiency power output.

3.2.4 Periodic Motion

For an impact-driven system, periodic motions are the simplest ones. To deeply understand the impact-driven frequency up-converter system, periodic motions of the energy harvesting system are studied. Based on figures A2, A3 and A4, in order to have optimum motion, the system has to avoid stick motion and contain more rapid-impact motion. Figures A5(a), A6(a) and A7(a) show multiple period-1 a period-1 motion, where the red and blue lines represent the tip point displacements of the driven and the driving beams in two cycles, respectively. Figures A5(b), A6(b) and A7(b) are the velocity versus displacement or the phase portrait of period-1 motion of the piezoelectric beam.

In this section, the bifurcation diagrams of periodic motions are presented via studying the analytic solutions of period-1 to period-2 motions. Without losing generality, a set of system parameters are considered as :$Q = 0.05m$, $e = 0.7$, as the base excitation amplitude and the coefficient of restitution. The bifurcation diagram as well as the numerical solutions of period-1 to period-2 motions of this coupled beam oscillators are obtained via studying the implicit mapping dynamics of the system. As the excitation frequency varies, the bifurcation diagram of impact time, switching displacements and switching velocities of the periodic solutions are shown in figures A8, A9 and A10, where the solid blue and red dashed lines represent the stable and unstable motions, respectively. The acronyms NB, SN and PD, represent the Neimark, saddle-node and period-doubling bifurcation points, respectively. The period-4 motions can be generated from the period-doubling bifurcation points of period-2 motions. Similarly, period-8 motions appear from the period-doubling bifurcation points of period-4 motions. figure A16(a) shows the average harvested power from P-1 and P-2 motions. According to figure A16(a) the proposed system generates more power in lower frequencies compared to the higher frequencies. A small stable P-2 branch exists for this kind of motion, which is

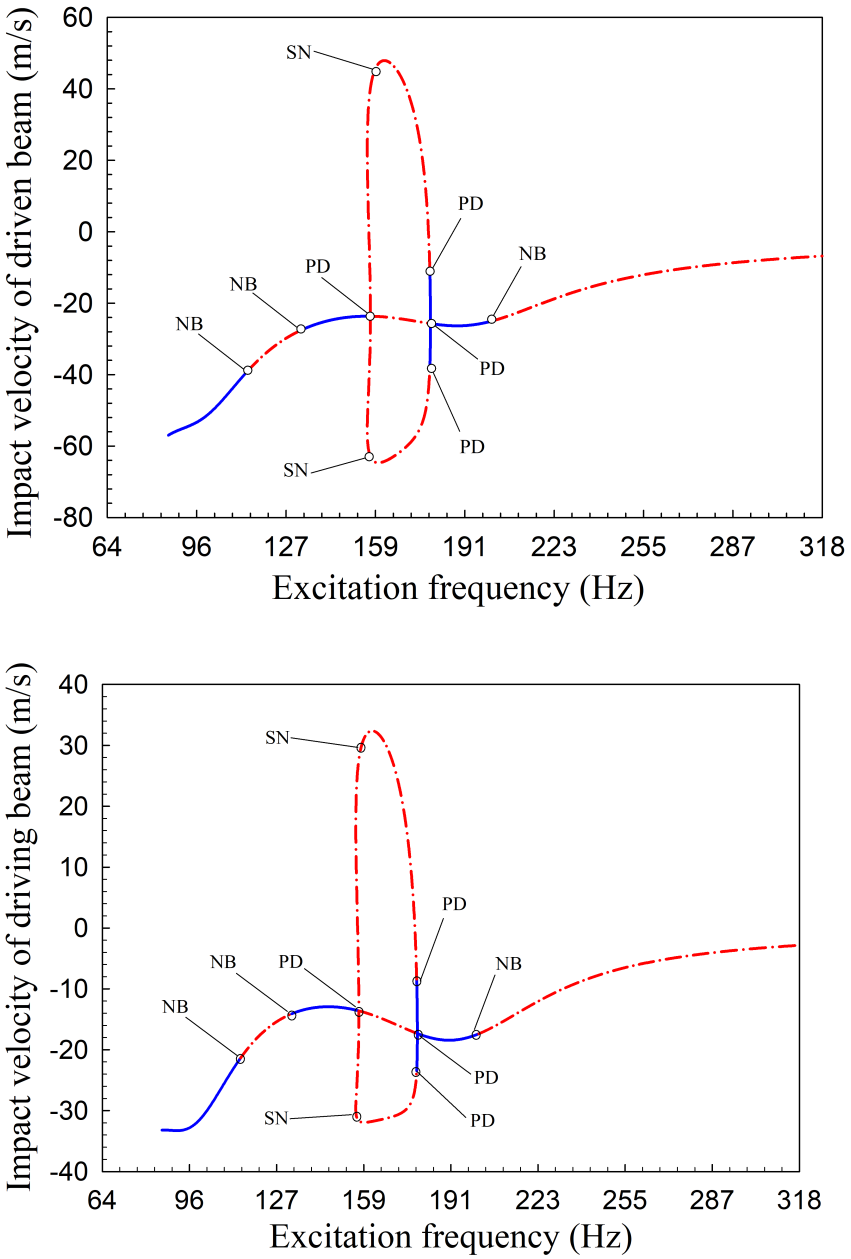

FIGURE A10: Impact velocity of the beams versus excitation frequency $\Omega \in [85, 318]\ Hz$, (a) Impact velocity of driven beam versus excitation frequency, (b) Impact velocity of driving beam versus excitation frequency.

better visible in the zoom in part of figure A9. Since the output power of the stable P-2 motion is not visible in on figure A16(a) a sample P-2 stable motion output voltage and power is provided in figure A15. These graphs demonstrate that the power generated in the P-1 motion is about four times larger than the P-2 motion. The reason for this behavior can be explained using figures A7(b) and A11(b), where one can observe that the second impact in P-2 motion generates about 5 m/s velocity jump, while the first impact generated about 40 m/s velocity jump. On the other hand, the P-1 motion benefits the 20 m/s jump for all of its impacts. Based on the above observation, the period-4, period-8, and other higher-order periodic motions are not studied in this research, because they should have even lower output power and smaller bandwidth.

The tip point displacement of two beams and the phase diagram of the driven beam for period-2 stable motion are shown in figure A11 over one period at $\Omega = 178\ Hz$. Figure A15 shows the generated voltage and power from the above motion with the optimum resistor. Based on figure A16, three different stable P-1 regions are achieved, and figures A5, A6 and A7 show one tip point displacement for both beams and velocities for the driven beam from each region. Figures A12, A13 and A14, shows the output power and voltage from these motions. Using figures A5, A6, A7, A12, A13 and A14, one can observe that the output power is closely associated with the velocity jump and the elapsed time between the impacts. For example, the motion in A5(b) has the largest velocity jump and also has the largest generated power(A12(b)), however, comparing figures A6(b) and A7(b), the velocity jumps are 40 m/s and 20 m/s, respectively, while the output power in the A14(b) is slightly greater than A13(b). That is because the higher excitation frequency produces faster impacts or more kinetic energy transfer. Excitation frequency of the motion of figures A7(b) and A14(b) is much higher than the motion of figures A6(b) and A13(b). When velocity jump is bigger in each impact, more kinetic energy will be transferred from driving beam to the driven beam, while when the excitation frequency is higher, faster impacts and energy transfer will be obtained.

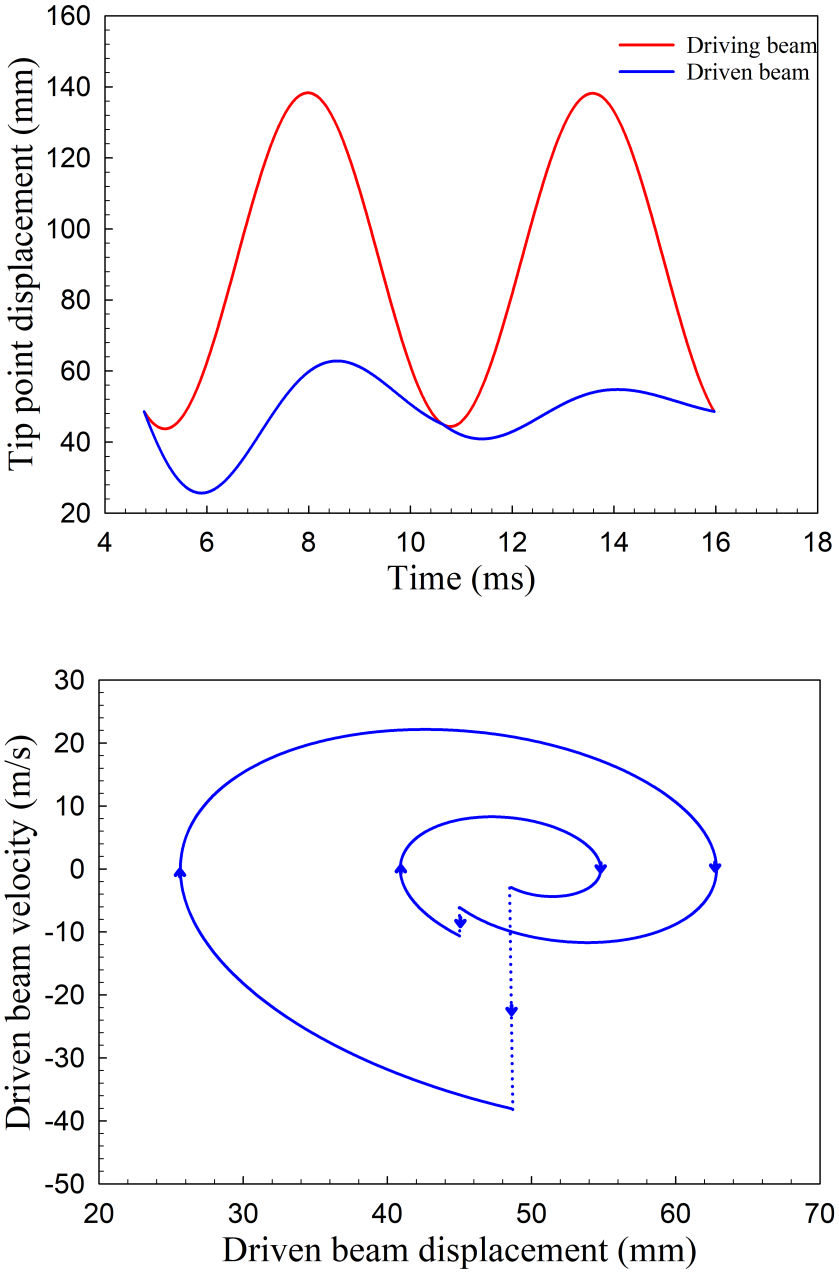

FIGURE A11: Period-2 motion at $\Omega_x = 178\ Hz$, (a) Position of the driving beam (red) and driven beam (blue) versus time, (b) Velocity versus Position of the driven beam.

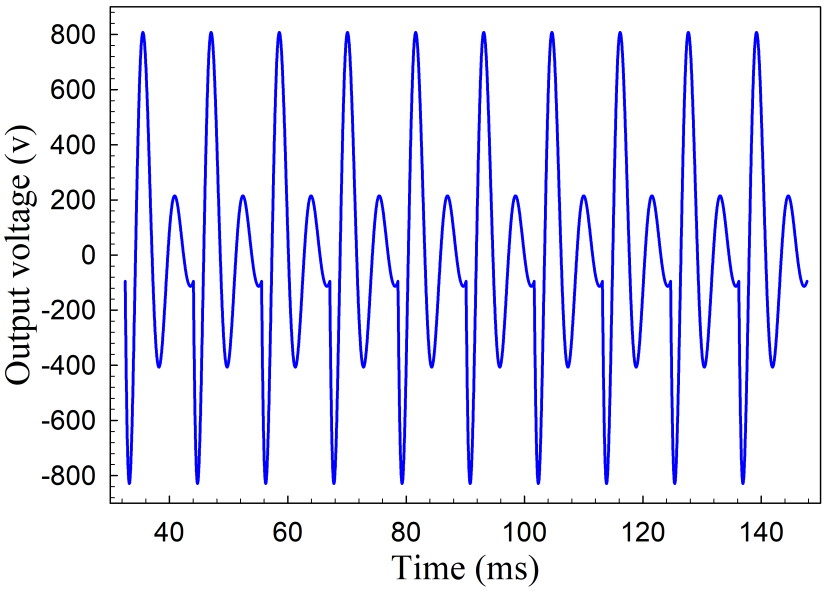

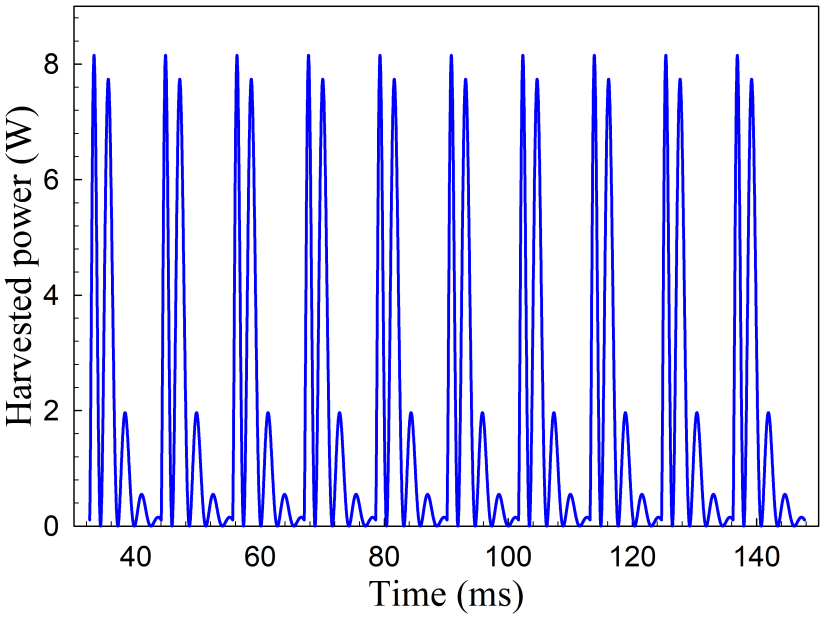

FIGURE A12: Output voltage and harvested power versus time in period one motion within ten periods at $\Omega = 86\ Hz$, (a) Voltage versus time (b) Harvested power versus time.

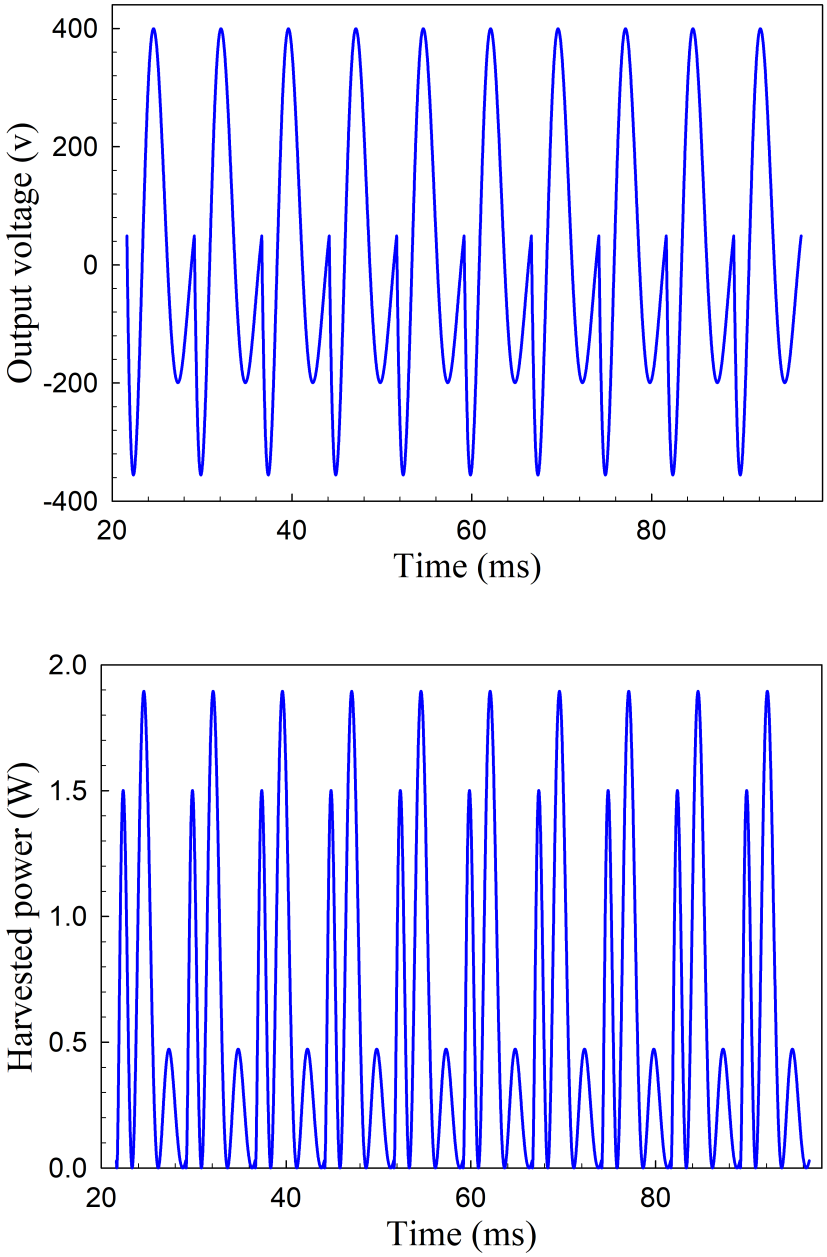

FIGURE A13: Output voltage and harvested power versus time in period one motion within ten periods at $\Omega = 133\ Hz$, (a) Voltage versus time, (b) Harvested power versus time.

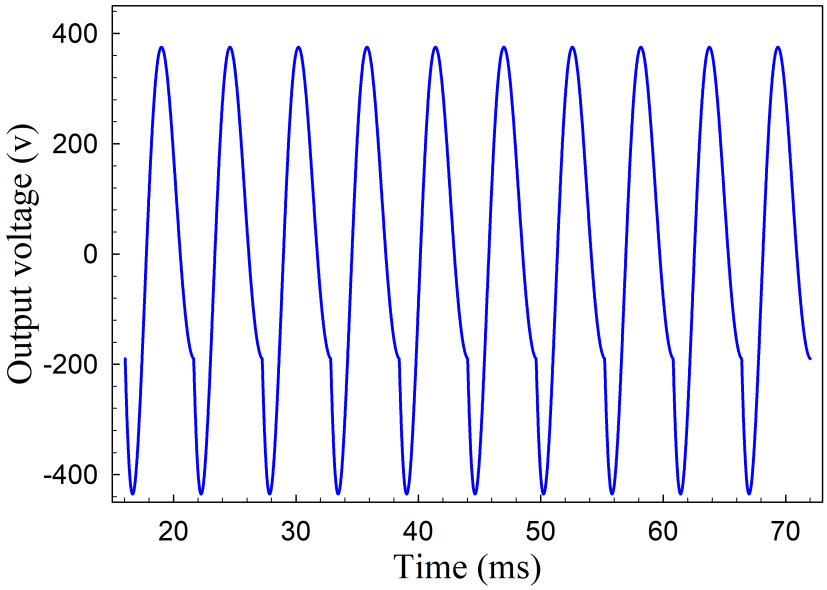

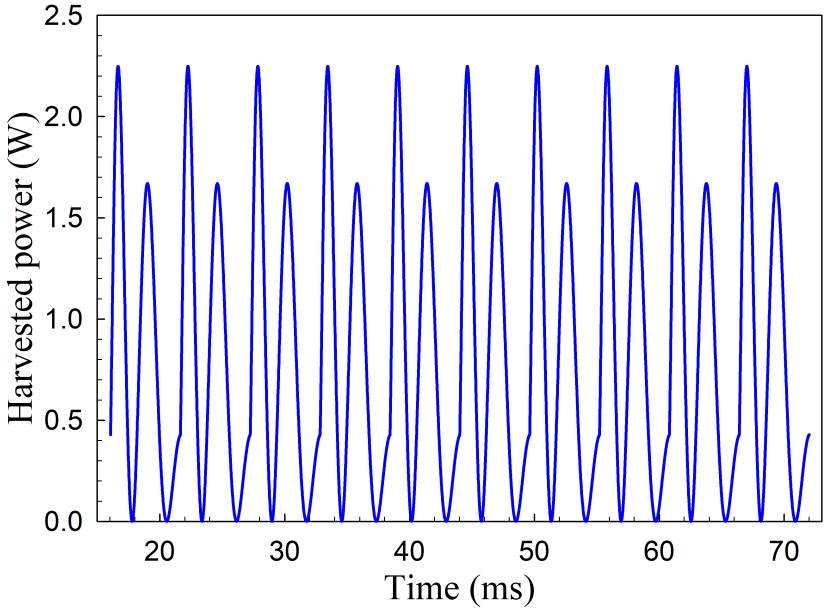

FIGURE A14: Output voltage and harvested power versus time in period one motion within ten periods at $\Omega = 178\ Hz$, (a) Voltage versus time, (b) Harvested power versus time.

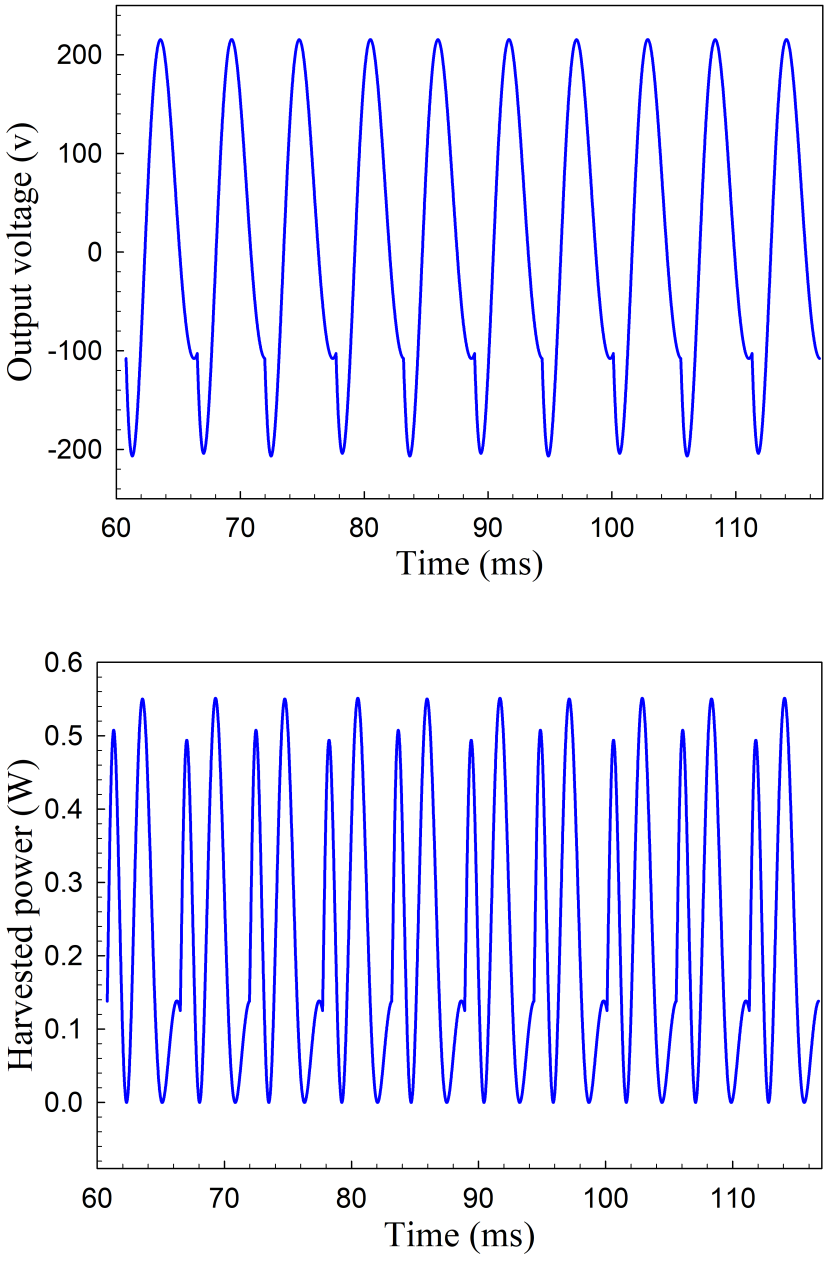

FIGURE A15: Output voltage and harvested power versus time in period two within ten periods at $\Omega = 178\ Hz$, (a) Voltage versus time, (b) Harvested power versus time.

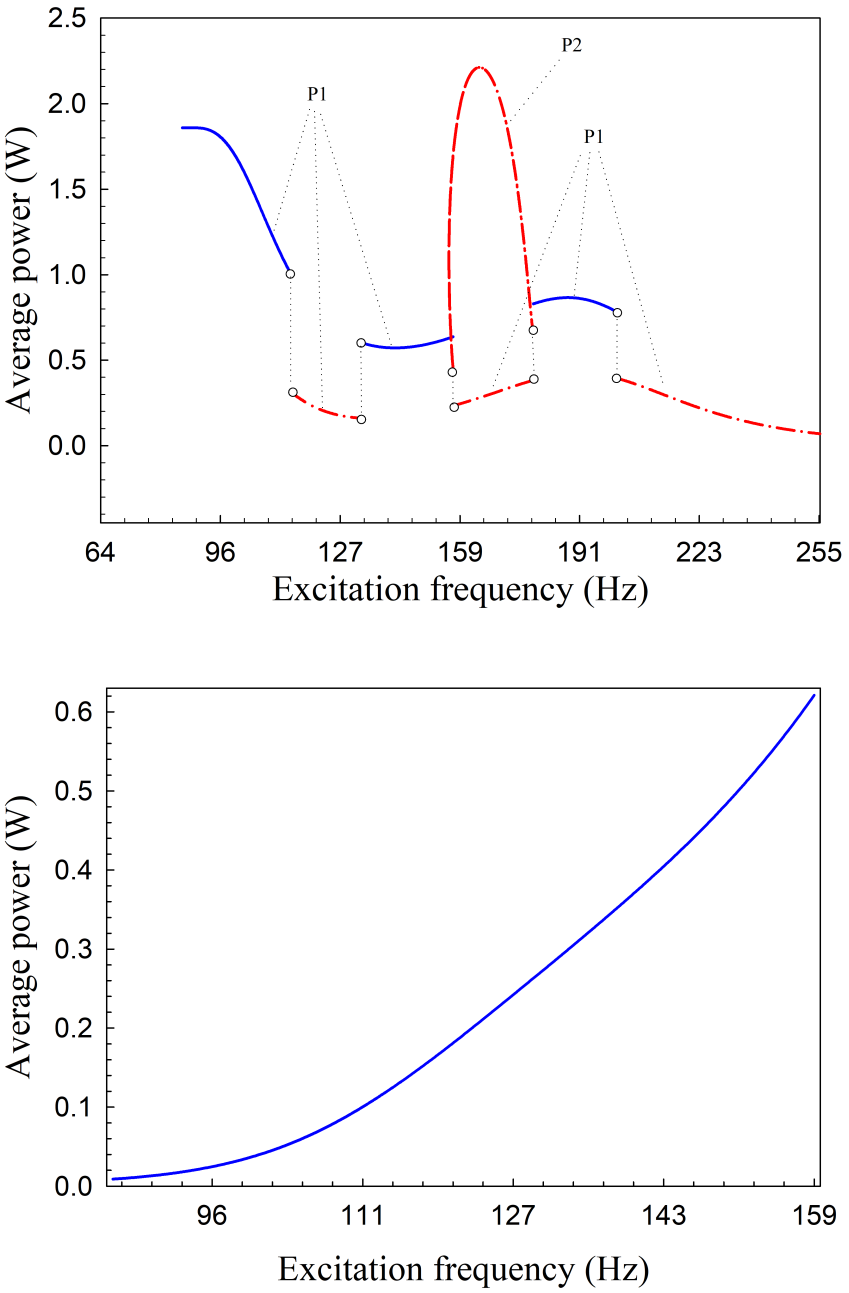

FIGURE A16: Output power comparison between impact-driven PEH and directly excited PEH in the frequency domain of 0 Hz to half of the natural frequency of the PEH: a) Average harvested power versus excitation frequency of the impact-driven system, (b) Average harvested power versus excitation frequency of the directly excited PEH.

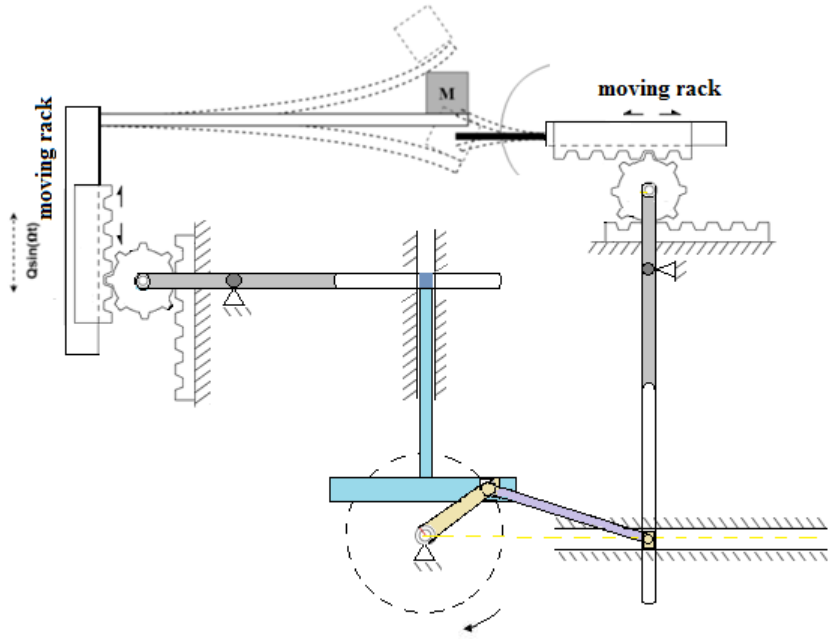

FIGURE A17: Impact-driven piezoelectric energy harvester with controlled impact

Comparing figure A16(a) and figure A16(b), one can see that at low-frequency excitation region, generated power from the impact model is much higher than that from the non-impact model. This shows the efficacy of the proposed impact-driven frequency-up-conversion system. In the future, we will look for other periodic motions in the low-frequency domain to find out the maximum generated power from different periodic motions and, discovering effective factors on the power level of various periodic motions.

3.3 CONTROLLED IMPACT

In previous work, the periodic motion of an impact-driven piezoelectric energy harvester was introduced and investigated via discontinuous dynamics, in that work the impact only occurs on one side of the piezoelectric beam and impacts are determined by initial conditions of vibrations. With these constraints, we found during one excitation period; no single impact periodic solutions are achieved when excitation frequency is less

than 500 (Rad/s). To optimize the energy retrieving from the vibration resource, each impact should be an energy pump in action for the piezoelectric beam. In this work, as shown in Fig.A17 a new system is proposed by adding a pair of rack and pinion gears and a slider crank to control the impact occurring time between the driving beam and the driven beam. In this way, the undesirable stick motion could be removed and guarantee during each impact maximum energy was pumped into the piezoelectric beam from the excitation base. To optimize the energy output from the piezoelectric beam, optimum resistance was calculated and connected to the piezoelectric bimorph. The soft beam is subjected to a base excitation in vertical plane and rack, and pinion and slider crank mechanism are designed to convert the vertical vibration to a horizontal motion with smaller amplitude for the piezoelectric bimorph. This horizontal motion of the piezoelectric beam controls the impact instant between the piezoelectric beam and the plastic driving beam. By properly setting the crank and connecting rod length ratio, after the first impact, the piezoelectric beam will move back a small amount along its longitudinal direction and wait for the soft beam to finish its cycle before the next impact. This assures during each impact the piezoelectric beam is hit by the plastic driving beam at its largest velocity. Hence, the obtained period one motions can maximally pump out of the kinetic energy from the excitation resource. With the new design, the stability of the periodic solutions and bifurcation diagram of periodic solutions' impact time, velocities, displacement are obtained. Harvested power versus the frequency of the base excitation is also calculated.

Discontinuous Mapping

In this study, an impact-driven system, including a driving and a driven beam, has been investigated. Considering an arbitrary motion, t_k is the impact time of the k^{th} impact. Similarly, impact position and after impact velocity of the driven beam are expressed as z_{pk}, $\dot{z}_{pk}^{+}$, respectively. In this study, we have two assumptions, the electric ef-

fects on the dynamic responses of the piezoelectric beam is small and can be neglected, in other words, only the forward mechanical-electric coupling effect is considered in the lumped parameter model of the piezoelectric beam, which is also widely presumed in most studies of piezoelectric energy harvesters. The second assumption we make is the elapsed time during the impacts is neglectable. At the impact instant, the impact time and position of the driving beam equal those of the driven beam. But the after impact velocity of the driving beam will change and is denoted as $\dot{z}_{pk}^{+}$. A constant coefficient of restitution is assumed, and the velocity relations of this implicit map can be presented as:

$$\begin{Bmatrix} \dot{z}_{d_k}^{+} \\ \dot{z}_{p_k}^{+} \end{Bmatrix} = \frac{1}{m_{eq_d} + m_{eq_p}} \begin{pmatrix} 1 & m_{eq_p} \\ 1 & -m_{eq_d} \end{pmatrix} \begin{Bmatrix} m_{eq_d}\dot{z}_{d_k}^{-} + m_{eq_p}\dot{z}_{p_k}^{-} \\ e(\dot{z}_{p_k}^{-} - \dot{z}_{d_k}^{-}) \end{Bmatrix}, \tag{3.29}$$

where e, $\dot{z}_{p}^{-}$ and $\dot{z}_{p}^{-}$ coefficient of restitution, before impact velocities of the driving and driven beams, respectively.

Considering a base excitation with a constant frequency, once the system is excited, the impact vibrations of both beams will settle to a periodic motion with dynamic properties determined by the physical nature of the system. The periodic motions can be defined based on the number of impacts in each cycle of the excitation. The number of impacts per excitation cycle is determined by the excitation frequency, amplitude, the beams natural frequencies, as well as the gap between beams. However, if the tip overlap of two beams is controlled by the small longitudinal shift of the driven beam, the number of the impacts per cycle will not only be altered but also be synchronized so that each impact guarantees there is maximum kinetic energy pumped into the piezoelectric beam from the driving beam. As shown in Fig.A18, the inline crank sliders system shows the 90-degree phase shift between the longitudinal based displacement of the piezoelectric beam and the transverse direction base displacement of the plastic driving beam. Via adjusting the connecting rod length and the offset of the crank slider, we can control the impact occurring instant between the driving beam and the piezoelectric beam during

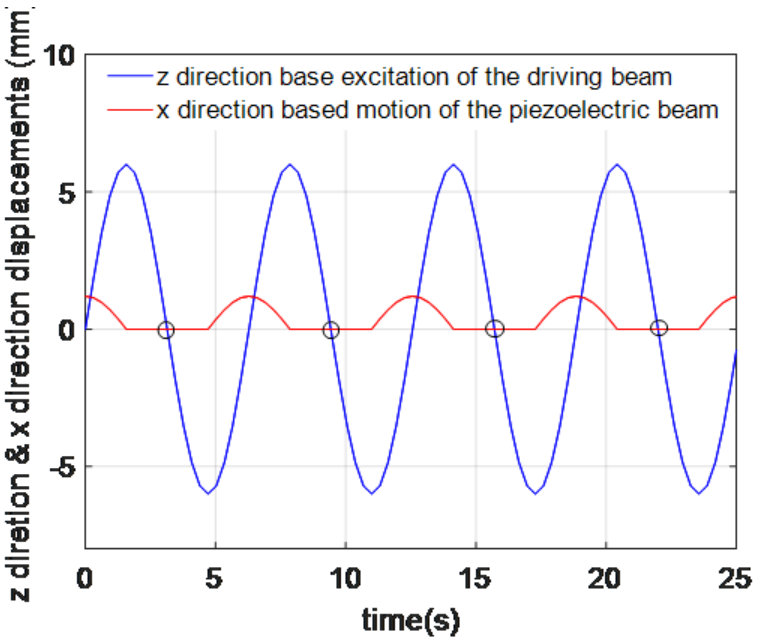

FIGURE A18: The longitudinal direction of the piezoelectric beam and the transverse motion of the driving beam, and small circles represent impacts occur.

one excitation cycle. With crank and connecting rod length ratio 1:1 and motion amplifier levers, Fig.A18 shows the relations of the transverse base excitation of the driving beam and the longitudinal base motion of the piezoelectric beam. One can observe that the mechanism controls the impact instants during one cycle of excitation so that the unfavorable stick motion could be removed. The transient simulations of Figs.A19, A20 and A21 illustrate the advantage of impact controlling. We fix the base excitation amplitude, frequency, and initial conditions, Fig.A19 (a), A20 (a), and A21 (a) are the tip points displacements, output voltage, and output power of an impact driven piezoelectric bimorph without impact controlling mechanism. While Fig.A19 (b), A20 (b), and A21 (b) are the displacement, voltage, and power output of the same impact-driven bimorph but adding the impact controller. Let's first look at the none impact-controlled case, from the driving beam and the driven beam displacements of Fig. A19(a), we see in one period, there are impacts, chattering, and stick motions. Fig.A20(a) shows that

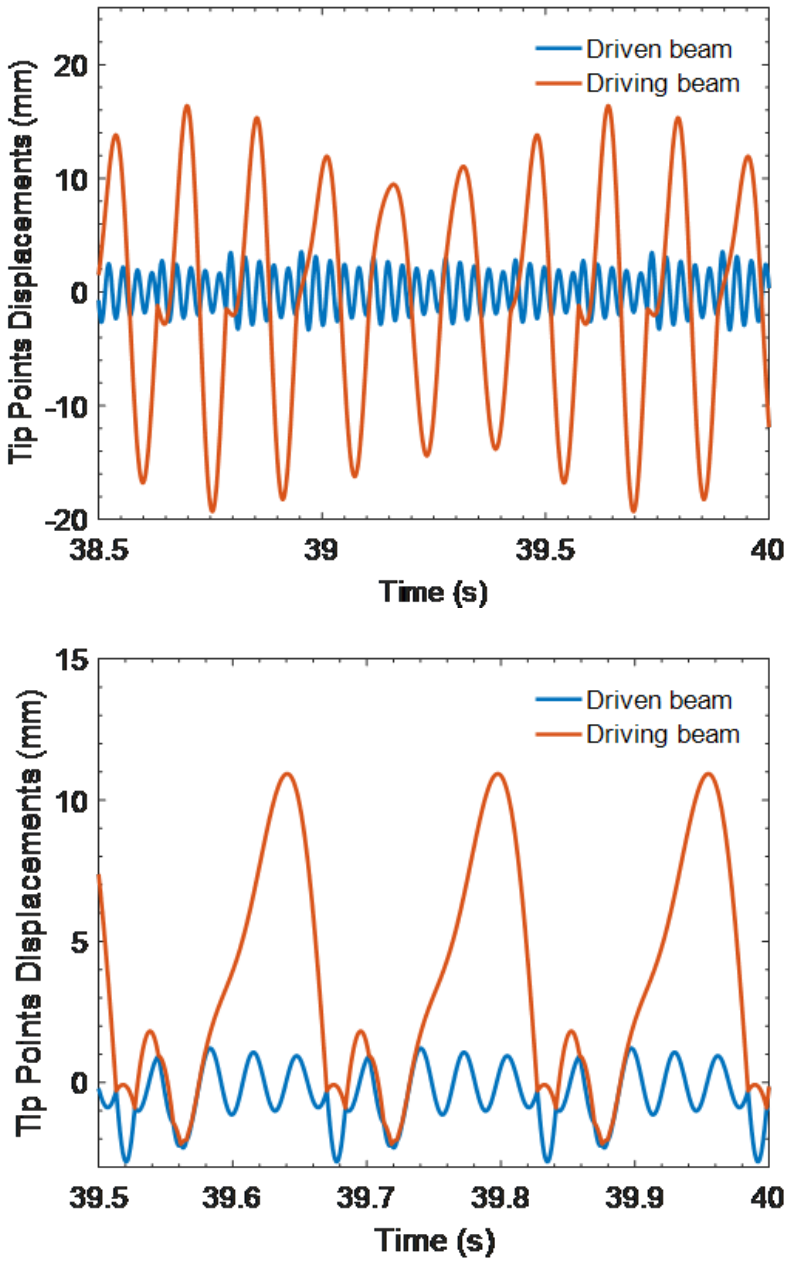

FIGURE A19: Motion comparison between cases with and without impact controller. (a) Tip points displacements of none impact-controlled case; (b) Tip points displacements of impact-controlled case;

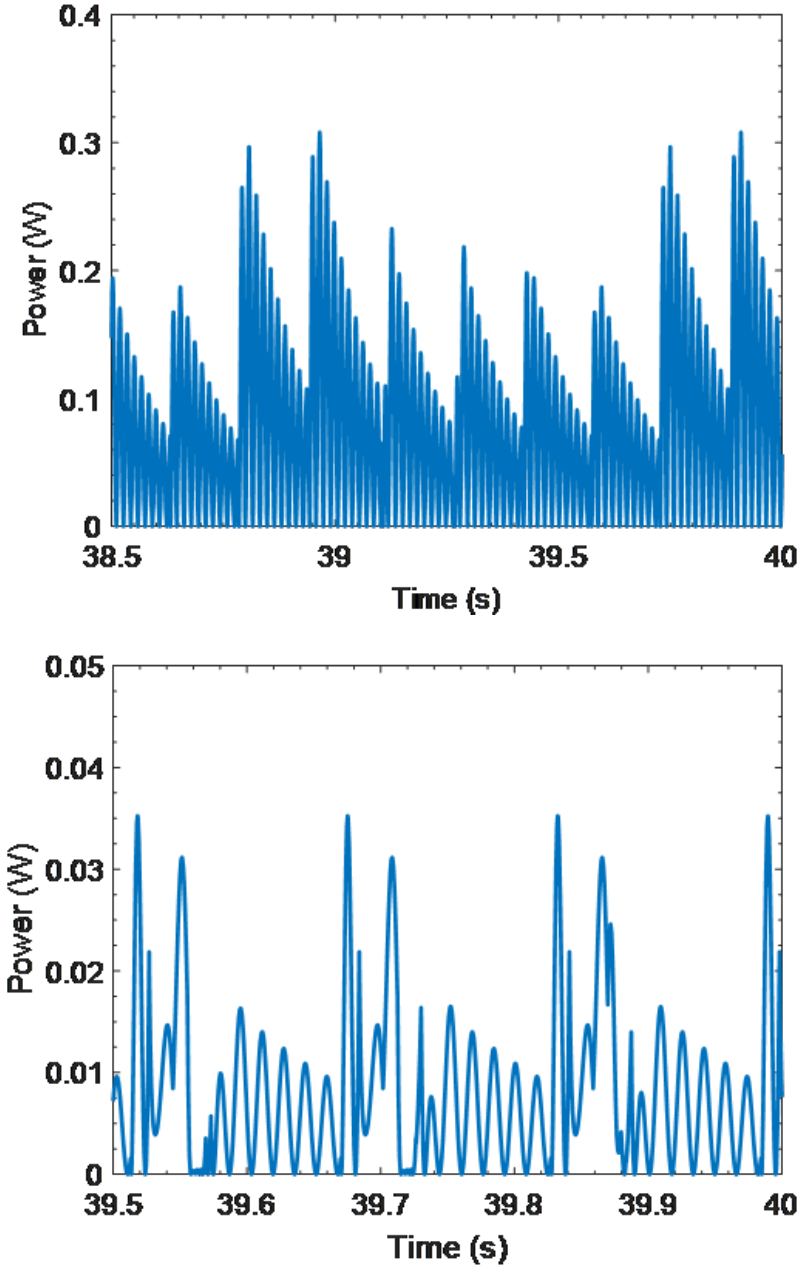

FIGURE A20: harvested power comparison between cases with and without impact controller. (a) output voltage of none impact-controlled case; (b) output voltage of impact-controlled case;

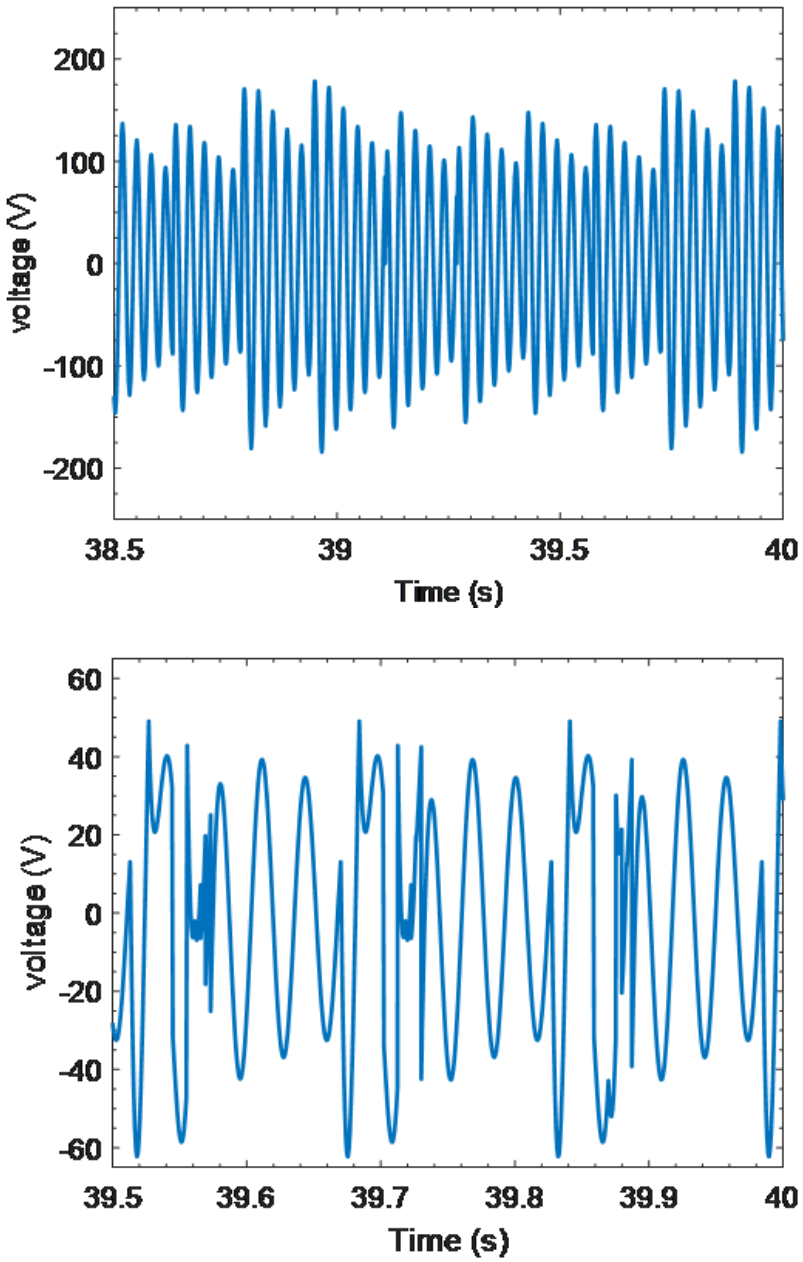

FIGURE A21: Generated voltage comparison between cases with and without impact controller. (e) output power of none impact-controlled case; (f) output power of impact-controlled case.

in one period, only the first impact generates large voltage and output power. Hence it transfers the kinetic energy of the driving beam to the piezoelectric bimorph. The following impact causes voltage drop because of the kinetic energy of the piezoelectric bimorph bumped back to the driving beam. The following chattering and stick motion further reduce the output voltage. Now let us look at the case with impact controller, from Fig.A19 (b), we can see that after the first impact that the kinetic energy of the driving beam is retrieved into the piezoelectric bimorph, the controller moves the piezoelectric beam back to avoid the second impact with the driving beam. Hence, the piezoelectric beam can experience a short time of free vibrations and transfer its kinetic energy into electric energy instead of pumping back to the driving beam. As the sticking motions removed from the periodic solutions in the impact- controlled case, the output voltage increased about three times via comparing Fig.A20 (a) and A20 (b). The output power of the impact-controlled case is augmented almost ten times based on the comparison between Fig.A21 (a) and A21 (b).

In the following analysis, discontinuous mapping will be applied to obtain the periodic solution. A general periodic motion with k impacts in each cycle can be defined as:

$$P_n : (t_n, z_{d_n}, z_{p_n}, \dot{z}_{d_n}, \dot{z}_{p_n}) \Rightarrow (t_{n+k}, z_{d_{n+k}}, z_{p_{n+k}}, \dot{z}_{d_{n+k}}, \dot{z}_{p_{n+k}}). \tag{3.30}$$

In this study, period-1 motion refers to a periodic motion with one impact in each excitation cycle. Period-2 motion is defined as a motion that repeats itself in every two impacts during two excitation cycles and it is bifurcated from a period-1 solution. The expression of the above motions can be shown in below equations:

$$(t_n, z_{d_n}, z_{p_n}, \dot{z}_{d_n}, \dot{z}_{p_n}) \Rightarrow P_1(t_{n+1}, z_{d_{n+1}}, z_{p_{n+1}}, \dot{z}_{d_{n+1}}, \dot{z}_{p_{n+1}}). \tag{3.31a}$$

$$\begin{bmatrix} (t_n, z_{d_n}, z_{p_n}, \dot{z}_{d_n}, \dot{z}_{p_n}) \\ (t_{n+1}, z_{d_{n+1}}, z_{p_{n+1}}, \dot{z}_{d_{n+1}}, \dot{z}_{p_{n+1}}) \end{bmatrix} = P_2 \begin{bmatrix} (t_{n-2}, z_{d_{n-2}}, z_{p_{n-2}}, \dot{z}_{d_{n-2}}, \dot{z}_{p_{n-2}}) \\ (t_{n-1}, z_{d_{n-1}}, z_{p_{n-1}}, \dot{z}_{d_{n-1}}, \dot{z}_{p_{n-1}}). \end{bmatrix} \tag{3.31b}$$

Using the Equ. (3.31a) and Equ. (3.31b), the implicit relations of displacement and velocity of the system can be represented as:

$$
\begin{aligned}
&z_{p_k} = z_{d_k} = z_k \\
&z_k = e^{-\zeta_d \omega_{n_d}(t_k - t_{k-1})}\Big[C_{s_d}\sin(\omega_{d_d}(t_k - t_{k-1})) + C_{c_d}\cos(\omega_{d_d}(t_k - t_{k-1}))\Big] \\
&+ A\sin(\Omega t_k) + B\cos(\Omega t_k) \\
&z_k = e^{-\zeta_p \omega_{n_p}(t_k - t_{k-1})}\Big[C_{s_p}\sin(\omega_{d_p}(t_k - t_{k-1})) + C_{c_p}\cos(\omega_{d_p}(t_k - t_{k-1}))\Big] \\
&\dot{z}_{d_k}^{-} = e^{-\zeta_d \omega_{n_d}(t_k - t_{k-1})}\Big[(C_{s_d}\omega_{dd} - C_{c_d}\zeta_d\omega_{n_d})\cos(\omega_{d_d}(t_k - t_{k-1})) \\
&- (C_{s_d}\omega_{n_d} + C_{c_d}\omega_{d_d})\sin(\omega_{d_d}(t_k - t_{k-1}))\Big] + A\Omega\cos(\Omega t_k) \\
&- B\Omega\sin(\Omega t_k) \\
&\dot{z}_{p_k}^{-} = e^{-\zeta_p \omega_{n_p}(t_k - t_{k-1})}\Big[(C_{s_p}\omega_{dp} - C_{c_p}\zeta_p\omega_{n_p})\cos(\omega_{d_p}(t_k - t_{k-1})) \\
&- (C_{s_p}\omega_{n_p} + C_{c_p}\omega_{d_p})\sin(\omega_{d_p}(t_k - t_{k-1}))\Big],
\end{aligned}
\tag{3.32}
$$

where;

$$
\begin{aligned}
\omega_{ni} &= \sqrt{\frac{k_{eq_p}}{m_{eq\,p}}}, \quad i = p, d \\
\zeta_i &= \frac{c_{eq_i}}{2\sqrt{k_{eq_i} m_{eq_i}}}, \quad i = p, d \\
\omega_{d_i} &= \sqrt{1 - \zeta_i^2}\,\omega_{n_i}, \quad i = p, d
\end{aligned}
\tag{3.33}
$$

and C_{s_d},C_{c_d} are the sine and cosine coefficient extracted from initial conditions and A, B are the particular solution constants of the driving beam, respectively. Similarly, C_{s_p}, C_{c_p} are the initial condition constants for the driven beam. According to Equ. (3.31a) and Equ. (3.32), the discrete impact mapping functions for period-1 motion can be defined

as:

$$
\begin{aligned}
&F_k^1(t_k, z_k, t_{k-1}, z_{k-1}, \dot{z}_{d_{k-1}}^+, \dot{z}_{p_{k-1}}^+) = z_k - z_{k-1} = 0 \\
&F_k^2(t_k, z_k, \dot{z}_{d_k}^+, \dot{z}_{p_k}^+, t_{k-1}, z_{k-1}, \dot{z}_{d_{k-1}}^+, \dot{z}_{p_{k-1}}^+) = \dot{z}_{d_k}^+ - \dot{z}_{d_{k-1}}^+ = 0 \\
&F_k^3(t_k, z_k, t_{k-1}, z_{k-1}, \dot{z}_{d_{k-1}}^+, \dot{z}_{p_{k-1}}^+) = z_{k-1} - z_{k-1} = 0 \\
&F_k^4(t_k, z_k, \dot{z}_{d_k}^+, \dot{z}_{p_k}^+, t_{k-1}, z_{k-1}, \dot{z}_{d_{k-1}}^+, \dot{z}_{p_{k-1}}^+) = \dot{z}_{p_{k-1}}^+ - \dot{z}_{p_{k-1}}^+ = 0,
\end{aligned}
\tag{3.34}
$$

Solving the above equations simultaneously will lead to the bifurcation graph of the period-1 motion. The local stability of period-1 can be analyzed through the corresponding stability Jacobian matrix:

$$
DP = DP_1^{-1} \cdot DP_0 = \left[\frac{\partial \mathbf{F}_{k+1}}{\partial \mathbf{X}_k}\right]^{-1} \left[\frac{\partial \mathbf{F}_k}{\partial \mathbf{X}_{k-1}}\right], \tag{3.35}
$$

where $\mathbf{X} = [t_k, z_k, \dot{z}_{d_k}, \dot{z}_{p_k}]^T$ and $\mathbf{F}_k = [F_k^1, F_k^2, F_k^3, F_k^4]^T$ For eigenvalue analysis:

If all $|\lambda_i| < 1$ for $(i = 1, 2, 3, 4)$, the periodic motion is stable.

If one of $|\lambda_i| > 1$ for $(i \in \{1, 2, 3, 4\})$, the periodic motion is unstable.

If one of $\lambda_i = -1$ and $|\lambda_j| < 1$ for $(i, j \in \{1, 2, 3, 4\}$ and $i \neq j)$, the period-doubling bifurcation of periodic motion occurs.

If one of $\lambda_i = 1$ and $|\lambda_j| < 1$ for $(i, j \in \{1, 2, 3, 4\}$ and $i \neq j)$, the saddle-node bifurcation of the periodic motion occurs.

If $|\lambda_{i,j}| = 1$ is a pair of complex Eigenvalues, the Neimark bifurcation of the periodic motion occurs.

3.4 NUMERICAL SIMULATION

In this section, different types of motions of the proposed piezoelectric energy harvester system are studied, and the bifurcation diagrams of the periodic solution of the impact-driven motions are obtained. The numerical predictions of the output voltage and power of period-1 to period-2 motions are also examined. The slider crank mechanism generates a horizontal movement for the piezoelectric beam so the driving beam and the

driven beam can pass each other without impact. The benet of such a design is that the soft beam hits the piezoelectric beam with maximum energy transforming into the harvester.

The base excitation amplitude is 5(cm) and frequency $\Omega = 15.12$ Hz. Figs. A22(a) and A23(a) are the voltage and power output of the non-impact case, in which the piezoelectric bimorph is directly subjected the same base excitation as the impact case. For an impact-driven system, periodic motions are the simplest ones to study. Figs.A22 (b) and A23(b) are the output voltage and output power of a period-1 solution of our designed impact controlled piezoelectric harvester. The impact driven system produces more voltage and power than a non-impact piezoelectric beam with the same base excitation conditions. This conclusion is observed by comparing Figs.A22 (a) and A22(b) with Figs. A23(a) and A23(b). As we can see that, the output voltage amplitude of the impact driven bimorph is about 15 times larger than that of the non-impact case. Hence, the output power amplitude of the impact case is more than 200 times bigger than that of the non-impact case. Figs.A26 and Figs.A27 Show the output voltage and output power of the stable period-2 motion and the stable period-1 motion with the same base excitation frequency and amplitude. Comparing Fig.A24 (a) and Fig.A24 (b) with Fig.A25 (a) and Fig.A25 (b), with the same based excitation amplitude, although the impact numbers of the period-2 solution is almost doubled during the same time period, the period-2 vibration does not produce more power. The reason for the period-1 motion transfers more energy to the piezoelectric beam compared to period-2 motion is that the period-1 solution happens when the driving beam hits the piezoelectric beam with a larger velocity. On the other hand, for the case of a period-2 solution we found, when the driving beam encounters with the piezoelectric beam, the driving beam's velocity is low which is close to the zero velocity point. With the base excitation amplitude fixed, as the base excitation frequency increases, the vibration amplitude of the driving beam decreases due to the base excitation frequency is further away from the natural frequency of the

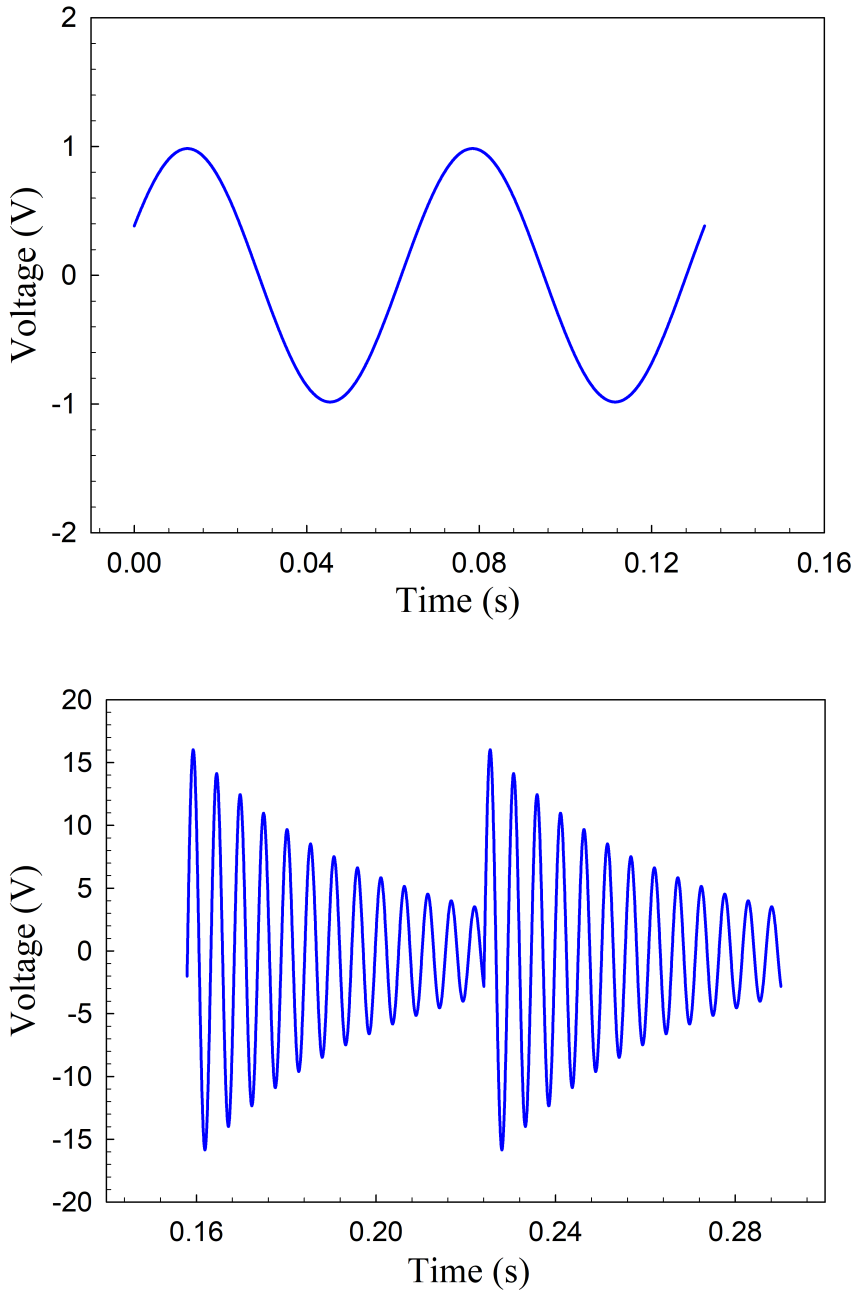

FIGURE A22: output voltage comparison between the non-impact piezoelectric energy harvester and impact piezoelectric energy harvester. Excitation frequency Ω= 15.12 Hz and excitation amplitude 5cm, (a) output voltage of the non-impact harvester; (b) output voltage of the impact harvester;

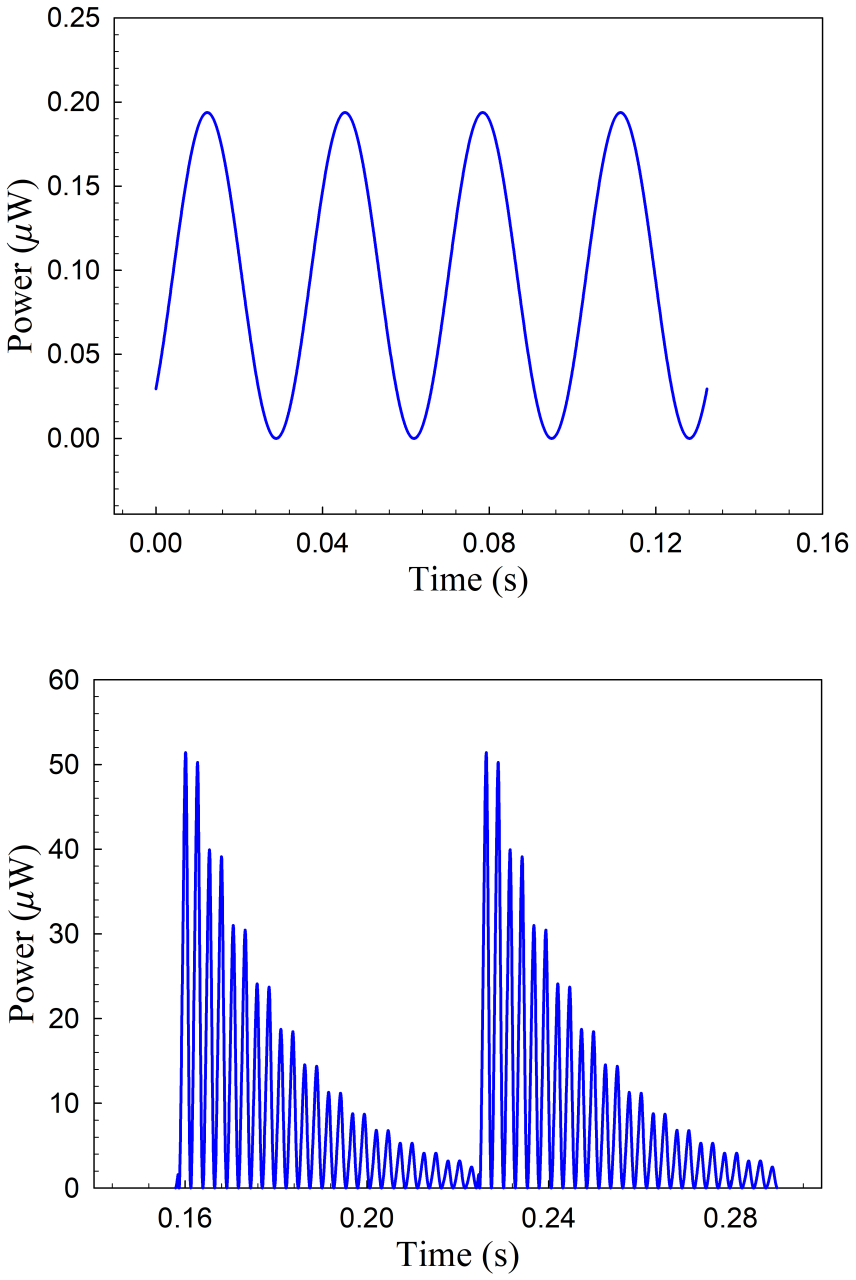

FIGURE A23: output voltage comparison between the non-impact piezoelectric energy harvester and impact piezoelectric energy harvester. Excitation frequency Ω= 15.12 Hz and excitation amplitude 5cm, (a) output power from the non-impact harvester; (b) output power from the impact harvester.

driving beam. If the gap between the driving beam and the piezoelectric driven bimorph does not change, the impact velocity of the driving beam will become smaller. In this section, the bifurcation diagrams of periodic motions are presented via studying the analytic solutions of period-1 to period-2 motions. Without losing generality, a set of system parameters are considered as Q=1 mm and e = 0.9, as the base excitation amplitude and the coefcient of restitution. As the excitation frequency varies, the bifurcation diagram of impact time, switching displacements and switching velocities of the periodic solutions are shown in Figs. A28 and A29, where the solid blue and red dashed lines represent the stable and unstable motions for period-1, and solid green and dashed dark red lines stand for stable and unstable period-2 motion, respectively. The generated power and voltage of the proposed system are compared to a conventional energy harvesting beam, which is directly subjected to the same base excitation. From the comparison between Figs. A30 (a) and A30 (b), we can see that in the low-frequency region, that is the base excitation frequency is much smaller than the natural frequency of the piezoelectric bimorph, the energy harvesting performance of the impact system is much better than that of the non-impact system. From Fig.A30 (b), we can see as the based excitation frequency equals 4 Hz, the impact system can generate 60 (W) power, while the non-impact system case produces almost zero power. Even in the frequency domain between 8 Hz to 40 Hz, the average power generated from the impact system is much higher than those obtained from the non-impact system. However, as the excitation frequency continuously approaches to the natural frequency of the piezoelectric bimorph, the non-impact piezoelectric bimorph generates power will more approach to the power output of the impact system. That is because as the excitation frequency becomes closer to the natural frequency of the bimorph, resonance vibrations stimulate considerable stress of the piezoelectric bimorph in the non-impact system. When the vibration source only contains low-frequency vibrations, the frequency-up converse phenomena induce by impacts will improve the energy harvesting efficiency for obvious.

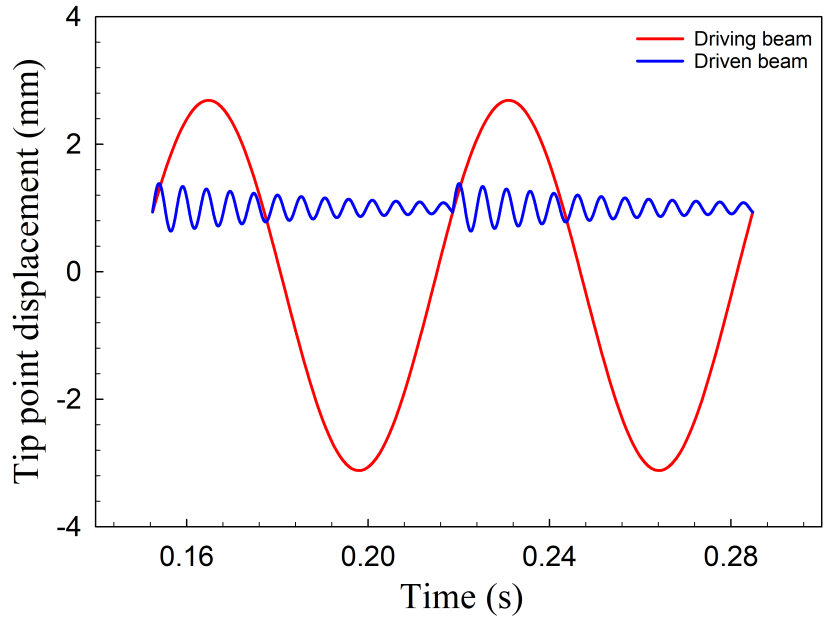

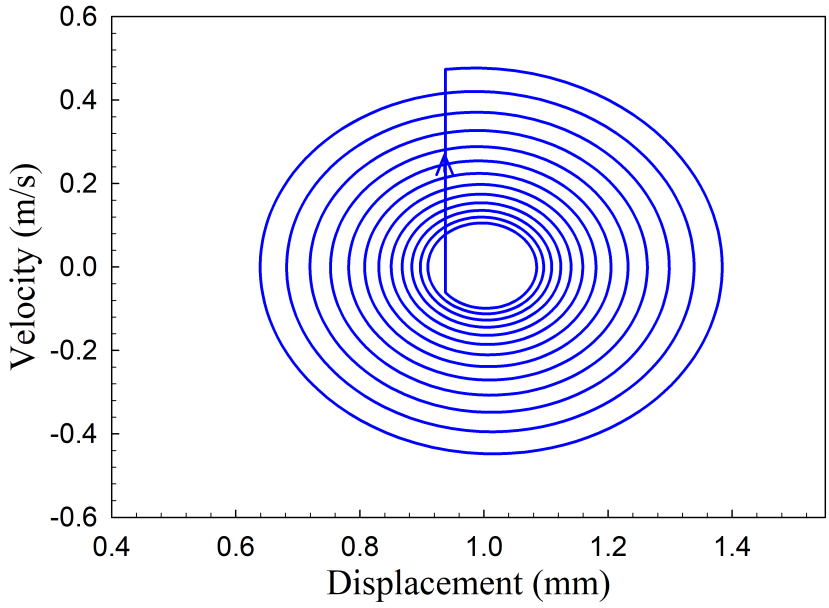

FIGURE A24: Period-1 at Ω=15.12 Hz, (a) tip points displacement of both beams of the period-1 solution; (b) Phase diagram of the Period-1 motion,

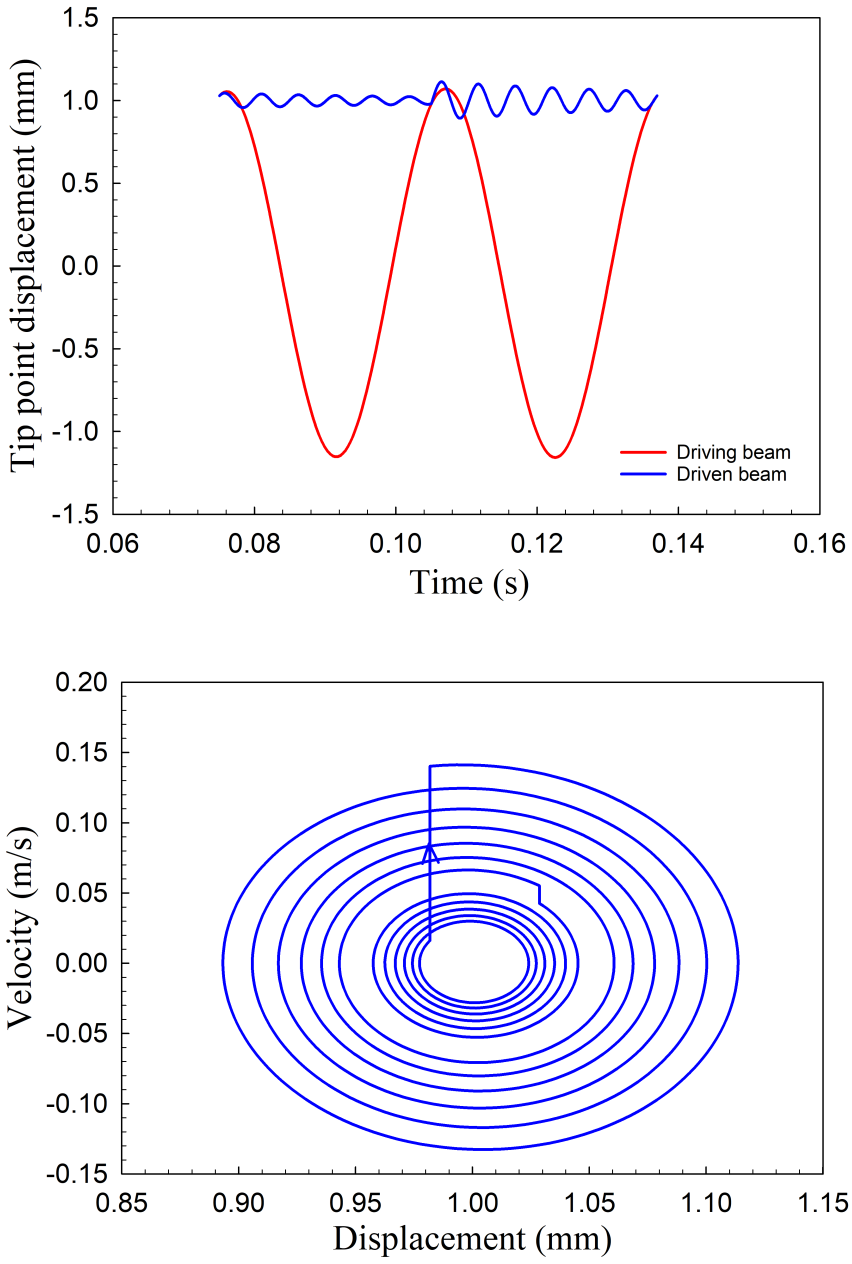

FIGURE A25: Period-2 at Ω=15.12 Hz, (a) tip points displacement of both beams of the period-2 solution; (b) Phase diagram of the period-2 motion.

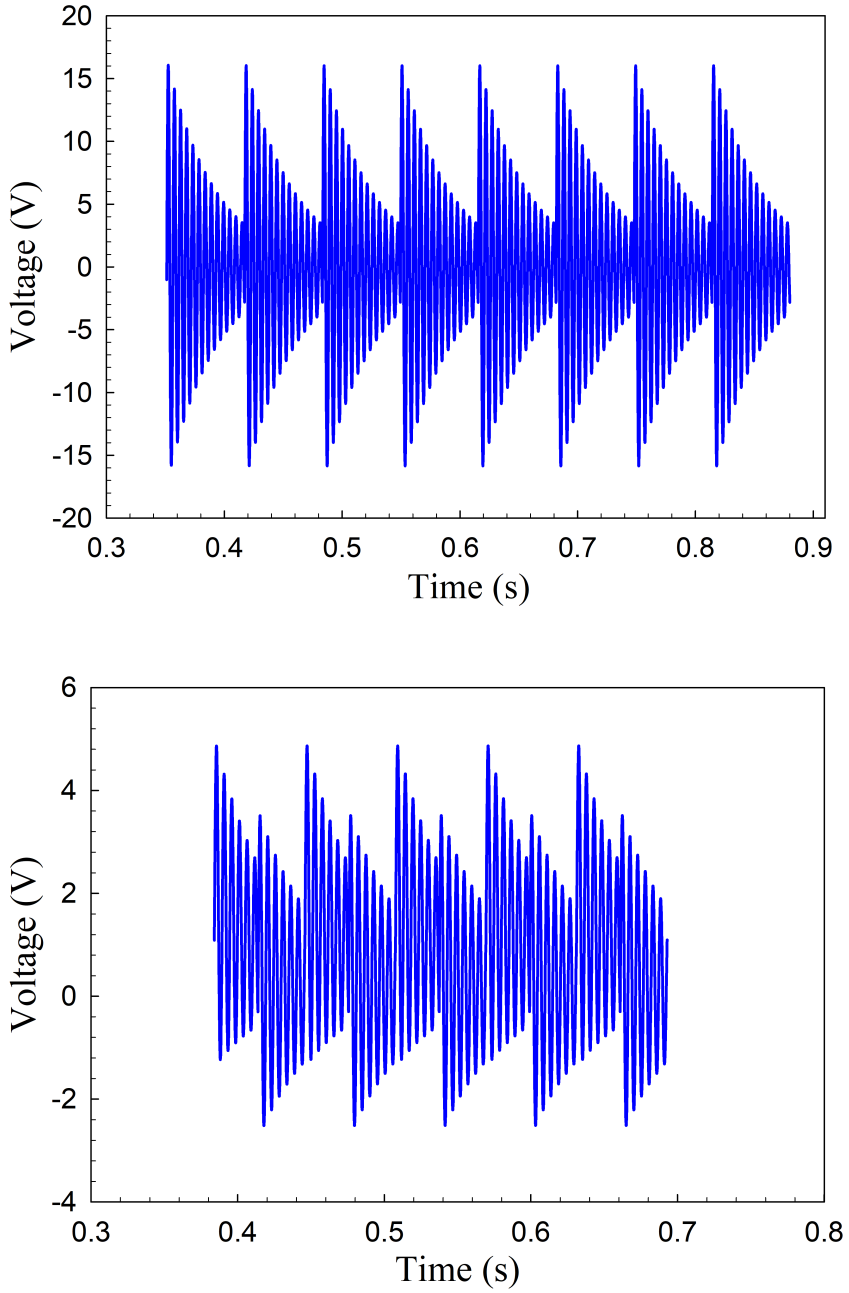

FIGURE A26: Comparison between the proposed system at period-1 motion and period-2 motion at $\Omega = 15.12$ Hz, (a) output voltage of period-1 solutions; (a) output voltage of period-2 solutions; (c) Output power of period-1 solutions; (d) Output power of period-2 solutions

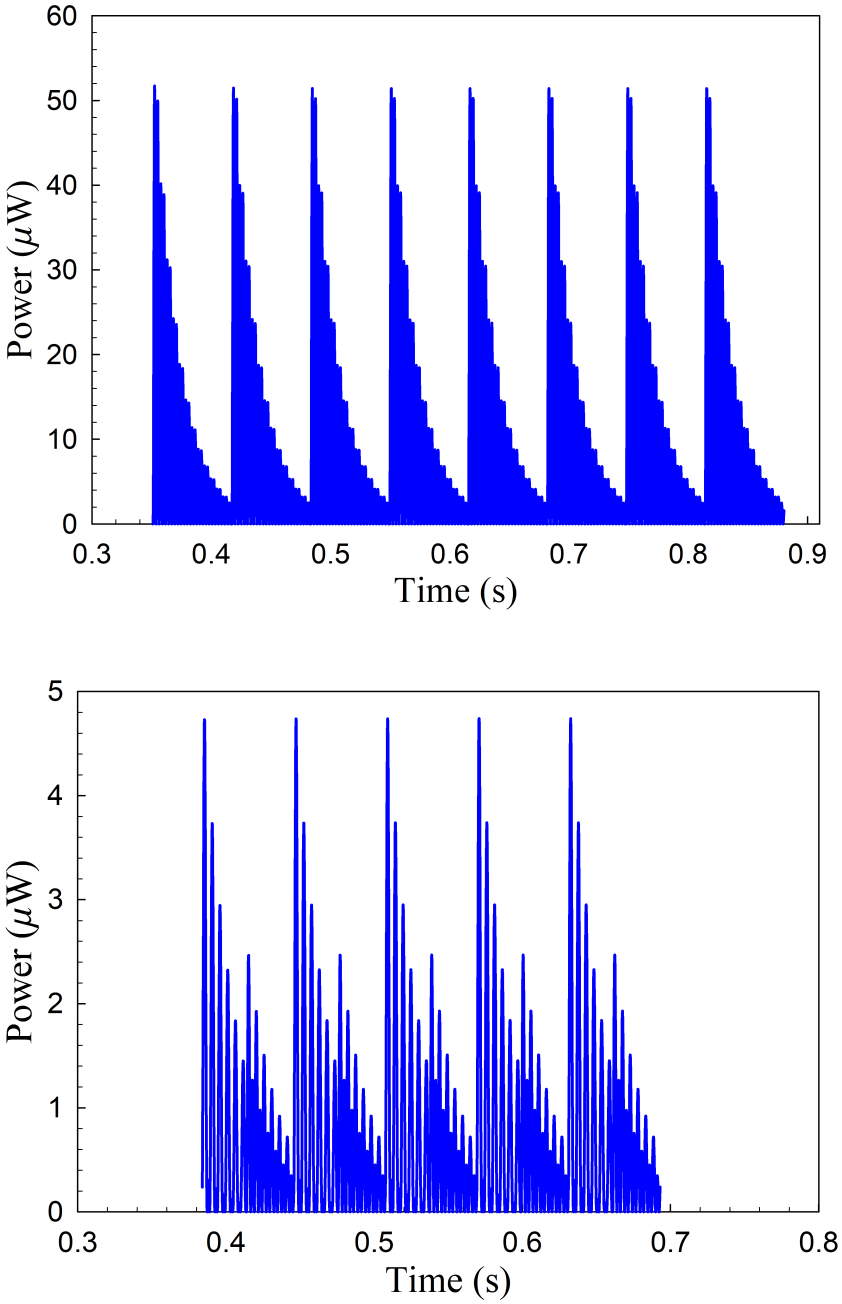

FIGURE A27: Comparison between the proposed system at period-1 motion and period-2 motion at $\Omega = 15.12$ Hz, (a) Output power of period-1 solutions; (b) Output power of period-2 solutions.

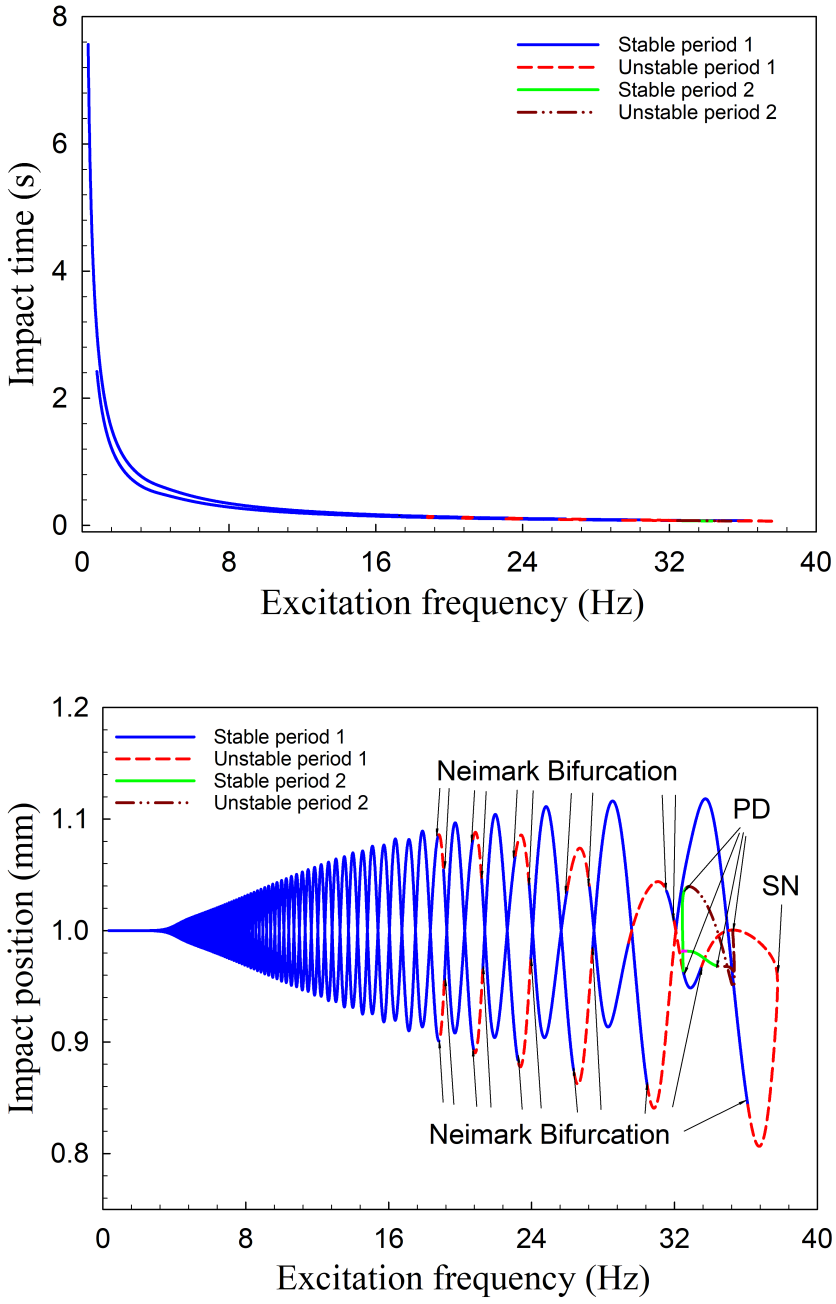

FIGURE A28: Bifurcation diagrams of the proposed system (a) Impact time vs excitation frequency, (b) Impact positions of the impact-driven system vs excitation frequency,

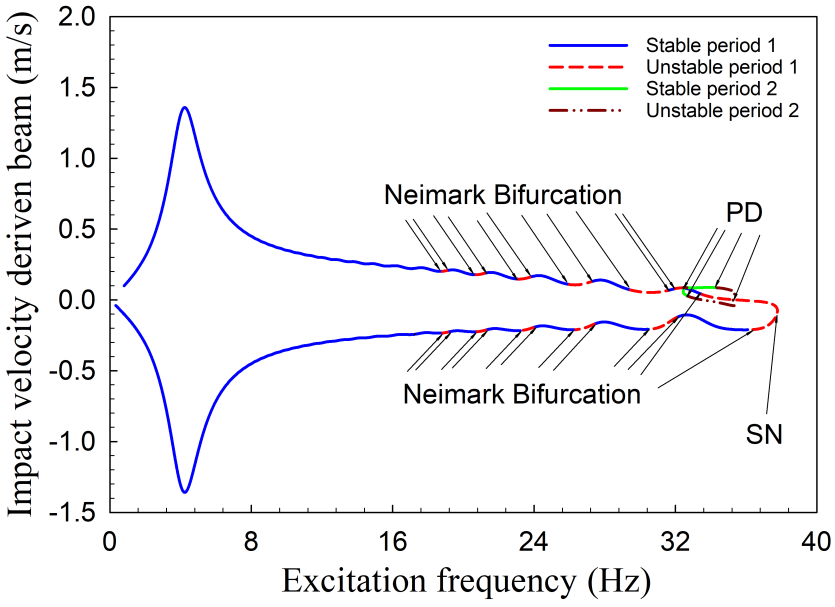

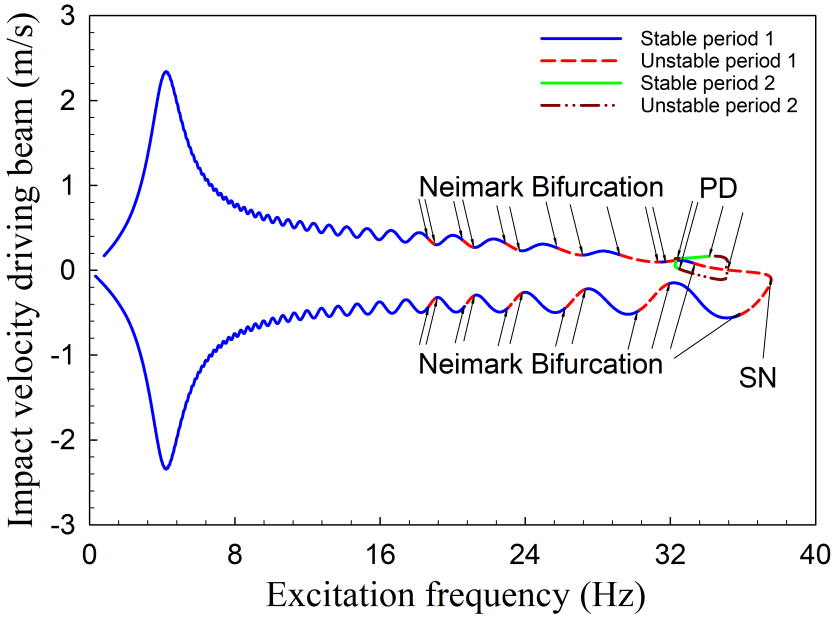

FIGURE A29: Bifurcation diagrams of the proposed system (a) After impact velocity of the piezoelectric beam vs excitation frequency, (b) After impact velocity of the soft driving beam vs excitation frequency.

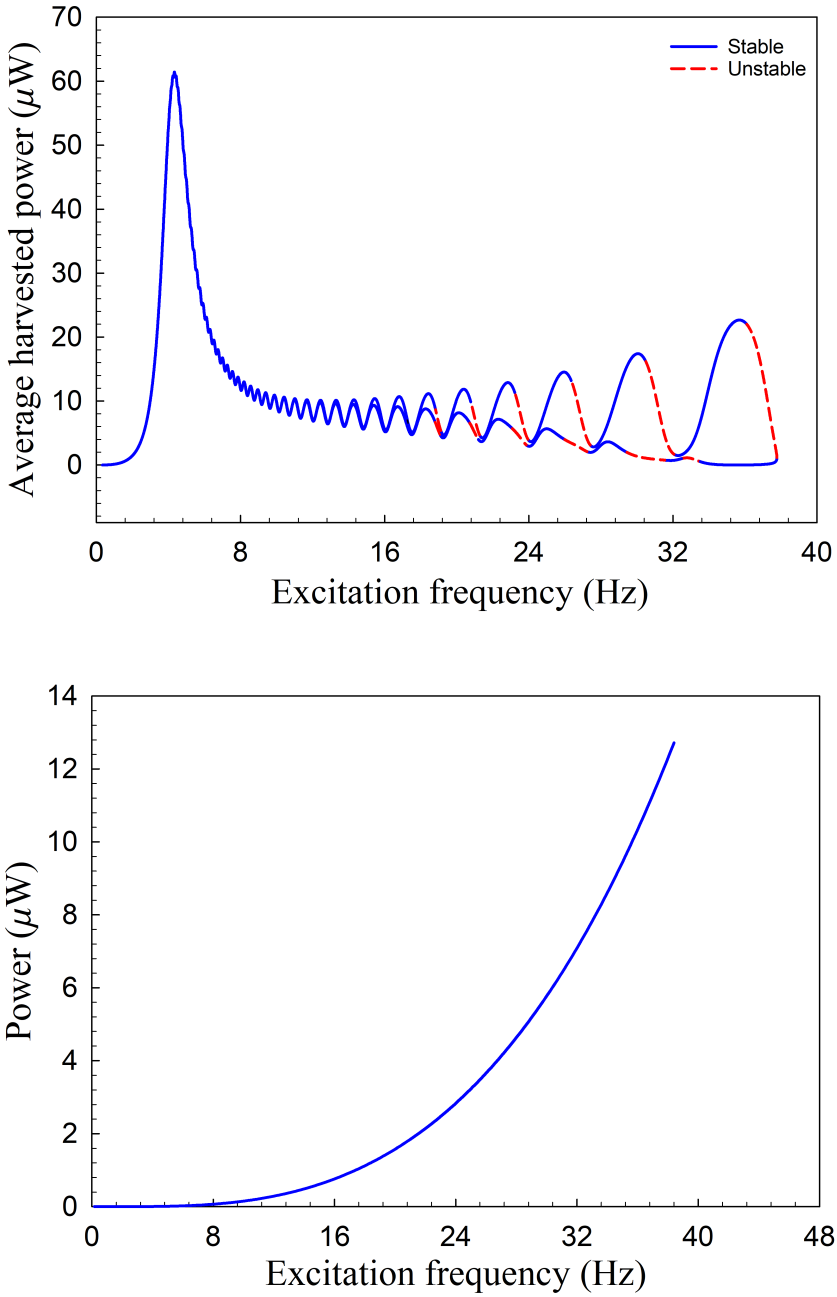

FIGURE A30: (a) Average harvested power from the impact driven system vs excitation frequency, (b) Average harvested power from a simple piezoelectric beam with base excitation vs excitation frequency.

CHAPTER 4

EULER-BERNOULLI BEAM MODEL

4.1 EULER-BERNOULLI BEAM EQUATION

For a piezoelectric beam in Fig.A1, the total kinetic energy T and the total potential energy U are written as,

$$T = \frac{1}{2}\int_{V_s} \rho_s(\dot{A}(t) + \dot{w}(x,t))^2 dV_s + \frac{1}{2}\int_{V_p} \rho_p(\dot{A}(t) + \dot{w}(x,t))^2 dV_p \tag{4.1a}$$

$$U = \frac{1}{2}\int_{V_s} Y_s S_1^2 dV_s + \frac{1}{2}\int_{V_p} c_{11} S_1^2 dV_p - \frac{1}{2}\int_{V_p} e_{31} S_1 E_3 dV_p - \frac{1}{2}\int_{V_p} \epsilon_{33} E_3^2 dV_p. \tag{4.1b}$$

where V_p and V_s are the volume of the piezoelectric material and the volume of the substrate, respectively. $w(x,t)$ represents the deformed bending direction displacements of a point on the neutral surface relative to the unreformed position. S_1 is the normal strain of an arbitrary point across the thickness of the bimorph. With the linear mechanical-electrical constitutive law, the electric field generated by the elastic strain on the top and bottom piezoelectric lays can be written as,

$$E(z,t) = \phi(z)V(t) = \begin{cases} -\frac{|z|v_A}{zh_p}, & \frac{h_s}{2} \le |z| \le \frac{h_s}{2} + h_p \\ 0, & 0 \le |z| < \frac{h_s}{2}, \end{cases} \tag{4.2}$$

with $V(t)$ as the generated AC voltage, h_p and h_s are the thickness of each piezoelectric layer and the thickness of the substrate layer as shown in Fig. A1. With Euler-Bernoulli beam assumption, the normal strain of an arbitrary point across the thickness of the bimorph S_1 can be written as,

$$S_1(x,z) = -z\frac{\partial^2 w(x,t)}{\partial x^2}. \tag{4.3}$$

The work W acting on the PZT bimorph including the impulse caused by the impact at the tip of the beam and the external load resistance can be written as,

$$W = \int_0^L W(x,t)F_0\delta(t-t_*)\delta(x-L)dx - \sum_{j=1}^{nq} V(t)q_j, \tag{4.4}$$

where q is the charge, $F_0\delta(t-t_*)\delta(x-L)$ is the impulse caused by the impact at the tip of the beam, and t_* is the time instant that impact occurs. R is the load resistance connected on the piezoelectric beam. Later on, further analysis will be performed to determine the unknown magnitude of the impulse(F_0). Substituting Equations 4.2 and 4.16 into equation 4.1, then further apply the Hamilton's principle,

$$\int_{t_1}^{t_2}(\delta T-\delta U+\delta W)=0. \tag{4.5}$$

the partial deferential equation will be obtained:

$$YI\frac{\partial^4(w(x,t))}{\partial^4 x}+m\frac{\partial^2(w(x,t))}{\partial^2 t}=0. \tag{4.6}$$

To obtain the discretized equation of motion with one mode on the dynamics part, we write the displacements of the bimorph in terms of the free vibration cantilever modal function $\Phi_1(x)$,

$$w(x,t)=\Phi_1(x)\eta_1(t) \tag{4.7a}$$

$$\Phi_1(x)=C_1\left[\cosh\frac{\beta_1 x}{L}-\cos\frac{\beta_1 x}{L}-\lambda_1(\sinh\frac{\beta_1 x}{L}-\sin\frac{\beta_1 x}{L})\right], \tag{4.7b}$$

where $\beta_1=1.8751$, $\lambda_1=.7341$, and C_1 is the mass normalization coefficient, that is

$$\int_0^L(\rho_s A_s+\rho_p A_p)\Phi_1^2(x)dx=1. \tag{4.8}$$

After add viscous damping, the following coupled equations discretized equations obtained,

$$\ddot{\eta}_1(t)+2\xi_1\omega_1\eta_1(t)+\omega_1^2\dot{\eta}_1(t)+\theta V(t)=-I_1\ddot{A}(t)+\Phi_1(L)F_0\delta(t-t_0), \tag{4.9a}$$

$$-\theta\eta_1(t)+C_pV(t)=q(t), \tag{4.9b}$$

where xi_1 is the damping ratio corresponding to the first mode, $I_1=\int_0^L(\rho_s A_s+\rho_p A_p)\Phi_1(x)dx$, $\theta=-\int_{V_p}z\Phi_1''(x)e_{31}\phi(z)dV_p$, $\omega_1=\beta_1^2\sqrt{\frac{b[(6h_s^2h_p+12h_sh_p^2+8h_p^3)Y_p+h_s^3Y_s]}{12(\rho_sA_s+\rho_pA_p)L^4}}$. For a series connected bimorph, the total capacitance of the piezoelectric beam is written as

$C_p = \frac{1}{2}\int_0^L \int_{t_s/2}^{t_p+t_s/2} b\varepsilon_{33}^S \phi^2(z) dz dx$. with a resistance load the voltage and the charge relation can be written as,

$$V(t) = -Rq(t). \tag{4.10}$$

Therefore the final mechanical-electrical coupling equation can be rewritten as,

$$\ddot{\eta}_1(t) + 2\xi_1\omega_1\dot{\eta}_1(t) + \omega_1^2\eta_1(t) + \theta V(t) = I_1\Omega^2 A_0 \sin\Omega t + \Phi_1(L)F_0\delta(t-t_0), \tag{4.11a}$$

$$-\theta\dot{\eta}_1(t) + C_p\dot{V}(t) = -\frac{V(t)}{R}, \tag{4.11b}$$

As we mentioned before, the impact amplitude will be determined based on the later on impact analysis.

4.1.1 The piezoelectric beam impacts with another plastic beam

Piezoelectric Beam

If we only consider forward coupling and neglect the backward coupling, based on reference [10] (L. Meirovitch, 1997, Principles and Techniques of Vibrations), the solution of equation (10a) can be written as, Before impact,

$$\begin{aligned}\eta_1^-(t) &= \frac{1}{\omega_{1d}} I_1\Omega^2 A_0 \int_0^t \sin(\Omega\tau) e^{-\xi_1\omega_1(t-\tau)} \sin\omega_{1d}(t-\tau) d\tau \\ &+ e^{-\xi_1\omega_1 t}\left(\cos(\omega_{1d}t) + \frac{\xi_1}{\sqrt{1-\xi_1^2}}\sin(\omega_{1d}t)\right)\eta_1(0) + \frac{1}{\omega_{1d}} e^{-\xi_1\omega_1 t}\sin(\omega_{1d}t)\dot{\eta}_1(0),\end{aligned} \tag{4.12}$$

Or

$$\begin{aligned}\eta_1^-(t) &= e^{\zeta_1\omega_1 t}\left(\cos(\omega_{1d}t) + \frac{\xi_1}{\sqrt{1-\xi_1^2}}\right)\eta_1(0) + \frac{1}{\omega_{1d}} e^{-\xi_1\omega_1 t}\sin(\omega_{1d}t)\dot{\eta}_1(0) \\ &+ I_1\Omega^2 A_0 \frac{\frac{\Omega}{\omega_{1d}} e^{-\xi_1\omega_1 t}((\Omega^2 - \omega_1^2 + 2\xi_1^2\omega_1^2)\sin(\omega_{1d}t)) + (\omega_1^2 - \Omega^2)\sin(\Omega t)}{\Omega^4 + 4\xi_1^2\Omega^2\omega_1^2 - 2\Omega^2\omega_1^2 + \omega_1^4} \\ &+ \frac{2\xi_1\omega_1\omega_{1d}\cos(\omega_{1d}t) - 2\xi_1\omega_1\Omega\cos(\Omega t)}{\Omega^4 + 4\xi_1^2\Omega^2\omega_1^2 - 2\Omega^2\omega_1^2 + \omega_1^4},\end{aligned} \tag{4.13}$$

After impact,

$$\begin{aligned}\eta_1^+(t) &= \frac{1}{\omega_{1d}} I_1 \Omega^2 A_0 \int_0^t \sin(\Omega\tau) e^{-\xi_1\omega_1(t-\tau)} \sin\omega_{1d}(t-\tau) d\tau \\ &+ e^{-\xi_1\omega_1 t}\left(\cos(\omega_{1d}t) + \frac{\xi_1}{\sqrt{1-\xi_1^2}}\sin(\omega_{1d}t)\right)\eta_1(0) + \frac{1}{\omega_{1d}} e^{-\xi_1\omega_1 t}\sin(\omega_{1d}t)\dot{\eta}_1(0) \\ &+ \frac{\Phi_1(L)F_0}{\omega_{1d}} e^{-\xi_1\omega_1(t-t_*)}\sin\omega_{1d}(t-t_*),\end{aligned} \tag{4.14}$$

Or expand the integral

$$\begin{aligned}\eta_1^+(t) &= e^{\zeta_1\omega_1 t}\left(\cos(\omega_{1d}t) + \frac{\xi_1}{\sqrt{1-\xi_1^2}}\right)\eta_1(0) + \frac{1}{\omega_{1d}} e^{-\xi_1\omega_1 t}\sin(\omega_{1d}t)\dot{\eta}_1(0) \\ &+ I_1\Omega^2 A_0 \frac{\frac{\Omega}{\omega_{1d}} e^{-\xi_1\omega_1 t}((\Omega^2 - \omega_1^2 + 2\xi_1^2\omega_1^2)\sin(\omega_{1d}t)) + (\omega_1^2 - \Omega^2)\sin(\Omega t)}{\Omega^4 + 4\xi_1^2\Omega^2\omega_1^2 - 2\Omega^2\omega_1^2 + \omega_1^4} \\ &+ \frac{2\xi_1\omega_1\omega_{1d}\cos(\omega_{1d}t) - 2\xi_1\omega_1\Omega\cos(\Omega t)}{\Omega^4 + 4\xi_1^2\Omega^2\omega_1^2 - 2\Omega^2\omega_1^2 + \omega_1^4} + \frac{\Phi_1(L)F_0}{\omega_{1d}} e^{-\xi_1\omega_1(t-t_*)}\sin\omega_{1d}(t-t_*),\end{aligned} \tag{4.15}$$

where $\omega_{1d} = \omega_1\sqrt{1-\zeta_1^2}$. Based on the mass orthonormal conditions of the mode shape functions,

$$\eta_1(0) = \int_0^L (\rho_s A_s + \rho_p A_p)\Phi_1(x) w(x,0) dx \tag{4.16a}$$

$$\dot{\eta}_1(0) = \int_0^L (\rho_s A_s + \rho_p A_p)\Phi_1(x) \dot{w}(x,0) dx, \tag{4.16b}$$

From Equation 4.14, the before impact the tip point velocity can also be rewritten as,

$$\begin{aligned}\dot{w}(L,t_*^-) &= \Phi_1(L)\frac{d\eta_1(t_*^-)}{dt} = \Phi_1(L)\Bigg[- \frac{\omega_1}{\sqrt{1-\xi_1^2}} e^{-\xi_1\omega_1 t_*}\sin(\omega_{1d}t_*)\eta_1(0) \\ &+ I_1\Omega^2 A_0 \int_0^{t_*} \sin(\Omega\tau) e^{-\xi_1\omega_1(t_*-\tau)}\cos\omega_{1d}(t_*-\tau) d\tau \\ &\frac{-\xi_1\omega_1}{\omega_{1d}} I_1\Omega^2 A_0 \int_0^{t_*} \sin(\Omega\tau) e^{-\xi_1\omega_1(t_*-\tau)}\sin\omega_{1d}(t_*-\tau) d\tau \\ &+ \frac{1}{\omega_{1d}} e^{-\xi_1\omega_1 t_*}\big[- \xi_1\omega_1\sin(\omega_{1d}t_*) + \omega_{1d}\cos(\omega_{1d}t_*)\big]\dot{\eta}_1(0)\Bigg],\end{aligned} \tag{4.17}$$

Or expand the integration

$$\dot{w}(L,t_*^-) = \Phi_1(L)\frac{d\eta_1(t_*^-)}{dt} = \Phi_1(L)\Big\{ -\frac{\omega_1}{\sqrt{1-\xi_1^2}}e^{-\xi_1\omega_1 t_*}\sin(\omega_{1d}t_*)\eta_1(0)$$
$$+ I_1\Omega^2 A_0 \frac{\frac{\Omega}{\omega_{1d}}e^{-\xi_1\omega_1 t_*}(\Omega^2-\omega_1^2)\omega_{1d}\cos(\omega_{1d}t_*)}{\Omega^4+4\xi_1^2\Omega^2\omega_1^2-2\Omega^2\omega_1^2+\omega_1^4}$$
$$- \frac{\frac{\Omega}{\omega_{1d}}e^{-\xi_1\omega_1 t_*}(\Omega^2+\omega_1^2)\xi_1\omega_1\sin(\omega_{1d}t_*)+\Omega(\omega^2-\Omega_1^2)\cos(\Omega t_*)+2\xi_1\omega_1\Omega^2\sin(\Omega t_*)}{\Omega^4+4\xi_1^2\Omega^2\omega_1^2-2\Omega^2\omega_1^2+\omega_1^4} \tag{4.18}$$
$$+ \frac{1}{\omega_{1d}}e^{-\xi_1\omega_1 t_*}\big[-\xi_1\omega_1\sin(\omega_{1d}t_*)+\omega_{1d}\cos(\omega_{1d}t_*)\big]\dot{\eta}_1(0)\Big\},$$

Similarly,

$$\dot{w}(L,t_*^+) = \Phi_1(L)\frac{d\eta_1(t_*^+)}{dt} = \Phi_1(L)\Big[-\frac{\omega_1}{\sqrt{1-\xi_1^2}}e^{-\xi_1\omega_1 t_*}\sin(\omega_{1d}t_*)\eta_1(0)$$
$$+ I_1\Omega^2 A_0\int_0^{t_*}\sin(\Omega\tau)e^{-\xi_1\omega_1(t_*-\tau)}\cos\omega_{1d}(t_*-\tau)d\tau + \Phi_1(L)F_0$$
$$\frac{-\xi_1\omega_1}{\omega_{1d}}I_1\Omega^2 A_0\int_0^{t_*}\sin(\Omega\tau)e^{-\xi_1\omega_1(t_*-\tau)}\sin\omega_{1d}(t_*-\tau)d\tau \tag{4.19}$$
$$+ \frac{1}{\omega_{1d}}e^{-\xi_1\omega_1 t_*}\big[-\xi_1\omega_1\sin(\omega_{1d}t_*)+\omega_{1d}\cos(\omega_{1d}t_*)\big]\dot{\eta}_1(0)\Big],$$

Or expand integral

$$\dot{w}(L,t_*^+) = \Phi_1(L)\frac{d\eta_1(t_*^+)}{dt} = \Phi_1(L)\Big\{ -\frac{\omega_1}{\sqrt{1-\xi_1^2}}e^{-\xi_1\omega_1 t_*}\sin(\omega_{1d}t_*)\eta_1(0)$$
$$+ I_1\Omega^2 A_0 \frac{\frac{\Omega}{\omega_{1d}}e^{-\xi_1\omega_1 t_*}(\Omega^2-\omega_1^2)\omega_{1d}\cos(\omega_{1d}t_*)}{\Omega^4+4\xi_1^2\Omega^2\omega_1^2-2\Omega^2\omega_1^2+\omega_1^4} + \Phi_1(L)F_0$$
$$- \frac{\frac{\Omega}{\omega_{1d}}e^{-\xi_1\omega_1 t_*}(\Omega^2+\omega_1^2)\xi_1\omega_1\sin(\omega_{1d}t_*)+\Omega(\omega^2-\Omega_1^2)\cos(\Omega t_*)+2\xi_1\omega_1\Omega^2\sin(\Omega t_*)}{\Omega^4+4\xi_1^2\Omega^2\omega_1^2-2\Omega^2\omega_1^2+\omega_1^4} \tag{4.20}$$
$$+ \frac{1}{\omega_{1d}}e^{-\xi_1\omega_1 t_*}\big[-\xi_1\omega_1\sin(\omega_{1d}t_*)+\omega_{1d}\cos(\omega_{1d}t_*)\big]\dot{\eta}_1(0)\Big\},$$

Plastic Beam

Neglect the backward electric effect on the dynamics of the piezoelectric beam. Assume the bending deformation of the plastic beam is denoted by $w_b(x_b,t) = \Psi_1(x_b)\xi_1(t)$, where $\Psi_1(x_b)$ is the first bending mode normalized with the mass of the plastic beam. According to Equation 4.11, the discretized one mode plastic beam equation can be writ-

ten as,

$$\ddot{\zeta}_1(t) + 2\xi_{1b}\omega_{1b}\dot{\zeta}_1(t) + \omega_{1b}^2\zeta_1(t) = I_{1b}\Omega_b^2 B_0 \sin\Omega_b t - \Psi_1(L_b)F_0\delta(t-t_0), \tag{4.21}$$

where L_b is the length of the plastic beam, Ω_b is the base excitation frequency of the beam, ω_{1b} is the first natural frequency of the plastic beam, ξ_{1b} is the damping ratio. Similarly, $I_{1b} = \int_0^{L_b} \rho_b A_b \Psi_1(x_b)dx_b$. Note that comparing equation 4.11 and 4.21, one can find the impulse due to impact are action and reaction forces for the two beams, i.e. they are the same magnitude opposite directions. with the restitution coefficient is between the tips of two beams, we have,

$$e = \frac{\dot{w}(L, t_*^+) - \dot{w}_b(L_b, t_*^+)}{\dot{w}_b(L_b, t_*^-) - \dot{w}(L, t_*^-)} \tag{4.22}$$

which leads us to:

$$\begin{aligned}
\dot{w}_b(L_b, t_*^-) = \Psi_1(L_b)\Bigg[& \frac{-\xi_{1b}\omega_{1b}}{\omega_{1d}} I_{1b}\Omega_b^2 B_0 \int_0^{t_*} \sin(\Omega_b\tau) e^{-\xi_{1b}\omega_{1b}(t_*-\tau)} \sin\omega_{1bd}(t_*-\tau)d\tau \\
& + I_{1b}\Omega_b^2 B_0 \int_0^{t_*} \sin(\Omega_b\tau) e^{-\xi_{1b}\omega_{1b}(t_*-\tau)} \cos\omega_{1bd}(t_*-\tau)d\tau - \frac{\omega_{1b}}{\sqrt{1-\xi_{1b}^2}} e^{-\xi_1\omega_{1b}t_*} \sin(\omega_{1bd}t_*)\zeta_1(0) \\
& - \frac{1}{\omega_{1bd}} e^{-\xi_{1b}\omega_{1b}t_*}\big[-\xi_{1b}\omega_{1b}\sin(\omega_{1bd}t_*) + \omega_{1bd}\cos(\omega_{1bd}t_*)\big]\dot{\zeta}_1(0)\Bigg],
\end{aligned} \tag{4.23}$$

Or expand the integral,

$$\begin{aligned}
\dot{w}_b(L_b, t_*^-) = \Psi_1(L_b)\Bigg\{ & I_{1b}\Omega_b^2 B_0 \frac{\Omega e^{-\xi_{1b}\omega_{1b}t_*}((\Omega^2-\omega_{1b}^2)\cos(\omega_{1bd}t_*)}{\Omega^4 + 4\xi_{1b}^2\Omega^2\omega_{1b}^2 - 2\Omega^2\omega_{1b}^2 + \omega_{1b}^4} \\
& - \frac{\frac{\Omega}{\omega_{1bd}} e^{-\xi_{1b}\omega_{1b}t_*}(\Omega^2-\omega_{1b}^2)\omega_{1b}\xi_{1b}\sin(\omega_{1bd}t_*)}{\Omega^4 + 4\xi_{1b}^2\Omega^2\omega_{1b}^2 - 2\Omega^2\omega_{1b}^2 + \omega_{1b}^4} - \frac{\omega_{1b}}{\sqrt{1-\xi_{1b}^2}} e^{-\xi_1\omega_{1b}t_*}\sin(\omega_{1bd}t_*)\zeta_1(0) \\
& + \frac{1}{\omega_{1bd}} e^{-\xi_{1b}\omega_{1b}t_*}\big[-\xi_{1b}\omega_{1b}\sin(\omega_{1bd}t_*) + \omega_{1bd}\cos(\omega_{1bd}t_*)\big]\dot{\zeta}_1(0)\Bigg\},
\end{aligned} \tag{4.24}$$

Similarly,

$$\dot{w}_b(L_b,t_*^+)=\Psi_1(L_b)\Bigg[\frac{-\xi_{1b}\omega_{1b}}{\omega_{1d}}I_{1b}\Omega_b^2B_0\int_0^{t_*}\sin(\Omega_b\tau)e^{-\xi_{1b}\omega_{1b}(t_*-\tau)}\sin\omega_{1bd}(t_*-\tau)d\tau$$
$$+I_{1b}\Omega_b^2B_0\int_0^{t_*}\sin(\Omega_b\tau)e^{-\xi_{1b}\omega_{1b}(t_*-\tau)}\cos\omega_{1bd}(t_*-\tau)d\tau-\frac{\omega_{1b}}{\sqrt{1-\xi_{1b}^2}}e^{-\xi_1\omega_{1b}t_*}\sin(\omega_{1bd}t_*)\zeta_1(0)$$
$$-\Psi_1(L_b)F_0-\frac{1}{\omega_{1bd}}e^{-\xi_1\omega_{1b}t_*}\big[-\xi_{1b}\omega_{1b}\sin(\omega_{1bd}t_*)+\omega_{1bd}\cos(\omega_{1bd}t_*)\big]\dot{\zeta}_1(0)\Bigg], \tag{4.25}$$

Or expand the integral,

$$\dot{w}_b(L_b,t_*^+)=\Psi_1(L_b)\Bigg\{I_{1b}\Omega_b^2B_0\frac{\Omega e^{-\xi_{1b}\omega_{1b}t_*}((\Omega^2-\omega_{1b}^2)\cos(\omega_{1bd}t_*)}{\Omega^4+4\xi_{1b}^2\Omega^2\omega_{1b}^2-2\Omega^2\omega_{1b}^2+\omega_{1b}^4}$$
$$-\frac{\frac{\Omega}{\omega_{1bd}}e^{-\xi_{1b}\omega_{1b}t_*}(\Omega^2-\omega_{1b}^2)\omega_{1b}\xi_{1b}\sin(\omega_{1bd}t_*)}{\Omega^4+4\xi_{1b}^2\Omega^2\omega_{1b}^2-2\Omega^2\omega_{1b}^2+\omega_{1b}^4}-\frac{\omega_{1b}}{\sqrt{1-\xi_{1b}^2}}e^{-\xi_1\omega_{1b}t_*}\sin(\omega_{1bd}t_*)\zeta_1(0) \tag{4.26}$$
$$-\Psi_1(L_b)F_0+\frac{1}{\omega_{1bd}}e^{-\xi_{1b}\omega_{1b}t_*}\big[-\xi_{1b}\omega_{1b}\sin(\omega_{1bd}t_*)+\omega_{1bd}\cos(\omega_{1bd}t_*)\big]\dot{\zeta}_1(0)\Bigg\},$$

Substitute equation (14) and (15) into equation (11), the amplitude of the impulse due to impact is solved,

$$F_0=\frac{\dot{w}_b(L_b,t_k^-)-\dot{w}_b(L_b,t_k^+)}{\Psi_1^2(L_b)}=\frac{\dot{w}(L,t_k^+)-\dot{w}(L,t_k^-)}{\Psi_1^2(L)}, \tag{4.27}$$

Combine equation 4.22 and 4.25 and make further simplify, the magnitude of the impulse is determined by the following equation,

$$
\begin{aligned}
F_0 &= \frac{(1+e)(\dot{w}_b(L_b,t_k^-)-\dot{w}(L,t_k^-))}{\Phi_1^2(L)+\Psi_1^2(L_b)} = \\
&\frac{1+e}{\Phi_1^2(L)+\Psi_1^2(L_b)}\Bigg\{\Psi_1(L_b)\Bigg\{I_{1b}\Omega_b^2 B_0\Bigg[\frac{\frac{\Omega}{\omega_{1bd}}e^{-\xi_{1b}\omega_{1b}t_*}((\Omega^2-\omega_{1b}^2)\omega_{1bd}\cos(\omega_{1bd}t_*)}{\Omega^4+4\xi_{1b}^2\Omega^2\omega_{1b}^2-2\Omega^2\omega_{1b}^2+\omega_{1b}^4} \\
&\frac{-(\Omega^2+\omega_{1b}^2)\xi_{1b}\omega_{1b}\sin(\omega_{1bd}t_*))+\Omega(\omega_{1b}^2-\Omega^2)\cos(\Omega t_*)+2\xi_{1b}\omega_{1b}\Omega^2\sin(\Omega t_*)}{\Omega^4+4\xi_{1b}^2\Omega^2\omega_{1b}^2-2\Omega^2\omega_{1b}^2+\omega_{1b}^4} \\
&-\frac{\omega_{1b}}{\sqrt{1-\xi_{1b}^2}}e^{-\xi_1\omega_{1b}t_*}\sin(\omega_{1bd}t_*)\zeta_1(0) \\
&+\frac{e^{-\xi_1\omega_{1b}t_*}}{\omega_{1bd}}\big[-\xi_{1b}\omega_{1b}\sin(\omega_{1bd}t_*)+\omega_{1bd}\cos(\omega_{1bd}t_*)\big]\dot{\zeta}_1(0)\Bigg\} \\
&-\Phi_1(L)\Bigg\{I_1\Omega^2A_0\Bigg[\frac{\frac{\Omega}{\omega_{1d}}e^{-\xi_1\omega_1t_*}((\Omega^2-\omega_1^2)\omega_{1d}\cos(\omega_{1d}t_*)}{\Omega^4+4\xi_1^2\Omega^2\omega_1^2-2\Omega^2\omega_1^2+\omega_1^4} \\
&\frac{-(\Omega^2+\omega_1^2)\xi_1\omega_1\sin(\omega_{1d}t_*))+\Omega(\omega_1^2-\Omega^2)\cos(\Omega t_*)+2\xi_1\omega_1\Omega^2\sin(\Omega t_*)}{\Omega^4+4\xi_1^2\Omega^2\omega_1^2-2\Omega^2\omega_1^2+\omega_1^4} \\
&-\frac{\omega_1}{\sqrt{1-\xi_1^2}}e^{-\xi_1\omega_1t_*}\sin(\omega_{1d}t_*)\eta_1(0) \\
&+\frac{e^{-\xi_1\omega_1t_*}}{\omega_{1d}}\big[-\xi_1\omega_1\sin(\omega_{1d}t_*)+\omega_{1d}\cos(\omega_{1d}t_*)\big]\dot{\eta}_1(0)\Bigg\},
\end{aligned}
\tag{4.28}
$$

4.2 PERIODIC PLUCKING

The motion is called plucking if the beams are allowed to pass each other when they hit each other. This motion is possible because of the flexibility of the driving beam and relatively larger gap between the beams.

The main drawback of the periodic bouncing is its frequency bandwidth, where based on the design parameters there is no possible periodic motion below a certain frequency. Since we are looking for a possible periodic motion in lowest frequency to generate the maximum power and voltage, the proposed motion is possible in lower frequency spectrum.

4.2.1 Modeling of Two Beams Impact via Mapping Function

Considering the state vector variables $z = (w, w_b)^T$, the impact variables of k^{th} impact w_{b_k} and $\dot{w}_k$ and t_k are defined as the impact position, after impact velocity and impact time of the driving beam, respectively. Similarly, the impact variables of the piezoelectric driven beam t_k, w_k and $\dot{w}_k$ are defined as the impact time, position and after impact velocity, respectively. For the time interval $t \in [t_{k-1} - t_{k+1}], (k = 1, 2, ...)$, the implicit map P_k is written as:

$$P_k : (w_{k-1}, w_{b_{k-1}}) \rightarrow (w_{k+1}, w_{b_{k+1}}) \Rightarrow$$

$$(w_{k+1}, w_{b_{k+1}}, \dot{w}_{k+1}, \dot{w}_{b_{k+1}}) = P_k(w_{k-1}, w_{b_{k-1}}, \dot{w}_{k-1}, \dot{w}_{b_{k-1}}). \tag{4.29a}$$

The corresponding mechanical implicit relations of displacements and velocities of the implicit map are:

$$f_k^b(t_k, t_{k-1}, w_{b_{k-1}}, \dot{w}_{b_{k-1}}^+, \dot{w}_{k-1}^+) = w_{b_k} =$$

$$\Psi_1(L_b)\Bigg[\frac{1}{\omega_{1bd}} I_{1b}\Omega_b^2 B_0 \int_{t_{k-1}}^{t_k} \sin(\Omega\tau) e^{-\xi_{1b}\omega_{1b}(t_k-\tau)} \sin\omega_{1bd}(t_k-\tau)d\tau$$

$$+ e^{-\xi_{1b}\omega_{1b}(t_k-t_{k-1})}\Bigg(\cos(\omega_{1bd}(t_k-t_{k-1})) + \frac{\xi_{1b}}{\sqrt{1-\xi_{1b}^2}}\sin(\omega_{1bd}(t_k-t_{k-1}))\Bigg)\zeta_1(t_{k-1})$$

$$+ \frac{1}{\omega_{1bd}} e^{-\xi_{1b}\omega_{1b}(t_k-t_{k-1})}\sin(\omega_{1bd}(t_k-t_{k-1}))\dot{\zeta}_1(t_{k-1}^+)\Bigg], \tag{4.30a}$$

$$\dot{f}_k^b(t_k, t_{k-1}, w_{b_{k-1}}, \dot{w}_{b_{k-1}}^+, \dot{w}_{k-1}^+) = \dot{w}_{bk}^+ =$$

$$\Psi_1(L_b)\Bigg[\frac{-\xi_{1b}\omega_{1b}}{\omega_{1d}} I_{1b}\Omega_b^2 B_0 \int_{t_{k-1}}^{t_k} \sin(\Omega_b\tau) e^{-\xi_{1b}\omega_{1b}(t_k-\tau)} \sin\omega_{1bd}(t_k-\tau)d\tau$$

$$+ I_{1b}\Omega_b^2 B_0 \int_{t_{k-1}}^{t_k} \sin(\Omega_b\tau) e^{-\xi_{1b}\omega_{1b}(t_k-\tau)} \cos\omega_{1bd}(t_k-\tau)d\tau$$

$$- \frac{\omega_{1b}}{\sqrt{1-\xi_{1b}^2}} e^{-\xi_1\omega_{1b}(t_k-t_{k-1})}\sin(\omega_{1bd}(t_k-t_{k-1}))\zeta_1(t_{k-1})$$

$$- \Psi_1(L_b)F_0 - \frac{1}{\omega_{1bd}} e^{-\xi_1\omega_{1b}(t_k-t_{k-1})}\big[-\xi_{1b}\omega_{1b}\sin(\omega_{1bd}(t_k-t_{k-1}))$$

$$+ \omega_{1bd}\cos(\omega_{1bd}(t_k-t_{k-1}))\big]\dot{\zeta}_1(t_{k-1}^+)\Bigg], \tag{4.30b}$$

$$
\begin{aligned}
&f_k(t_k, t_{k-1}, w_{b_{k-1}}, \dot{w}^+_{b_{k-1}}, \dot{w}^+_{k-1}) = w_k = \\
&\Phi_1(L_b)\Bigg[\frac{1}{\omega_{1d}} I_1 \Omega^2 A_0 \int_{t_{k-1}}^{t_k} \sin(\Omega\tau) e^{-\xi_1\omega_1(t_k-\tau)} \sin\omega_{1d}(t_k-\tau)d\tau \\
&+ e^{-\xi_1\omega_1(t_k-t_{k-1})}\Bigg(\cos(\omega_{1d}(t_k-t_{k-1})) + \frac{\xi_1}{\sqrt{1-\xi_1^2}}\sin(\omega_{1d}(t_k-t_{k-1}))\Bigg)\eta_1(t_{k-1}) \\
&+ \frac{1}{\omega_{1d}} e^{-\xi_1\omega_1(t_k-t_{k-1})}\sin(\omega_{1d}(t_k-t_{k-1}))\dot{\eta}_1(t^+_{k-1})\Bigg],
\end{aligned}
\tag{4.31a}
$$

$$
\begin{aligned}
&\dot{f}_k(t_k, t_{k-1}, w_{b_{k-1}}, \dot{w}^+_{b_{k-1}}, \dot{w}^+_{k-1}) = \dot{w}^+_k = \\
&\Phi_1(L)\Bigg[-\frac{\omega_1}{\sqrt{1-\xi_1^2}} e^{-\xi_1\omega_1(t_k-t_{k-1})}\sin(\omega_{1d}(t_k-t_{k-1}))\eta_1(t_{k-1}) \\
&+ I_1\Omega^2 A_0 \int_{t_{k-1}}^{t_k} \sin(\Omega\tau) e^{-\xi_1\omega_1(t_k-\tau)}\cos\omega_{1d}(t_k-\tau)d\tau + \Phi_1(L)F_0 \\
&\frac{-\xi_1\omega_1}{\omega_{1d}} I_1\Omega^2 A_0 \int_{t_{k-1}}^{t_k} \sin(\Omega\tau) e^{-\xi_1\omega_1(t_k-\tau)}\sin\omega_{1d}(t_k-\tau)d\tau \\
&+ \frac{1}{\omega_{1d}} e^{-\xi_1\omega_1(t_k-t_{k-1})}\big[-\xi_1\omega_1\sin(\omega_{1d}(t_k-t_{k-1})) + \omega_{1d}\cos(\omega_{1d}(t_k-t_{k-1}))\big]\dot{\eta}_1(t^+_{k-1})\Bigg],
\end{aligned}
\tag{4.31b}
$$

According to Equ.(4.31) and Equ.(4.29), the discrete impact mapping functions can be defined as:

$$F_k^1(t_k, w_{b_k}, t_{k-1}, w_{b_{k-1}}, \dot{w}_{b_{k-1}}^+, \dot{w}_{k-1}^+) = f_{k+1}^b - w_{b_{k-1}} = 0, \tag{4.32a}$$

$$F_k^2(t_k, w_{b_k}, \dot{w}_{b_k}^+, \dot{w}_k^+, t_{k-1}, w_{b_{k-1}}, \dot{w}_{b_{k-1}}^+, \dot{w}_{k-1}^+) = \dot{f}_{k+1}^b - \dot{w}_{b_{k-1}}^+ = 0, \tag{4.32b}$$

$$F_k^3(t_k, w_{b_k}, t_{k-1}, w_{b_{k-1}}, \dot{w}_{b_{k-1}}^+, \dot{w}_{k-1}^+) = f_{k+1} - w_{k-1} = 0 \tag{4.32c}$$

$$F_k^4(t_k, w_{b_k}, \dot{w}_{b_k}^+, \dot{w}_k^+, t_{k-1}, w_{b_{k-1}}, \dot{w}_{b_{k-1}}^+, \dot{w}_{k-1}^+) = \dot{f}_{k+1} - \dot{w}_{k-1}^+ = 0, \tag{4.32d}$$

$$F_{k+1}^1(t_{k+1}, z_{b_{k+1}}, t_k, w_{b_k}, \dot{w}_{b_k}^+, \dot{w}_k^+) = f_{k+2}^b - w_{b_k} = 0, \tag{4.32e}$$

$$F_{k+1}^2(t_{k+1}, w_{b_{k+1}}, \dot{w}_{b_{k+1}}^+, \dot{w}_{k+1}^+, t_k, w_{b_k}, \dot{w}_{b_k}^+, \dot{w}_k^+) = \dot{f}_{k+2}^b - \dot{w}_{b_k}^+ = 0, \tag{4.32f}$$

$$F_{k+1}^3(t_{k+1}, w_{b_{k+1}}, t_k, w_{b_k}, \dot{w}_{b_k}^+, \dot{w}_k^+) = f_{k+2} - w_k = 0 \tag{4.32g}$$

$$F_{k+1}^4(t_{k+1}, w_{b_{k+1}}, \dot{w}_{b_{k+1}}^+, \dot{w}_{k+1}^+, t_k, w_{b_k}, \dot{w}_{b_k}^+, \dot{w}_k^+) = \dot{f}_{k+2} - \dot{w}_k^+ = 0, \tag{4.32h}$$

$$w_{b_k} = w_k, \tag{4.32i}$$

$$w_{b_{k+1}} = w_{k+1}, \tag{4.32j}$$

$$w_{b_{k-1}} = w_{k-1}. \tag{4.32k}$$

Let $\mathbf{X_k} = [t_k, w_k, \dot{w}_k, \dot{w}_{b_k}]^T$ and $\mathbf{P_k} = [F_k^1, F_k^2, F_k^3, F_k^4]^T$ Once the switching points for a specific periodic motion is obtained, the local stability and bifurcation analysis can be achieved through the corresponding stability Jacobian matrix:

$$\mathbf{S} = \left[\frac{\partial \mathbf{P}_{k+1}}{\partial \mathbf{X}_{k+1}}\right]^{-1} \left[\frac{\partial \mathbf{P}_{k+1}}{\partial \mathbf{X}_k}\right] \left[\frac{\partial \mathbf{P}_k}{\partial \mathbf{X}_k}\right]^{-1} \left[\frac{\partial \mathbf{P}_k}{\partial \mathbf{X}_{k-1}}\right], \tag{4.33}$$

Where n is the number of periodic motion. Considering the eigenvalues of $\mathbf{S}$, the following statements hold:

If all $|\lambda_i| < 1$ for $(i = 1, 2, 3, 4)$, the periodic motion is stable.

If $|\lambda_i| > 1$ for $(i \in \{1, 2, 3, 4\})$, the periodic motion is unstable.

If $\lambda_i = -1$ and $|\lambda_j| < 1$ for $(i, j \in \{1, 2, 3, 4\}$ and $i \neq j)$, the period-doubling bifurcation of periodic motion occurs.

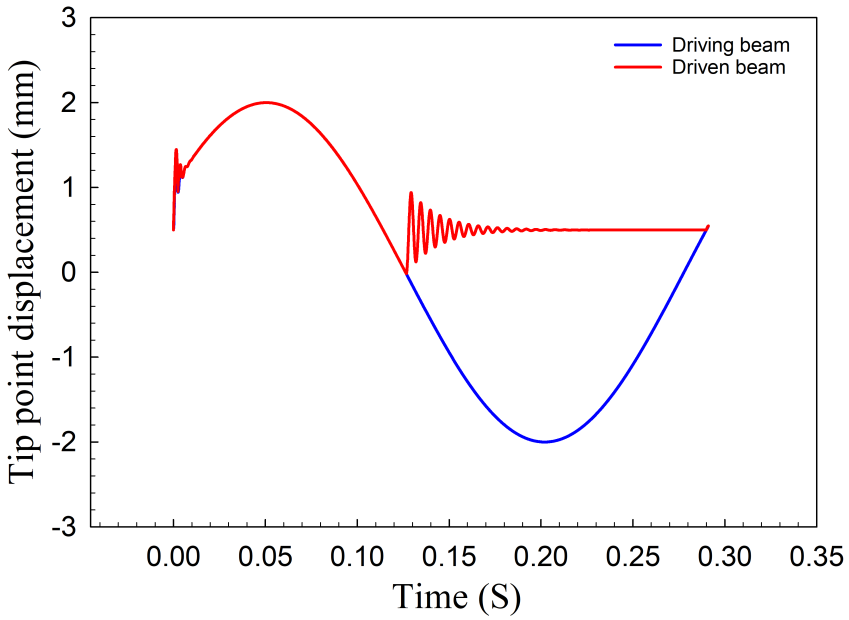

FIGURE A1: Displacement versus time for driving(blue) and driven(red) beams with arbitrary initial condition

If $\lambda_i = 1$ and $|\lambda_j| < 1$ for $(i, j \in \{1, 2, 3, 4\}$ and $i \neq j)$, the saddle-node bifurcation of the periodic motion occurs.

If $|\lambda_{i,j}| = 1$ is a pair of complex eigenvalues, the Neimark bifurcation of the periodic motion occurs.

In this section, the impact driven system is compared to a simple piezoelectric beam and the output power and voltage are predicted. Different types of motions of the proposed piezoelectric energy harvester system are studied and the best phase of the motion of the impact-driven system is chosen. The bifurcation diagrams of periodic solution of the impact-driven system are obtained. The numerical predictions of the output voltage and power of period-1 motion are also examined.

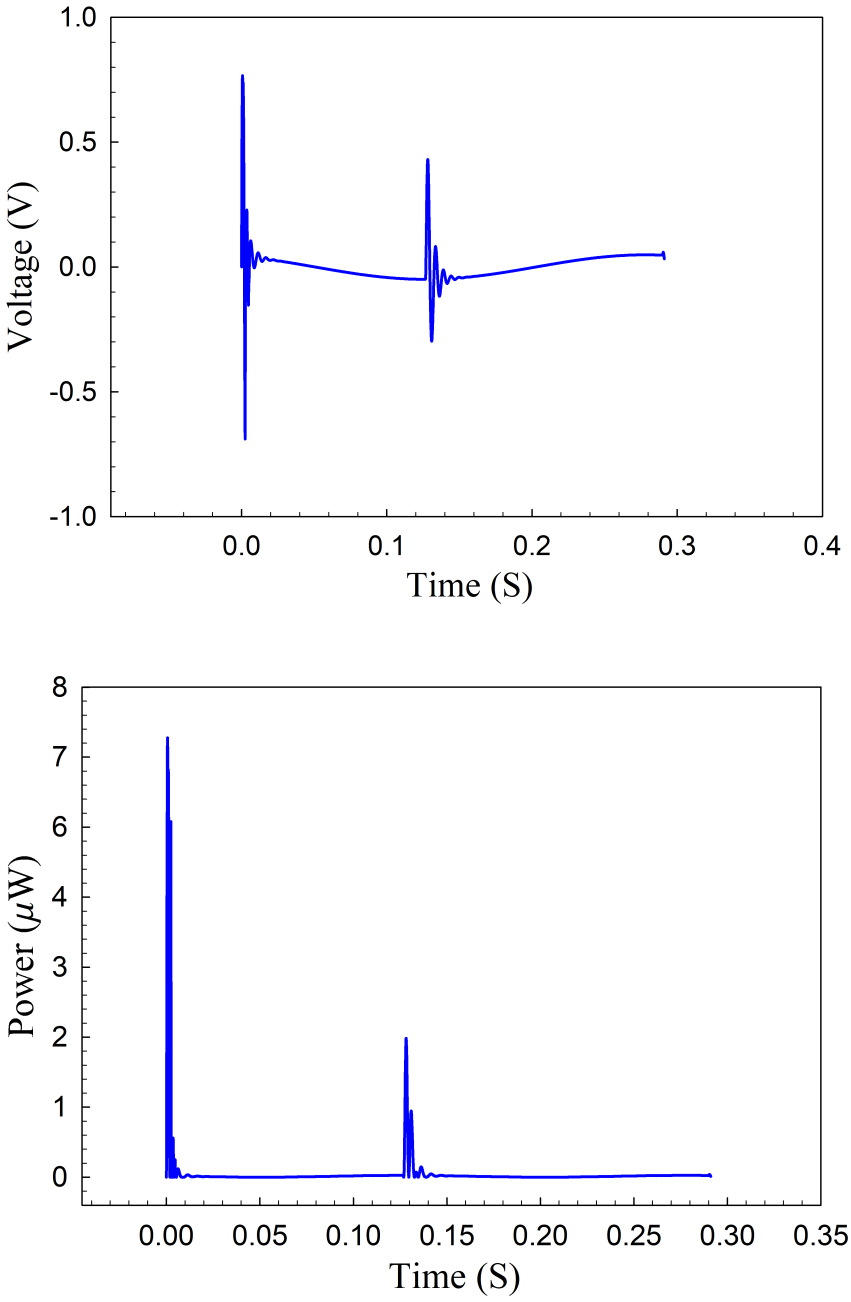

FIGURE A2: System with arbitrary initial condition and the different possible motions:chattering, stick and free vibration(a) Output voltage of the system, (b) Output power of the system,

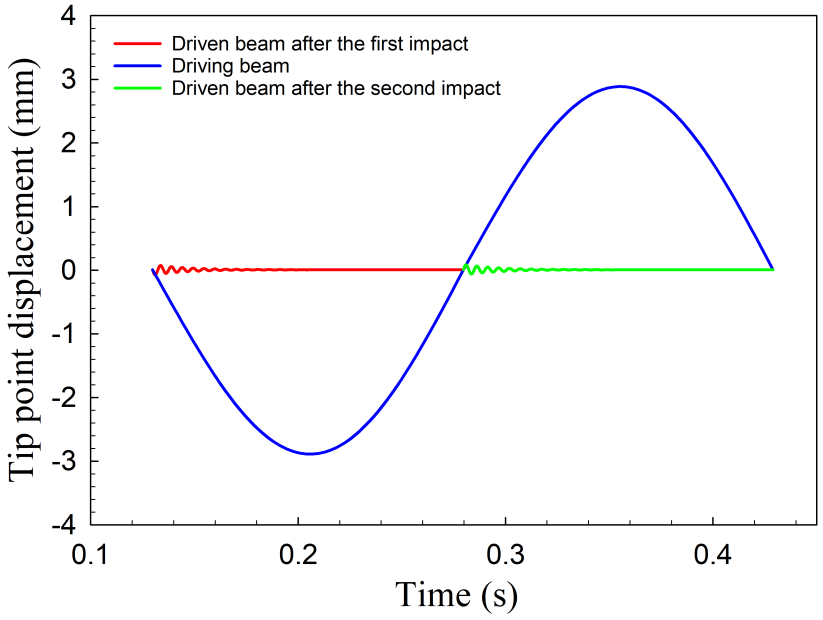

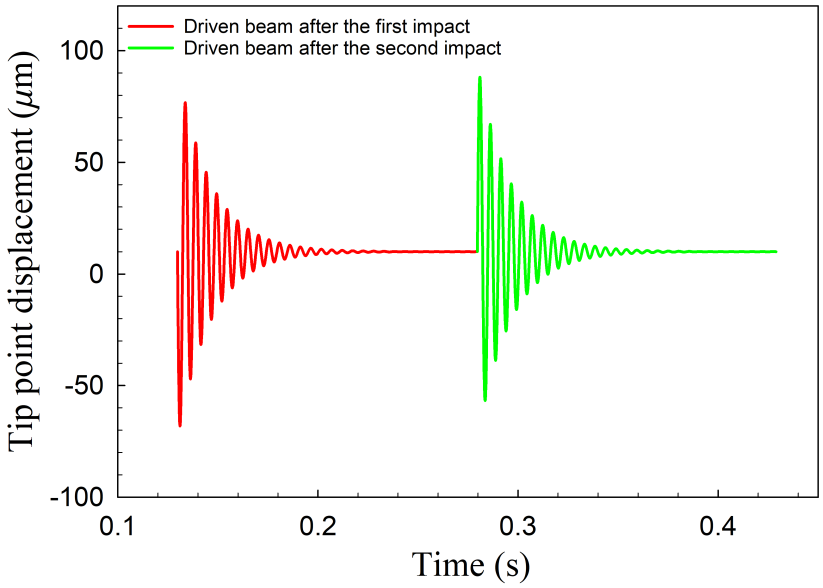

FIGURE A3: Impact driven system displacement at $\Omega \approx 3.3Hz$, (a) Displacement versus time for driving(blue) and driven(red) beams half period, (b) Displacement versus time for driven beam,

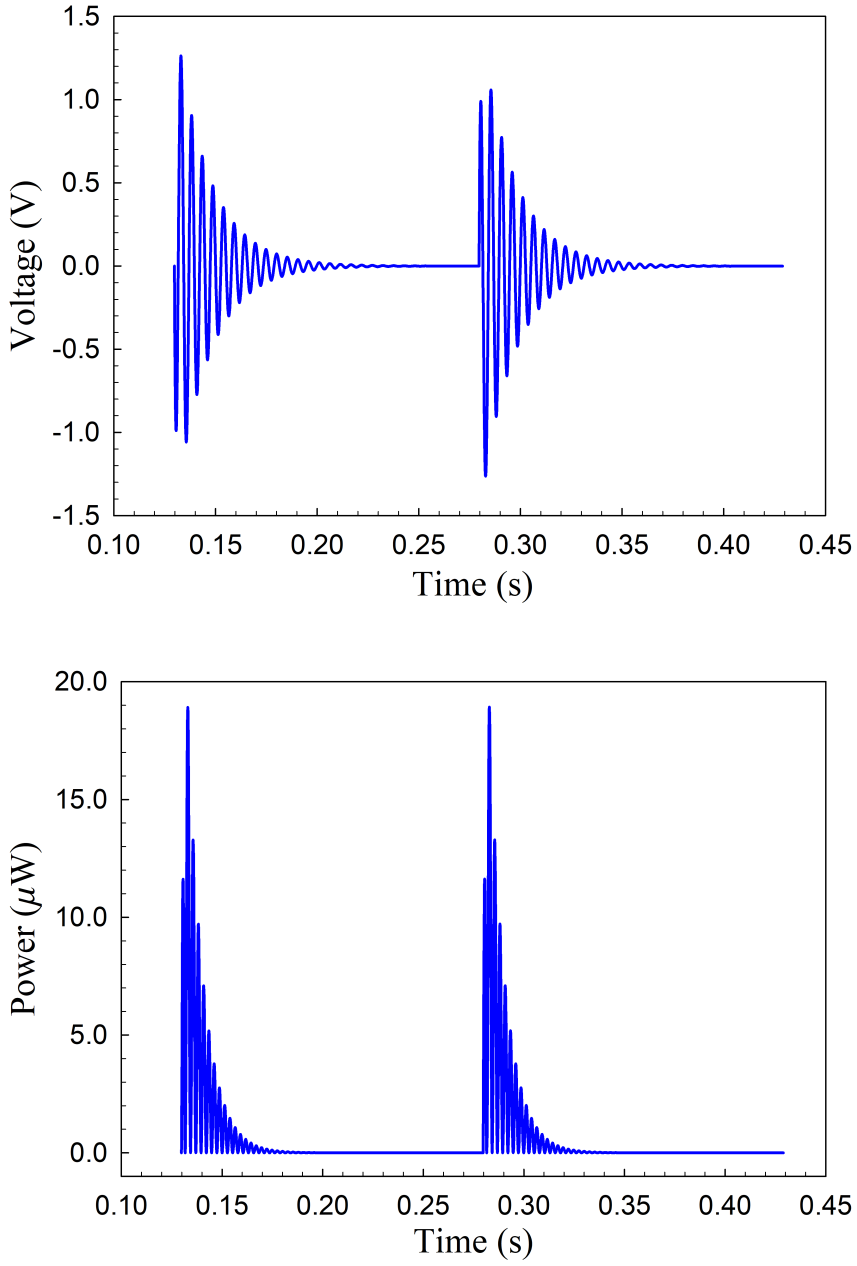

FIGURE A4: Output voltage an power at $\Omega \approx 3.3Hz$ for the proposed system, (a) Output voltage from impact driven system versus time, (b) Output power from impact driven system versus time,

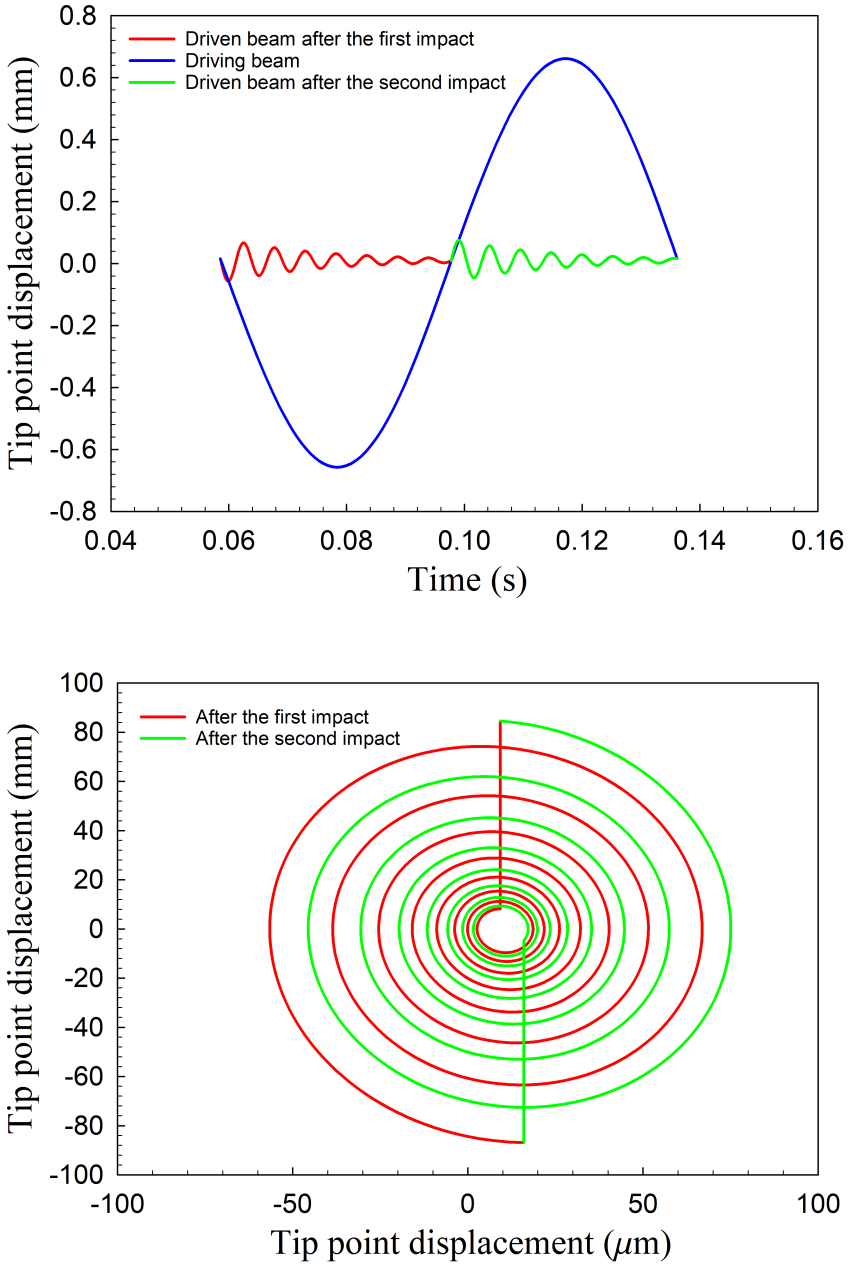

FIGURE A5: (a) Displacement versus time at $\Omega \approx 13Hz$, (b) Phase portrait of the driven beam at $\Omega \approx 13Hz$,

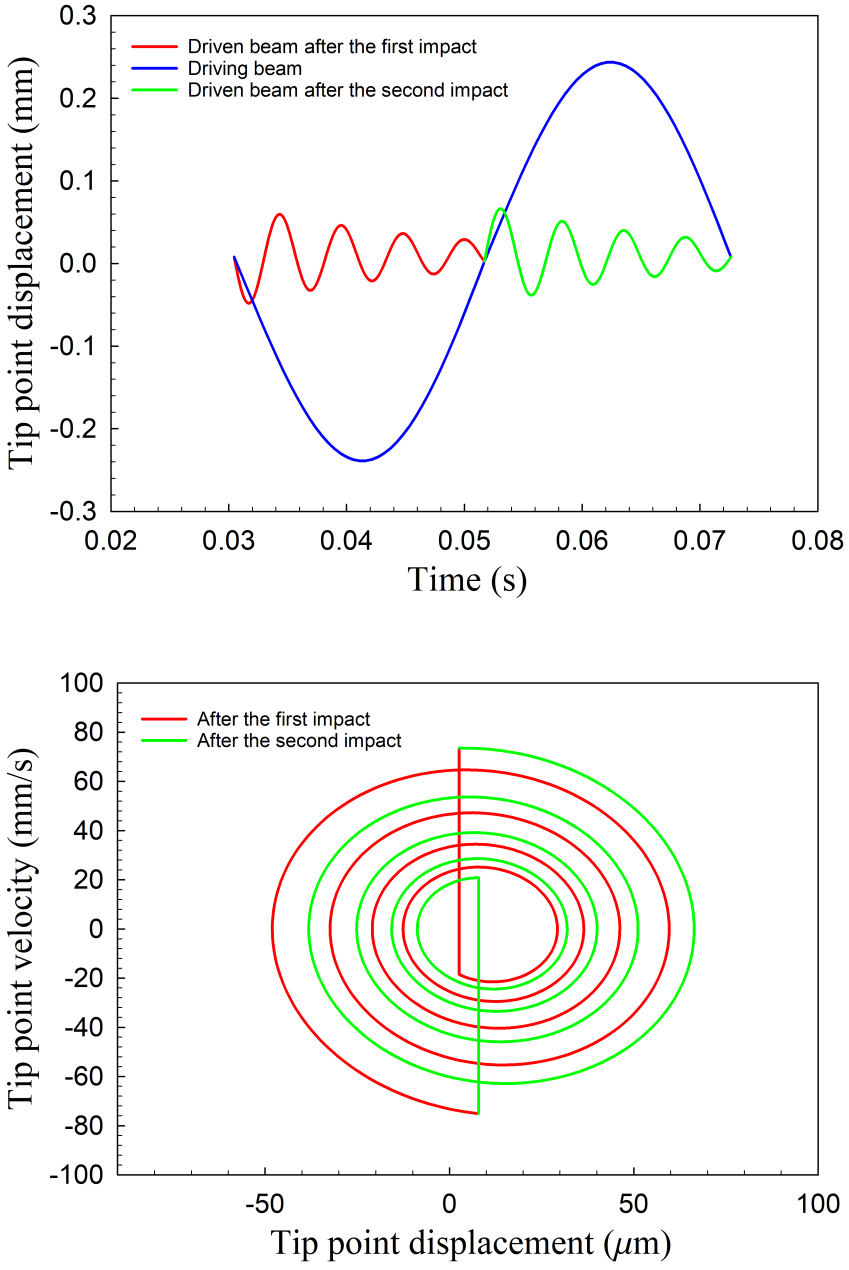

FIGURE A6: (a) Displacement versus time at $\Omega \approx 23Hz$, (b) Phase portrait of the driven beam at $\Omega \approx 23Hz$,

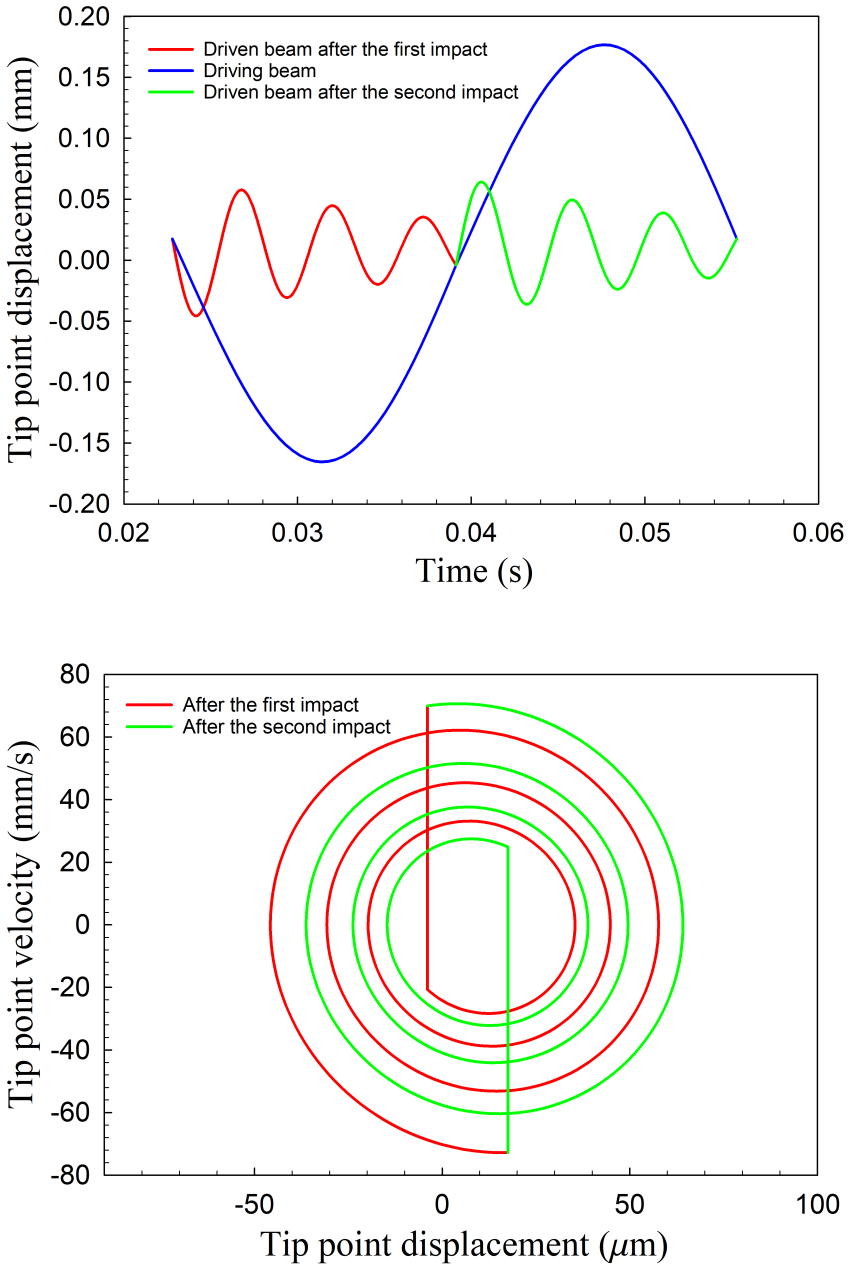

FIGURE A7: (a) Displacement versus time at $\Omega \approx 30Hz$, (b) Phase portrait of the driven beam at $\Omega \approx 30Hz$.

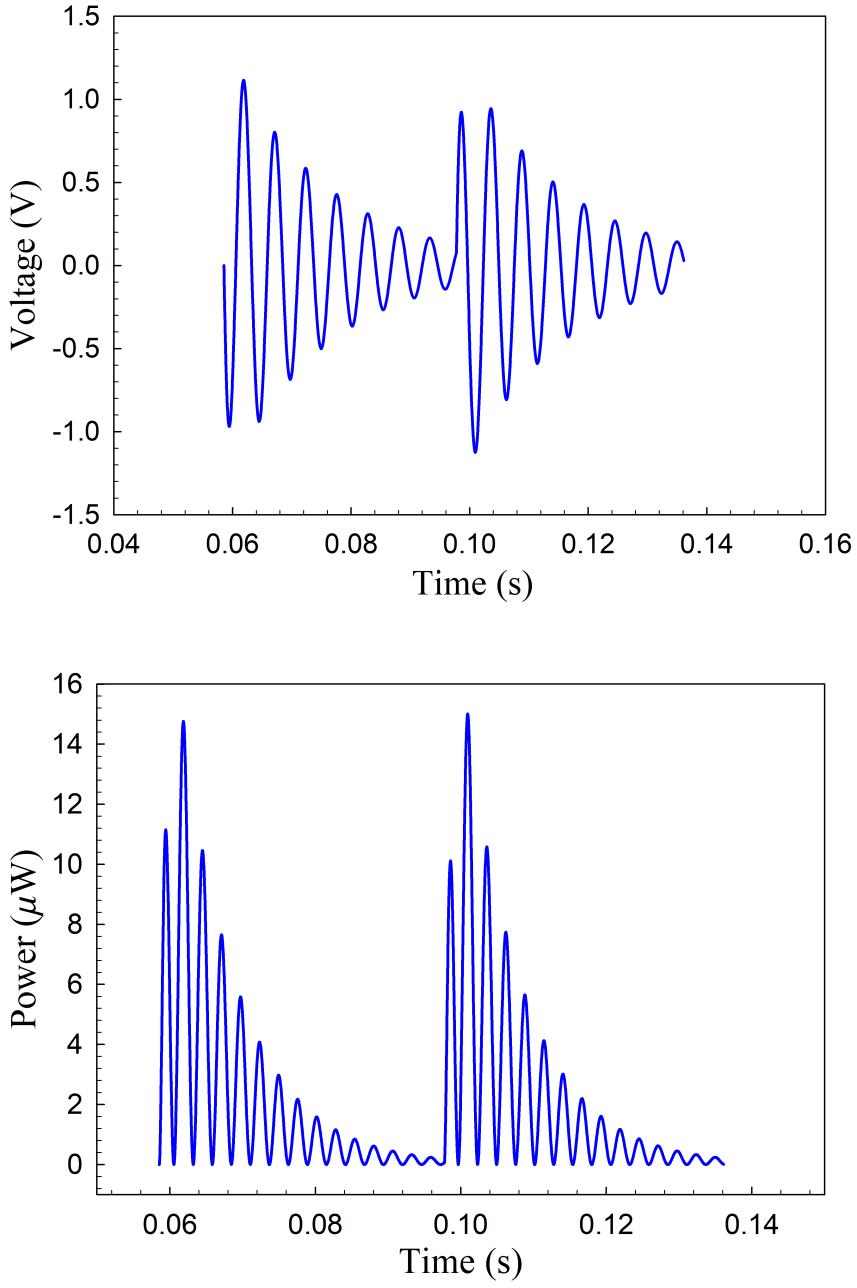

FIGURE A8: (a) Output voltage versus time at $\Omega \approx 13Hz$, (b) Output power versus time at $\Omega \approx 13Hz$,

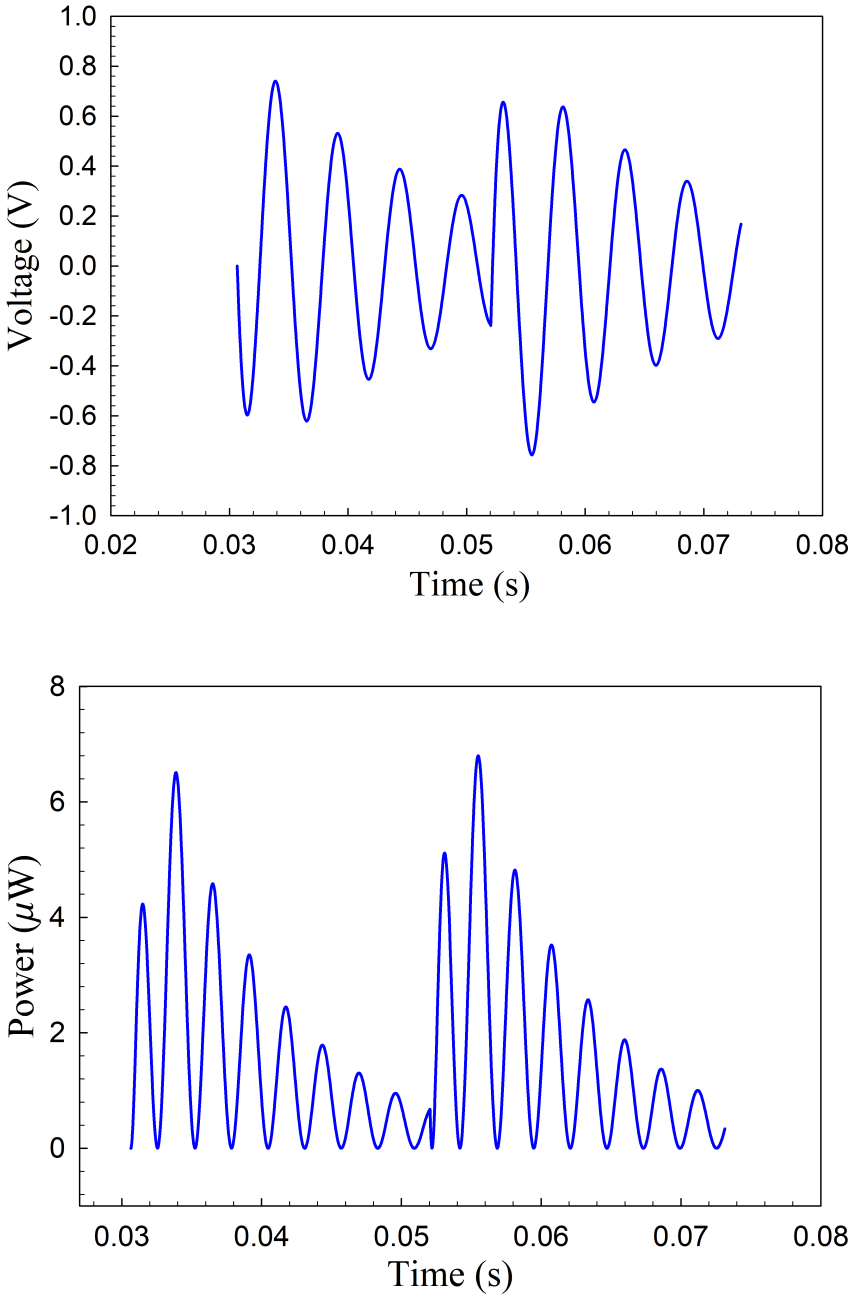

FIGURE A9: (a) Output voltage versus time at $\Omega \approx 23Hz$, (b) Output power versus Time at $\Omega \approx 23Hz$,

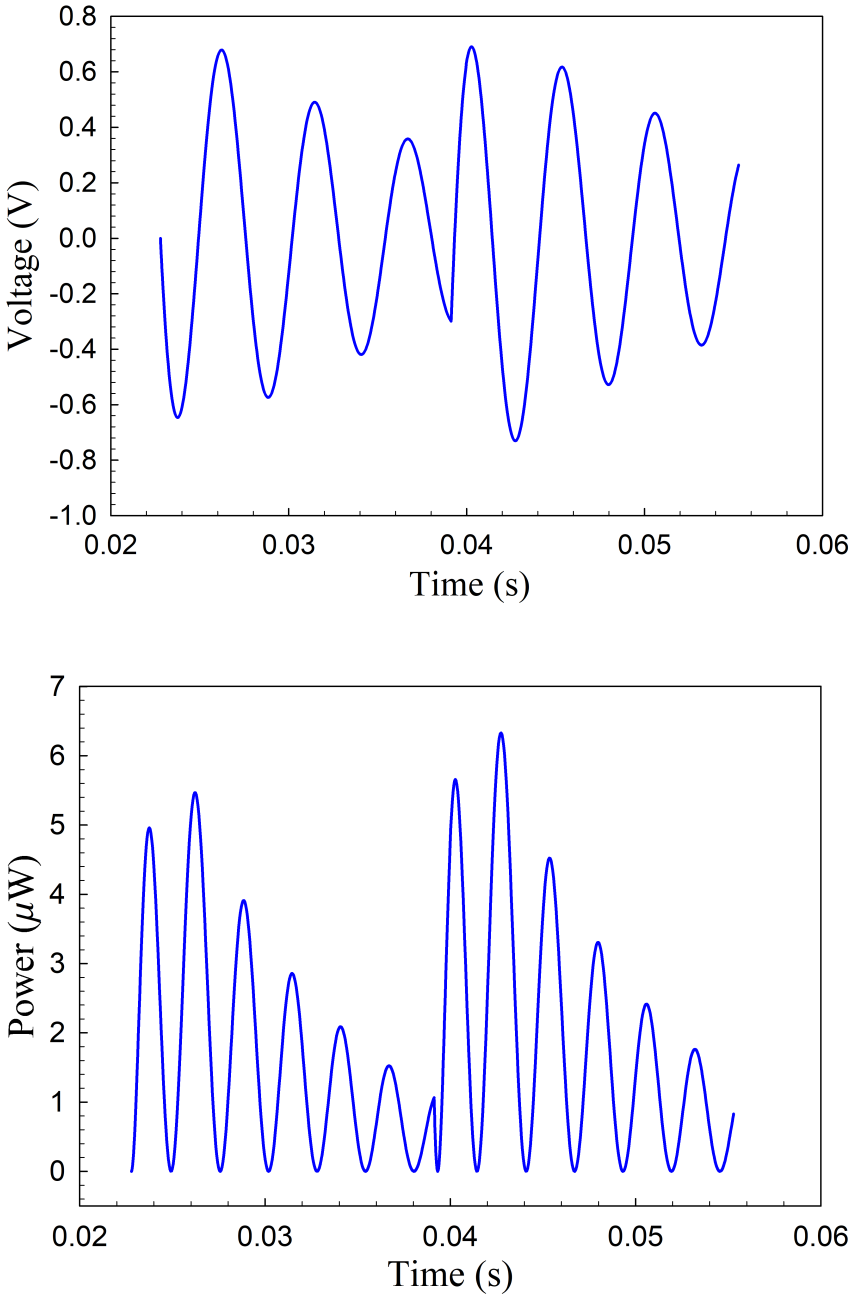

FIGURE A10: (a) Output voltage versus time at $\Omega \approx 30Hz$, (b) Output power versus time at $\Omega \approx 30Hz$.

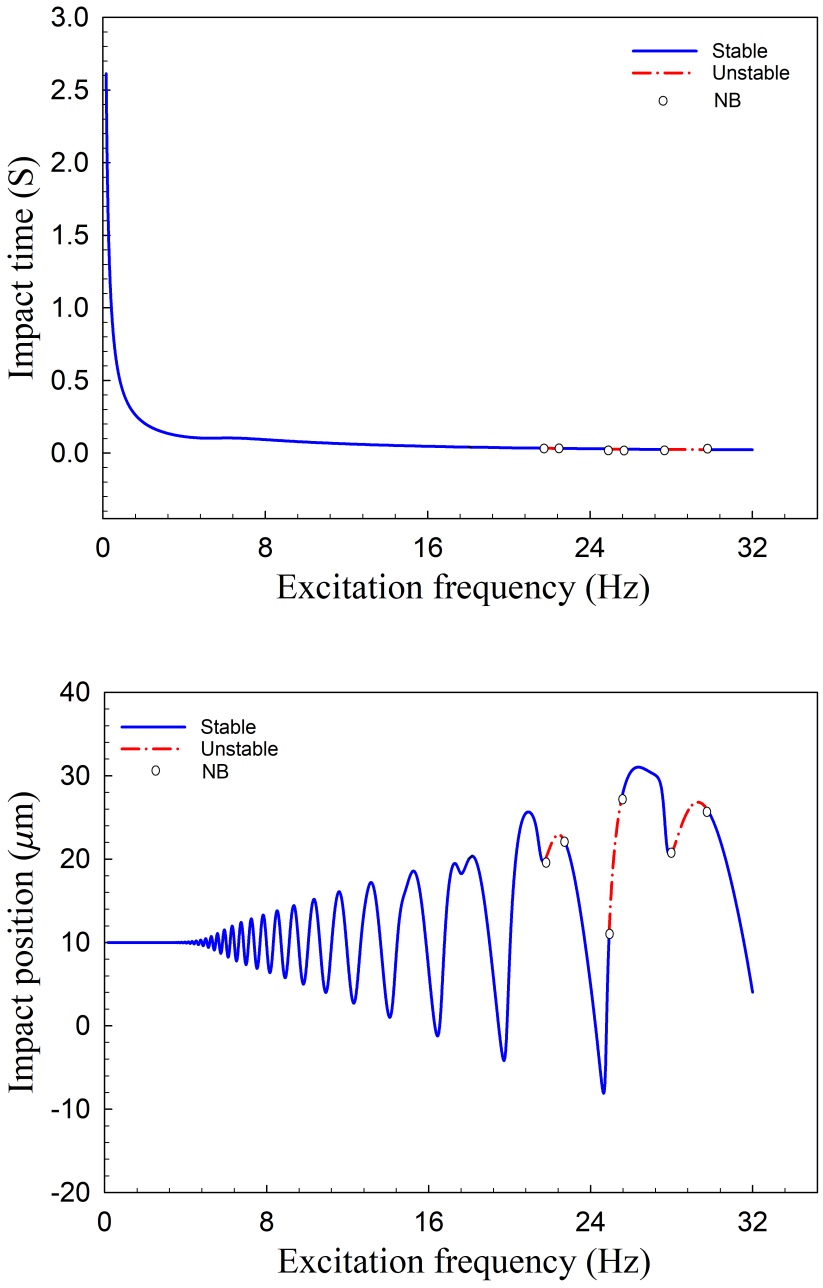

FIGURE A11: Period-1 motion bifurcation graphs of the first impact piezoelectric driven beam, (a) Impact time vs frequency, (b) Impact position vs frequency,

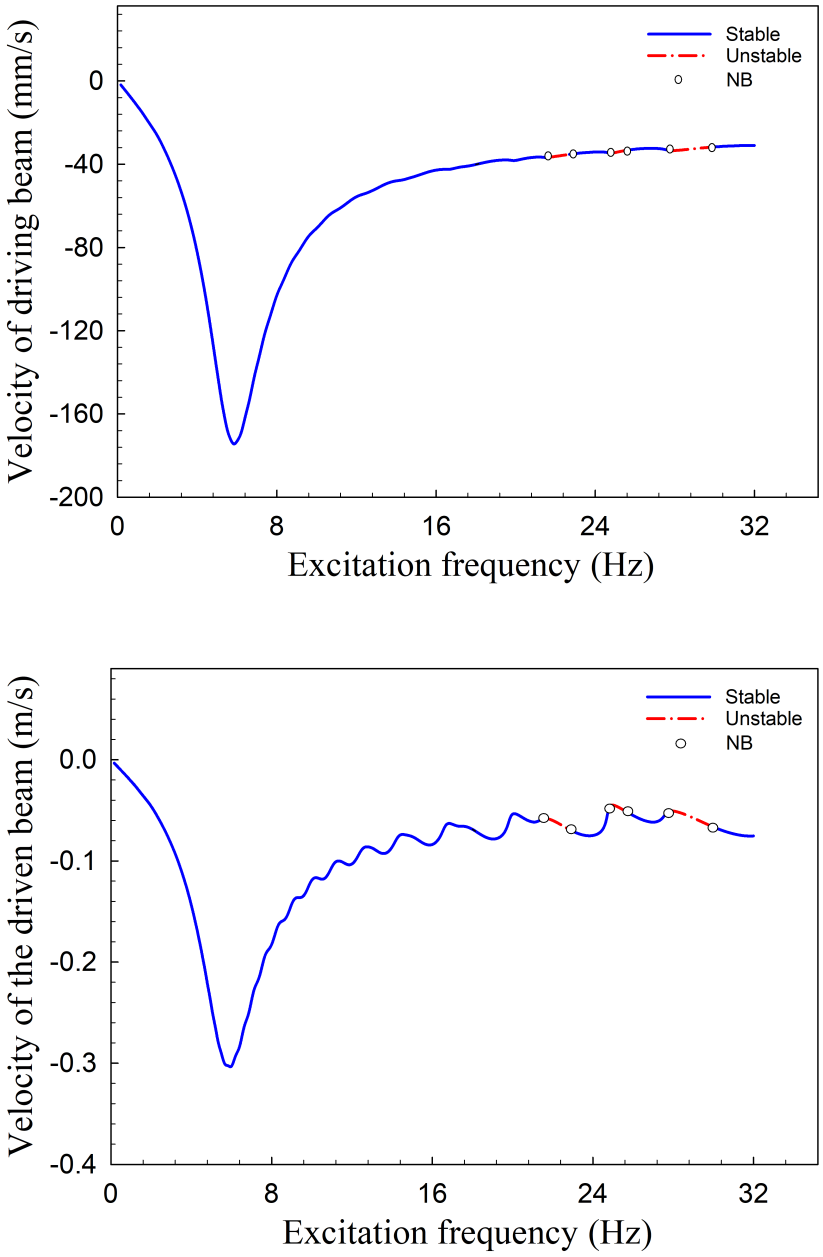

FIGURE A12: Period-1 motion bifurcation graphs of the first impact piezoelectric driven beam, (a) Impact velocity of the driving beam vs frequency, (b) Impact velocity of the driven beam vs frequency,

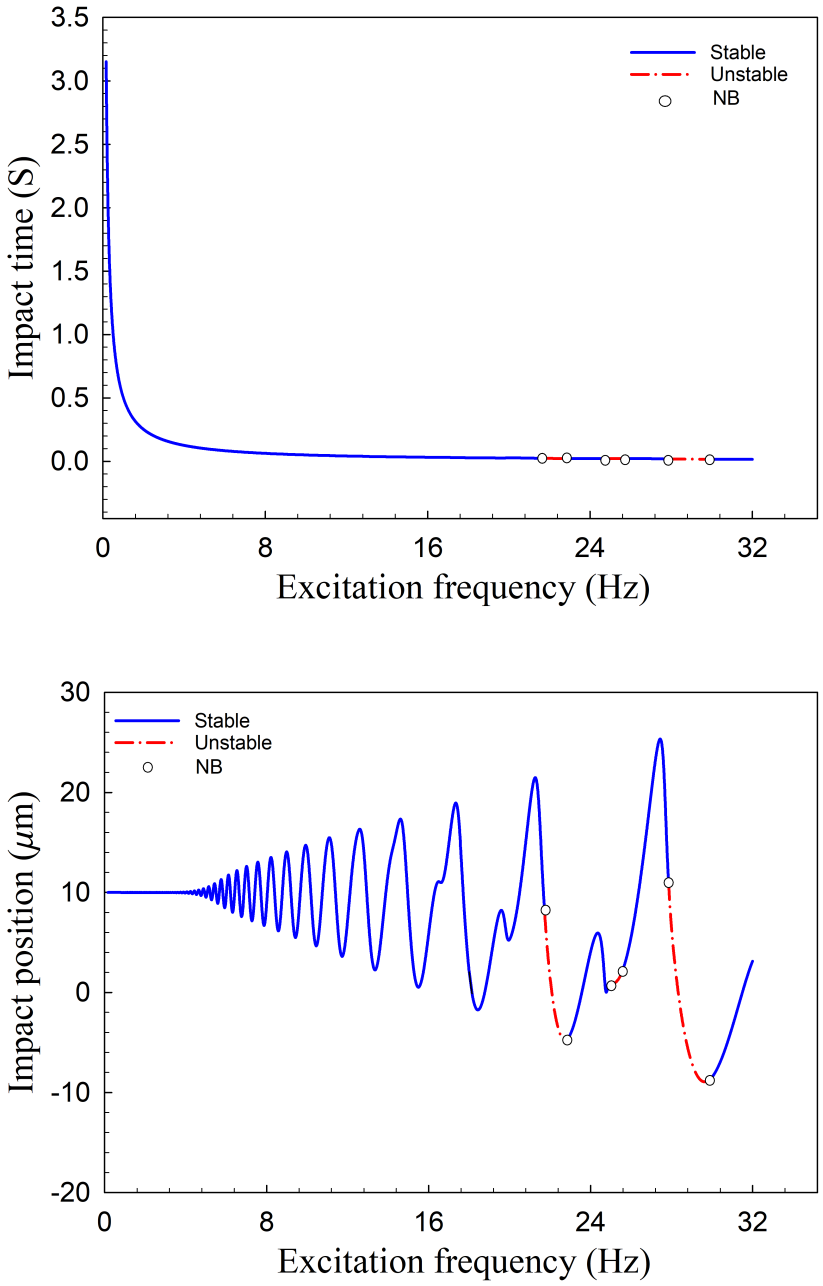

FIGURE A13: Period-1 motion bifurcation graphs of the second impact piezoelectric driven beam, (a) Impact time vs frequency, (b) Impact position vs frequency,

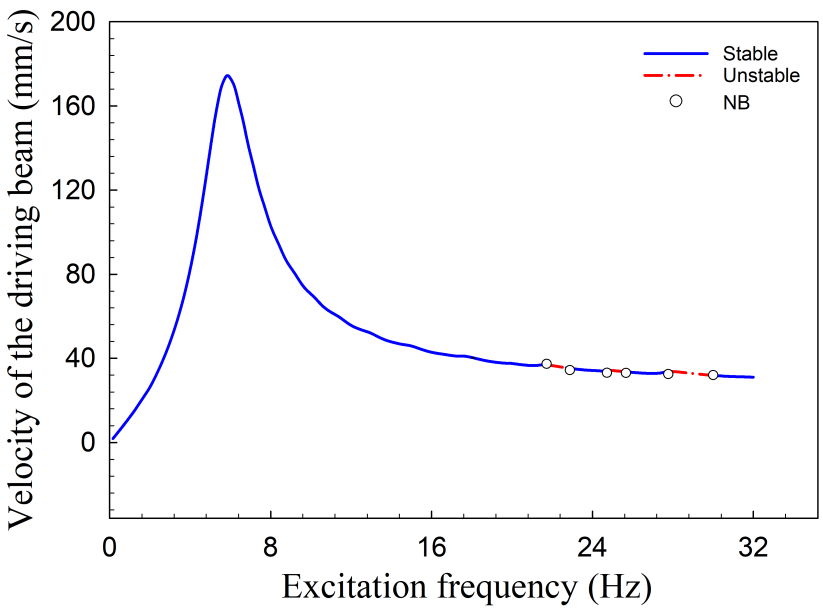

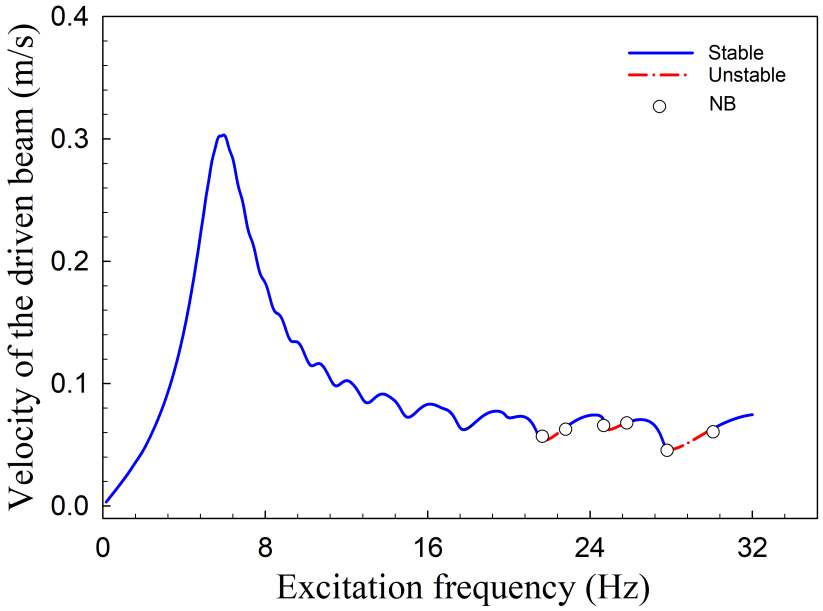

FIGURE A14: Period-1 motion bifurcation graphs of the second impact piezoelectric driven beam, (a) Impact velocity of the driving beam vs frequency, (b) Impact velocity of the driven beam vs frequency

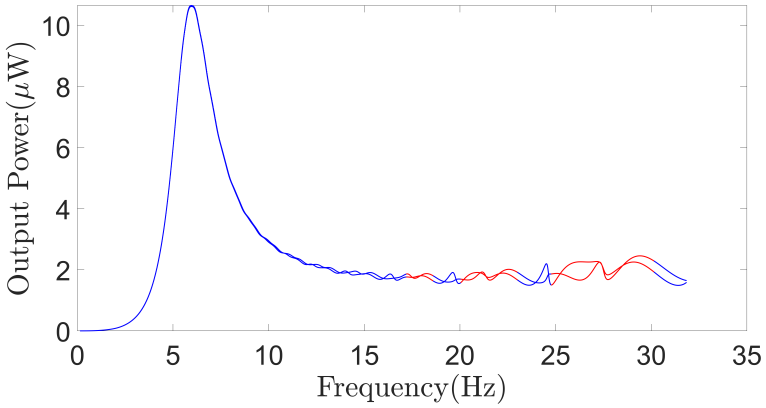

FIGURE A15: (a) Average output power vs frequency for the impact driven system with base excitation for $\Omega \in$(1,200) Rad/s

4.2.2 Impact Driven System

The goal of this research is to enhance the piezoelectric harvester's energy retrieving performance from ambient vibrations with low or varying frequencies. Therefore, the frequency region in our study is less than the natural frequency of the piezoelectric beam.

The output voltage and power of the piezoelectric beam excited by impact from the driving beam with arbitrary initial conditions at $\Omega \approx 3.3Hz$ are predicted as shown in figures A2(a) and A2(b) and, the displacement of the impact-driven system components are presented in figure A2(a). Comparing figures A2(a) and A2(b) and A1, one can see that the impact-driven piezoelectric harvester has great potential to provide much more energy when the excitation frequency is low.

The same four different types of motions which were defined in previous chapter are applicable in this chapter as well and are shown in figures A2 where they are obtained from Euler-Bernouli equations.

4.2.3 Periodic Motion

For an impact-driven system, periodic motions are the simplest ones. To deeply understand the impact-driven frequency up-converter system, periodic motions of the energy harvesting system are studied. Based on figure A2, in order to have optimum motion, the system has to avoid stick motion and contain more rapid-impact motion. Each cycle includes two impacts which is shown in figure A3(a) and a better graph for the driven piezoelectric beam is presented in A3(b). This motion will generate two discontinuous motion, voltage and power in each cycle of the the driving beam which are shown in A4(a) and (b).

In this study half cycle impact with plucking is selected and investigated. Figures A5(a), A6(a) and A7(a) show multiple period-1 motion, where the red and blue lines represent the tip point displacements of the driven and the driving beams in one cycle, respectively. Figures A5(b), A6(b) and A7(b) are the velocity versus displacement or the phase portrait of period-1 motion of the piezoelectric beam where the blue line represents the motion between the first impact and the second impact and the green line represents the motion between the second and third impact.

In this section, the bifurcation diagrams of periodic motions are presented via studying the analytic solutions of period-1 motion. Without losing generality, a set of system parameters are considered as :$Q = 0.002m$, as the base excitation amplitude and the coefficient of restitution. The bifurcation diagram as well as the numerical solutions of period-1 motions of this coupled beam oscillators are obtained via studying the implicit mapping dynamics of the system. As the excitation frequency varies, the bifurcation diagram of impact time, switching displacements and switching velocities of the periodic solutions for the first impact are shown in figures A11(a) A11(b), A12(a) and A12(b) where the solid blue and red dashed lines represent the stable and unstable motions, respectively. Similarly, the bifurcation diagrams for the second impact are presented at figures A13 and A14. Figure A15 shows the average harvested power from P-1 motions

from the impact driven system. According to figure A15 the proposed system generates more power in lower frequencies compared to the higher frequencies.

Based on figures A11 and A12, four different stable P-1 regions are achieved, and figure A5 shows one tip point displacement for both beams and velocities for the driven beam from each region. Figure A8 shows the output power and voltage from the above motions.

Comparing figure A15(a) and figure A15(b), one can see that at low-frequency excitation region, generated power from the impact model is much higher than that from the non-impact model. This shows the higher efficacy of the proposed impact-driven frequency-up-conversion system. In the future, we will look for other periodic motions in the low-frequency domain to find out the maximum generated power from different periodic motions and, discovering effective factors on the power level of various periodic motions.

CHAPTER 5

SUMMARY, CONCLUSION, RECOMMENDATION

In this work, impact induced frequency-up-conversion technology was used to design piezoelectric energy harvesters, which are vibo-impact systems. The piezoelectric energy harvesters mainly contains two beams, a soft driving beam and a piezoelectric driven beam. Three models were designed for this soft driving beam and a piezoelectric driven beam harvester: 1) when two beam impact, both beams bounce back, that is don't allow the tip of two beams to pass through each other during impacts. 2) Designing an impact controlled mechanism, which can move the piezoelectric beam away right after impacts and allow it to finish the free vibration. 3) impact becoming a plucking motion, that is allow the tips of two beams to pass through each other.

In this work, linear constitution law was used to build the model of the driving beam and the piezoelectric beam. For the first two models, lumped parameter models were created for both the driving beam and the piezoelectric beam, while for the third model parametric beam model was used to model both the driving beam and the piezoelectric bimorph. For the second impact controlled model, the impact control mechanism is composed of a pair of rack and pinion and a slider crank mechanism. The slider crank converts the vertical vibrations to small horizontal motions as well as provide a 90-degree phase shift between the vertical vibration and the horizontal motion. This design can synchronize the impact between the piezoelectric bimorph and the soft driving beam, when the proper initial condition is applied.

Discontinuous dynamics theory was applied to all three models to reveal the general trends of frequency response with a varying system parameter and to provide insight into the dynamic characteristics of such systems. Analytical study has been carried out to understand the relations between dynamic behaviors and the power output efficiency of these vibro-impacting energy regeneration systems. We compare the power

output for systems with impact frequency-up-conversion and without impact frequency-up-conversion. All three models showed that with impact frequency-up-conversion the output power is much larger under the same base excitation conditions. We also compared the power efficiency between the impact controlled piezoelectric energy harvester (model II) and none impacted-controlled energy harvester (model I). The results showed that the impact-controlled harvester could significantly improve the energy harvesting efficiency.

For the all three models, the periodic motions and bifurcations were generated with excitation frequency varying. The generated power and voltage from a specic periodic motion have been calculated. Different motions will generate different power. The generated average power was studied for dierent types of periodic motions and also with the non-periodic motion. The bifurcation diagram of the period-1 and period-2 solutions was obtained. The impact displacements, impact velocities, output voltage, and output power of the piezoelectric bimorph were presented as a function of base excitation frequencies.

With the current rapid development of the Internet of Things (IoTs), energy harvesting offers a critical and promising solution for the application of self-powered sensors and terminal modes. The self-powered technology allow these devices operate lone time with a battery charges, this not lonely induces cost savings but also solves environment pollution issues. The sustainability and environmental friendliness of self-powered devices are essential for the development of smart cities, smart homes, smart health, smart agriculture, intelligent transportation, industry, security, marine, and so on.

REFERENCES

[1] X. Zhao, H. Gao, G. Zhang, B. Ayhan, F. Yan, C. Kwan, and J. L. Rose, "Active health monitoring of an aircraft wing with embedded piezoelectric sensor/actuator network: I. defect detection, localization and growth monitoring," *Smart materials and structures*, vol. 16, no. 4, p. 1208, 2007.

[2] T. J. Arsenault, A. Achuthan, P. Marzocca, C. Grappasonni, and G. Coppotelli, "Development of a fbg based distributed strain sensor system for wind turbine structural health monitoring," *Smart Materials and Structures*, vol. 22, no. 7, p. 075027, 2013.

[3] P. Rizzo, M. Cammarata, D. Dutta, H. Sohn, and K. Harries, "An unsupervised learning algorithm for fatigue crack detection in waveguides," *Smart Materials and Structures*, vol. 18, no. 2, p. 025016, 2009.

[4] S. G. Taylor, G. Park, K. M. Farinholt, and M. D. Todd, "Diagnostics for piezoelectric transducers under cyclic loads deployed for structural health monitoring applications," *Smart Materials and Structures*, vol. 22, no. 2, p. 025024, 2013.

[5] G. Owojaiye and Y. Sun, "Focal design issues affecting the deployment of wireless sensor networks for pipeline monitoring," *Ad Hoc Networks*, vol. 11, no. 3, pp. 1237–1253, 2013.

[6] R. Vullers, R. Schaijk, H. Visser, J. Penders, and C. Hoof, "Energy harvesting for autonomous wireless sensor networks," *IEEE Solid-State Circuits Magazine*, vol. 2, no. 2, pp. 29–38, 2010.

[7] V. C. Gungor and G. P. Hancke, "Industrial wireless sensor networks: Challenges, design principles, and technical approaches," *IEEE Transactions on Industrial Electronics*, vol. 56, no. 10, pp. 4258–4265, 2009.

[8] S. M. Glenn, T. D. Dickey, B. Parker, and W. Boicourt, "Long-term real-time coastal ocean observation networks," *OCEANOGRAPHY-WASHINGTON DC-*

OCEANOGRAPHY SOCIETY-, vol. 13, no. 1, pp. 24–34, 2000.

[9] R. Murray and J. Rastegar, "Novel two-stage piezoelectric-based ocean wave energy harvesters for moored or unmoored buoys," in *SPIE Smart Structures and Materials+ Nondestructive Evaluation and Health Monitoring*, pp. 72880E–72880E, International Society for Optics and Photonics, 2009.

[10] J. Sibert, "Electronic tagging and tracking in marine fisheries," in *Electronic Tagging and Tracking in Marine Fisheries*, pp. 1–6, Springer, 2001.

[11] Y. Cha, M. Verotti, H. Walcott, S. D. Peterson, and M. Porfiri, "Energy harvesting from the tail beating of a carangiform swimmer using ionic polymer–metal composites," *Bioinspiration & biomimetics*, vol. 8, no. 3, p. 036003, 2013.

[12] C. B. Williams and R. B. Yates, "Analysis of a micro-electric generator for microsystems," *sensors and actuators A: Physical*, vol. 52, no. 1-3, pp. 8–11, 1996.

[13] P. Glynne-Jones, M. J. Tudor, S. P. Beeby, and N. M. White, "An electromagnetic, vibration-powered generator for intelligent sensor systems," *Sensors and Actuators A: Physical*, vol. 110, no. 1-3, pp. 344–349, 2004.

[14] D. P. Arnold, "Review of microscale magnetic power generation," *IEEE Transactions on Magnetics*, vol. 43, no. 11, pp. 3940–3951, 2007.

[15] P. D. Mitcheson, P. Miao, B. H. Stark, E. M. Yeatman, A. S. Holmes, and T. C. Green, "Mems electrostatic micropower generator for low frequency operation," *Sensors and Actuators A: Physical*, vol. 115, no. 2-3, pp. 523–529, 2004.

[16] S. Roundy, P. K. Wright, and J. M. Rabaey, "Energy scavenging for wireless sensor networks," in *Norwell*, pp. 45–47, Springer, 2003.

[17] S. Roundy, P. K. Wright, and J. Rabaey, "A study of low level vibrations as a power source for wireless sensor nodes," *Computer communications*, vol. 26, no. 11, pp. 1131–1144, 2003.

[18] Y. Jeon, R. Sood, J. Jeong, and S.-G. Kim, "Mems power generator with transverse mode thin film pzt," *Sensors and Actuators A: Physical*, vol. 122, no. 1, pp. 16–22,

2005.

[19] S. P. Beeby, J. Tudor, and N. M. White, "Energy harvesting vibration sources for microsystems applications," *Measurement science and technology*, vol. 17, no. 12, p. R175, 2006.

[20] K. Cook-Chennault, N. Thambi, and A. M. Sastry, "Powering mems portable devices—a review of non-regenerative and regenerative power supply systems with special emphasis on piezoelectric energy harvesting systems," *Smart Materials and Structures*, vol. 17, no. 4, p. 043001, 2008.

[21] A. Erturk and D. J. Inman, "On mechanical modeling of cantilevered piezoelectric vibration energy harvesters," *Journal of Intelligent Material Systems and Structures*, 2008.

[22] G. Park, T. Rosing, M. D. Todd, C. R. Farrar, and W. Hodgkiss, "Energy harvesting for structural health monitoring sensor networks," *Journal of Infrastructure Systems*, vol. 14, no. 1, pp. 64–79, 2008.

[23] N. Elvin, A. Elvin, and D.-H. Choi, "A self-powered damage detection sensor," *The Journal of Strain Analysis for Engineering Design*, vol. 38, no. 2, pp. 115–124, 2003.

[24] T. Monnier, P. Guy, M. Lallart, L. Petit, D. Guyomar, and C. Richard, "Optimization of signal pre-processing for the integration of cost-effective local intelligence in wireless self-powered structural health monitoring," in *Advances in Science and Technology*, vol. 56, pp. 459–468, Trans Tech Publ, 2008.

[25] N. E. Dutoit, B. L. Wardle, and S.-G. Kim, "Design considerations for mems-scale piezoelectric mechanical vibration energy harvesters," *Integrated Ferroelectrics*, vol. 71, no. 1, pp. 121–160, 2005.

[26] N. Stephen, "On energy harvesting from ambient vibration," *Journal of sound and vibration*, vol. 293, no. 1, pp. 409–425, 2006.

[27] M. Marzencki, Y. Ammar, and S. Basrour, "Integrated power harvesting system including a mems generator and a power management circuit," *Sensors and Actuators*

A: Physical, vol. 145, pp. 363–370, 2008.

[28] I. Kuehne, D. Marinkovic, G. Eckstein, and H. Seidel, "A new approach for mems power generation based on a piezoelectric diaphragm," *Sensors and Actuators A: Physical*, vol. 142, no. 1, pp. 292–297, 2008.

[29] F. Wang, Z. Wang, M. Soroush, and A. Abedini, "Energy harvesting efficiency optimization via varying the radius of curvature of a piezoelectric thunder," *Smart Materials and Structures*, vol. 25, no. 9, p. 095044, 2016.

[30] F. Wang, W. Wu, A. Lozowski, V. Alizadehyazdi, and A. Abedini, "Energy harvesting with a piezoelectric thunder," in *ASME 2015 International Mechanical Engineering Congress and Exposition*, pp. V04BT04A043–V04BT04A043, American Society of Mechanical Engineers, 2015.

[31] c. Eichhorn, F. Goldschmidtboeing, and P. Woias, "Bidirectional frequency tuning of a piezoelectric energy converter based on a cantilever beam," *Journal of Micromechanics and Microengineering*, vol. 19, no. 9, p. 094006, 2009.

[32] M. Lallart, S. R. Anton, and D. J. Inman, "Frequency self-tuning scheme for broadband vibration energy harvesting," *Journal of Intelligent Material Systems and Structures*, vol. 21, no. 9, pp. 897–906, 2010.

[33] M. Umeda, K. Nakamura, and S. Ueha, "Energy storage characteristics of a piezogenerator using impact induced vibration," *Japanese journal of applied physics*, vol. 36, no. 5S, p. 3146, 1997.

[34] M. Renaud, P. Fiorini, R. van Schaijk, and C. Van Hoof, "Harvesting energy from the motion of human limbs: the design and analysis of an impact-based piezoelectric generator," *Smart Materials and Structures*, vol. 18, no. 3, p. 035001, 2009.

[35] G. Manla, N. M. White, and J. Tudor, "Harvesting energy from vehicle wheels," in *Solid-State Sensors, Actuators and Microsystems Conference, 2009. TRANSDUCERS 2009. International*, pp. 1389–1392, IEEE, 2009.

[36] Q. Tang, Y. Yang, and X. Li, "Bi-stable frequency up-conversion piezoelectric en-

ergy harvester driven by non-contact magnetic repulsion," *Smart Materials and Structures*, vol. 20, no. 12, p. 125011, 2011.

[37] T. Xue and S. Roundy, "Analysis of magnetic plucking configurations for frequency up-converting harvesters," in *Journal of Physics: Conference Series*, vol. 660, p. 012098, IOP Publishing, 2015.

[38] P. Pillatsch, E. M. Yeatman, and A. S. Holmes, "A piezoelectric frequency up-converting energy harvester with rotating proof mass for human body applications," *Sensors and Actuators A: Physical*, vol. 206, pp. 178–185, 2014.

[39] L. Gu and C. Livermore, "Impact-driven, frequency up-converting coupled vibration energy harvesting device for low frequency operation," *Smart Materials and Structures*, vol. 20, no. 4, p. 045004, 2011.

[40] P. S. Gandhi and V. Vyas, "On the dynamics of tapered vibro-impacting cantilever with tip mass," *Journal of Mechanical Science and Technology*, vol. 31, no. 1, pp. 63–73, 2017.

[41] S. Stoykov, G. Litak, and E. Manoach, "Vibration energy harvesting by a timoshenko beam model and piezoelectric transducer," *The European Physical Journal Special Topics*, vol. 224, no. 14-15, pp. 2755–2770, 2015.

[42] A. Abedini, S. Onsorynezhad, and F. Wang, "Study of an impact driven frequency up-conversion piezoelectric harvester," in *ASME 2017 Dynamic Systems and Control Conference*, pp. V003T41A005–V003T41A005, American Society of Mechanical Engineers, 2017.

[43] M. Pozzi, M. S. Aung, M. Zhu, R. K. Jones, and J. Y. Goulermas, "The pizzicato knee-joint energy harvester: characterization with biomechanical data and the effect of backpack load," *Smart Materials and Structures*, vol. 21, no. 7, p. 075023, 2012.

[44] P. L. Green, K. Worden, K. Atallah, and N. D. Sims, "The benefits of duffing-type nonlinearities and electrical optimisation of a mono-stable energy harvester under white gaussian excitations," *Journal of Sound and Vibration*, vol. 331, no. 20,

pp. 4504–4517, 2012.

[45] R. L. Harne and K.-W. Wang, "A review of the recent research on vibration energy harvesting via bistable systems," *Smart materials and structures*, vol. 22, no. 2, p. 023001, 2013.

[46] R. M. May, "Simple mathematical models with very complicated dynamics," *Nature*, vol. 261, 1976.

[47] M. Henon, "A two-dimensional mapping with a strange attractor," *Communications in Mathematical Physics*, vol. 50, pp. 69–77, 1976.

[48] F. R. Marotto, "Chaotic behavior in the hénon mapping," *Communications in Mathematical Physics*, vol. 68, no. 2, pp. 187–194, 1979.

[49] J. H. Curry, "On the hénon transformation," *Communications in Mathematical Physics*, vol. 68, no. 2, pp. 129–140, 1979.

[50] P. Cvitanović, G. H. Gunaratne, and I. Procaccia, "Topological and metric properties of hénon-type strange attractors," *Physical Review A*, vol. 38, no. 3, p. 1503, 1988.

[51] A. C. Luo and R. P. Han, "Period doubling and multifractals in 1-d interative maps," *Chaos, Solitons & Fractals*, vol. 2, no. 3, pp. 335–348, 1992.

[52] J. A. Gallas, "Structure of the parameter space of the hénon map," *Physical Review Letters*, vol. 70, no. 18, p. 2714, 1993.

[53] Z. T. Zhusubaliyev, V. N. Rudakov, E. A. Soukhoterin, and E. Mosekilde, "Bifurcation analysis of the henon map," *Discrete Dynamics in Nature and Society*, vol. 5, no. 3, pp. 203–221, 2000.

[54] S. W. Shaw and P. J. Holmes, "A periodically forced piecewise linear oscillator," *Journal of sound and vibration*, vol. 90, no. 1, pp. 129–155, 1983.

[55] B. Feeny and F. C. Moon, "Chaos in a forced dry-friction oscillator: Experiments and numerical modelling," *Journal of Sound and Vibration*, vol. 170, no. 3, pp. 303–323, 1994.

[56] A. C. Luo and Y. Guo, "Motion switching and chaos of a particle in a generalized fermi-acceleration oscillator," *Mathematical problems in engineering*, vol. 2009, 2009.

[57] A. C. Luo and Y. Guo, "Switching mechanism and complex motions in an extended fermi-acceleration oscillator," *Journal of Computational and Nonlinear Dynamics*, vol. 5, no. 4, p. 041007, 2010.

[58] Y. Guo and A. C. Luo, "Parametric analysis of bifurcation and chaos in a periodically driven horizontal impact pair," *International Journal of Bifurcation and Chaos*, vol. 22, no. 11, p. 1250268, 2012.

[59] D. O'Connor and A. C. Luo, "On discontinuous dynamics of a freight train suspension system," *International Journal of Bifurcation and Chaos*, vol. 24, no. 12, p. 1450163, 2014.

[60] A. Meitzler, H. Tiersten, A. Warner, D. Berlincourt, G. Couqin, and F. Welsh III, "Ieee standard on piezoelectricity," 1988.

[61] J. W. S. B. Rayleigh, *The theory of sound*, vol. 2. Macmillan, 1896.

APPENDICES

APPENDIX A

LUMPED PARAMETERS

Sine and cosine coefficients

The coefficients of particular solution for the driving beam in Equ.4.31 is presented as:

$$\begin{Bmatrix} A \\ B \end{Bmatrix} = \begin{pmatrix} \omega_{n_d}^2 - \Omega^2 & -2\zeta_d\omega_{n_d}\Omega \\ 2\zeta_d\omega_{n_d}\Omega & \omega_{n_d}^2 - \Omega^2 \end{pmatrix}^{-1} \begin{Bmatrix} \omega_n^2 Q \\ 2\zeta_d Q\omega_{n_d}\Omega \end{Bmatrix}. \tag{5.1}$$

Using the above equation, the sine and cosine coefficients of the Equ.4.31 can be exp[ressed as:

$$C_{c_d} = z_d(t_{k-1}) - A\sin\Omega t_{k-1} - B\cos\Omega t_{k-1} \tag{5.2a}$$

$$C_{s_d} = \frac{\dot{z}_d(t_{k-1}) + \zeta_d\omega_{n_d} z_d(t_{k-1}) + (B\Omega - A\zeta\omega_{n_d})\sin\Omega t_{k-1} - (A\Omega + B\zeta\omega_{n_d})\cos\Omega t_{k-1}}{\omega_{d_d}}. \tag{5.2b}$$

Similarly, the equations below hold for the driven beam:

$$C_{c_p} = z_p(t_{k-1}) \tag{5.3a}$$

$$C_{s_p} = \frac{\dot{z}_p(t_{k-1}) + \zeta_p\omega_{n_p} z_p(t_{k-1})}{\omega_{d_p}}. \tag{5.3b}$$

APPENDIX B

EULER-BERNOULLI

$$\dot{v}(t) + \frac{1}{C_p R} v(t) = \frac{\theta_i}{C_p} \dot{\eta}_i(t) \tag{5.4}$$

$$V(S) = \frac{1}{S + \frac{1}{C_p R}} \left(\frac{\theta_i}{C_p} \dot{\eta}_i(S) - v(0) \right) \tag{5.5}$$

$$\begin{aligned} v(t) &= \frac{\theta_i}{C_p} \int_0^t \dot{\eta}_i(\tau) e^{\frac{-1}{C_p R}(t-\tau)} d\tau - v(0) e^{\frac{t}{C_p R}} \\ &= \frac{\theta_i}{C_p} e^{\frac{t}{C_p R}} \int_0^t \dot{\eta}_i(\tau) e^{\frac{-1}{C_p R}\tau} d\tau - v(0) e^{\frac{-1}{C_p R}} \end{aligned} \tag{5.6}$$

$$\begin{aligned} &\int_0^t \dot{\eta}_i(\tau) e^{\frac{1}{C_p R}\tau} d\tau = C_p R \int_0^t \dot{\eta}_i(\tau) d[e^{\frac{1}{C_p R}\tau}] \\ &= C_p R \left[\dot{\eta}_i(\tau) e^{\frac{1}{C_p R}\tau} \Big|_0^t - \int_0^t \ddot{\eta}_i(\tau) e^{\frac{1}{C_p R}\tau} d\tau \right] \\ &= C_p R \left[\dot{\eta}_i(t) e^{\frac{1}{C_p R}t} - \dot{\eta}_i(0) + \int_0^t (2\xi\omega_i \dot{\eta}_i(\tau) + \omega_i^2 \dot{\eta}_i(\tau) - I_i \Omega^2 A_0 \sin(\Omega\tau)) e^{\frac{1}{C_p R}\tau} d\tau \right] \end{aligned} \tag{5.7}$$

$$\begin{aligned} \int_0^t \dot{\eta}_i(\tau) e^{\frac{1}{C_p R}\tau} d\tau &= \int_0^t e^{\frac{1}{C_p R}\tau} d\eta_i(\tau) = \eta_i(\tau) e^{\frac{1}{C_p R}\tau} \Big|_0^t - \frac{1}{C_p R} \int_0^t \eta_i(\tau) e^{\frac{1}{C_p R}\tau} d\tau \\ \int_0^t \eta_i(\tau) e^{\frac{1}{C_p R}\tau} d\tau &= C_p R \eta_i(\tau) e^{\frac{1}{C_p R}t} - C_p R \eta_i(0) - C_p R \int_0^t \dot{\eta}_i(\tau) e^{\frac{1}{C_p R}\tau} d\tau \end{aligned} \tag{5.8}$$

Substitute (8) into (7)

$$\begin{aligned} \int_0^t \dot{\eta}_i(\tau) e^{\frac{1}{C_p R}\tau} d\tau &= C_p R \dot{\eta}_i(t) e^{\frac{1}{C_p R}t} - C_p R \dot{\eta}_i(0) + 2 C_p R \int_0^t \dot{\eta}_i(\tau) e^{\frac{1}{C_p R}\tau} d\tau \\ &+ C_p R \omega_i^2 \int_0^t \eta_i(\tau) e^{\frac{1}{C_p R}\tau} d\tau - C_p R I_i \Omega^2 A_0 \int_0^t \sin(\Omega\tau) e^{\frac{1}{C_p R}\tau} d\tau \end{aligned} \tag{5.9}$$

$$\int_0^t \eta_i(\tau) e^{\frac{1}{C_p R}\tau} d\tau = C_p R \eta_i(t) e^{\frac{1}{C_p R}t} - C_p R \eta_i(0) - C_p R \int_0^t \dot{\eta}_i(\tau) e^{\frac{1}{C_p R}\tau} d\tau \tag{5.10}$$

$$\begin{aligned} \int_0^t \dot{\eta}_i(\tau) e^{\frac{1}{C_p R}\tau} d\tau &= C_p R \dot{\eta}_i(t) e^{\frac{1}{C_p R}t} - C_p R \dot{\eta}_i(0) + 2 C_p R \xi \omega_i \int_0^t \dot{\eta}_i(\tau) e^{\frac{1}{C_p R}\tau} d\tau \\ &+ C_p R \omega_i^2 \left[C_p R \eta_i(t) e^{\frac{1}{C_p R}t} - C_p R \eta_i(0) - C_p R \int_0^t \eta_i(\tau) e^{\frac{1}{C_p R}\tau} d\tau \right] \end{aligned} \tag{5.11}$$

$$\int_0^t \dot{\eta}_i(\tau)e^{\frac{1}{C_pR}\tau}d\tau = \frac{C_pR}{1-2C_pR\xi\omega_i+(C_pR\xi\omega_i)^2}\Bigg[\dot{\eta}_i(t)e^{\frac{1}{C_pR}t} - C_pR\omega_i^2\eta_i(t)e^{\frac{1}{C_pR}t} \\ - \dot{\eta}_i(0) - C_pR\omega_i^2\eta_i(0) - I_i\Omega^2A_0\int_0^t \sin(\Omega\tau)e^{\frac{1}{C_pR}\tau}d\tau\Bigg] \tag{5.12}$$

$$\begin{aligned} v(t) &= \frac{\theta_i}{C_p}e^{\frac{-1}{C_pR}t}\int_0^t \dot{\eta}_i(\tau)e^{\frac{1}{C_pR}\tau}d\tau - v(0)e^{\frac{-1}{C_pR}t} \\ &\frac{R\theta_i}{1-2C_pR\xi\omega_i+(C_pR\xi\omega_i)^2}\Bigg[\dot{\eta}_i(t) + C_pR\omega_i^2\eta_i(t)e^{\frac{1}{C_pR}t} \\ &- \dot{\eta}_i(0)e^{\frac{1}{C_pR}t} - C_pR\omega_i^2\eta_i(0)e^{\frac{-1}{C_pR}t} - I_i\Omega^2A_0\int_0^t \sin(\Omega\tau)e^{\frac{1}{C_pR}\tau}d\tau\Bigg] \\ &- v(0)e^{\frac{-1}{C_pR}t} \end{aligned} \tag{5.13}$$

VITA

Graduate School
Southern Illinois University

Amin Abedini

aminabedini@gmail.com

Sharif University of Technology
Bachelor of Science, Aerospace Engineering, July 2011
Sharif University of Technology
Master of Science, Mechanical Engineering, January 2014

Dissertation Paper Title:
PIEZOELECTRIC ENERGY HARVESTING VIA FREQUENCY UP-CONVERSION TECHNOLOGY

Major Professor: Dr. F. Wang

Publications:

1- A. Abedini, S. Onsorynezhad, F. Wang, Periodic Solutions of an Impact-Driven Frequency Up-Conversion Piezoelectric Harvester, Accepted in: **International Journal of Bifurcation and Chaos**, 2019.

2- A. Abedini, F. Wang, Energy Harvesting of a Frequency Up-Conversion Piezoelectric Harvester with Controlled Impact, in: **The European Physical Journal Special Topics**, Acceptance recommended by Topic Editor, 2019.

3- S. Onsorynezhad, **A. Abedini**, F. Wang, Analytical study of a piezoelectric frequency up-conversion harvester under sawtooth wave excitation, 2018, p. V002T18A004. doi:10.1115/DSCC2018-9173. 10.1115/DSCC2018-9173.

4- A. Abedini, S. Onsorynezhad, F. Wang, Study of an impact driven frequency up-conversion piezoelectric harvester, in: ASME 2017 Dynamic Systems and Control Conference, American Society of Mechanical Engineers, 2017, pp. V003T41A005–V003T41A005.

5- F. Wang, Z. Wang, M. Soroush, **A. Abedini**, Energy harvesting efficiency optimization via varying the radius of curvature of a piezoelectric thunder, **Smart Materials and Structures** 25 (9) (2016) 095044.

6- Wang, Fengxia & wu, Wei & Mahmoudiandehkordi, Soroush & **Abedini, Amin**. (2016). Energy Harvesting with a Piezoelectric Thunder. **Journal of Applied Nonlinear Dynamics**. 5. 423-439. 10.5890/JAND.2016.12.004.

7- F. Wang, W. Wu, A. Lozowski, V. Alizadehyazdi, **A. Abedini**, Energy harvesting with a piezoelectric thunder, in: ASME 2015 International Mechanical Engineering Congress and Exposition, American Society of Mechanical Engineers, 2015, pp. V04BT04A043–V04BT04A043.

8- F. Wang, W. Wu, V. Alizadehyazdi, **A. Abedini**, Energy Harvesting Efficiency Optimization via Varying the Radius of Curvature of a Piezoelectric THUNDER. ASME. Dynamic Systems and Control Conference, American Society of Mechanical Engineers, 2015, V002T22A004. doi:10.1115/DSCC2015-9890.